Ultrafast Laser Driven Micro-Lens to Focus and Energy Select MeV Protons

Inaugural-Dissertation

zur

Erlangung des Doktorgrades der

Mathematisch-Naturwissenschaftlichen Fakultät

der Heinrich-Heine-Universität Düsseldorf

vorgelegt von

Toma Toncian

aus Cluj-Napoca/Klausenburg (RO)

Mai 2008

Aus dem Institut für Laser- und Plasmaphysik
der Heinrich-Heine Universität Düsseldorf

Gedruckt mit der Genehmigung der

Mathematisch-Naturwissenschaftlichen Fakultät der

Heinrich-Heine Universität Düsseldorf

Referent: Prof. Dr. O. Willi

Koreferent: Prof. Dr. K.-H. Spatschek

Koreferent: Prof. Dr. P. Mulser

Tag der mündlichen Prüfung: 03.11.2008

Abstract

A technique for simultaneous focusing and energy selection of high-current, MeV proton beams using radial, transient electric fields (10^7-10^{10} V/m) triggered on the inner wall of a hollow micro-cylinder by an intense, sub-picosecond laser-pulse is presented. Due to the transient nature of the radial focusing field, the proposed method allows selection of a desired range out of the spectrum of the poly-energetic proton beam. This technique addresses current drawbacks of laser-accelerated proton beams, i.e. their broad spectrum and divergence at the source. This thesis presents both experimental and computational studies that led to the understanding of the physical processes driving the micro-lens. After an one side irradiation of a hollow metallic cylinder a radial electric field develops inside the cylinder. Hot electrons generated by the interaction between laser pulse and cylinder wall spread inside the cylinder generating a plasma at the wall. This plasma expands into vacuum and sustains an electric field that acts as a collecting lens on a proton beam propagating axially through the cylinder. Both focusing and the reduction of the intrinsic beam divergence from 20 deg to .3 deg for a narrow spectral range was demonstrated. By sub-aperturing the beam a narrow spectral range ($\delta\mathcal{E}/\mathcal{E} < 3\%$) was selected from the poly-energetic beam. The micro-lens properties are tunable allowing for optimization towards applications. Optical probing techniques and proton imaging were employed to study the spacial and temporal evolution of the field and revealed a complex physical scenario of the rise and decay of the radial electric field. Each aspect studied experimentally is interpreted using 2D PIC and ray tracing simulations. A very good agreement between the experimental and computational data is found. The PIC simulations are used to upscale the demonstrated micro-lens capabilities to the focusing of a 270 MeV proton beam, an energy relevant for medical applications such as the hadron therapy of deep-seated tumours.

Zusammenfassung

Eine Technik zur gleichzeitigen Fokussierung und Energieselektion eines hoch strömigen MeV Protonenstrahls durch kurzlebige radiale elektrische Felder (10^7-10^{10} V/m), die an der Innenfläche eines hohlen Mikrozylinders durch einen intensiven subpikosekunden Laserstrahl erzeugt werden, wird in dieser Arbeit vorgestellt. Auf Grund der Kurzlebigkeit der Felder kann die Methode zur Selektion eines beliebigen Ausschnitts aus dem Energiesspektrum eines polyenergetischen Protonenstrahls eingesetzt werden. Diese Technik wirkt den aktuellen Nachteilen der lasererzeugten Protonenstahlen, wie ein breites Spektrum und der Divergenz der Quelle, entgegen. Diese Arbeit stellt sowohl experimentelle als auch rechnerunterstützte Untersuchungen, welche zum Verständnis der physikalischen Prozesse der Mikrolinse führen, vor. Nach einer einseitigen Bestrahlung eines metallischen Hohlzylinders wird im Innern ein radiales elektrisches Feld erzeugt. Die bei der Wechselwirkung zwischen Laserpuls und Zylinder erzeugten heissen Elektronen verteilen sich an der Zylinderwand und erzeugen dabei ein Plasma. Das Plasma expandiert ins Vakuum und hält ein elektrisches Feld aufrecht, welches auf einen durch den Zylinder axial propagierenden Protonenstahl wie eine Sammellinse wirkt. Sowohl die Fokussierung als auch die Reduzierung der intrinsischen Strahldivergenz von 20 Grad auf 0.3 Grad eines schmalen spektralen Bereiches werden gezeigt. Mit Hilfe einer Blende konnte aus dem polyenergetischen Strahl ein schmaler spektraler Bereich ($\delta\mathcal{E}/\mathcal{E} < 3\%$) selektiert werden. Die Eigenschaften der Mikrolinse sind variabel einstellbar und ermöglichen Optimierungen für mögliche Anwendungen. Mit dem Einsatz optischer Diagnostiken als auch von Proton Imaging konnte die räumliche und zeitliche Entwicklung des Feldes untersucht werden. Dabei ergab sich ein komplexes physikalisches Szenario des Aufbaus und des Zerfalls des radialen Feldes. Jeder experimentell untersuchte Aspekt wurde mit Hilfe von 2D PIC und ray tracing Simulationen interpretiert. Eine sehr gute Übereinstimmung von Experiment und Simulation wurde gefunden. Die PIC Simulationen wurden verwendet um die Praxistauglichkeit der Mikrolinse beim Einsatz eines 270 MeV Protonenstahls zu zeigen. Diese Protonenenergie ist für medizinische Anwendungen, wie die Schwerionentherapie von Tumoren, von hoher Bedeutung.

Contents

Chapter 1

Motivation and Introduction

The recent development of ultra-intense laser pulses [1] has opened up opportunities for applications in many areas including particle acceleration ([2], [3], [4], [5]), inertial fusion energy [6], generation of intense x-ray pulses [7], laser-driven nuclear physics [8] and laboratory astrophysics [9]. In particular, the acceleration of MeV ions from the interaction of high-intensity laser-pulses with thin solids has major applicative prospects due to the high beam quality of these ion bursts [10], [11]. Such proton beams are already applied to produce high energy density matter [12] or to radiograph transient processes [13], and offer high prospects for tumour therapy [14], isotope generation for positron emission tomography [15], fast ignition of fusion cores [16] and brightness increase of conventional accelerators. However, as these proton beams are poly-energetic and divergent at source, reduction and control of their divergence and energy spread are essential requirements for most of these applications.

Focusing of energetic proton beams is usually achieved using electrostatic or magnetic lenses [17] that have several drawbacks, namely: slow switching times, large sizes, asymmetry in the transverse plane for the focused beam, aberrations, inability to focus large currents and large heat dissipation. It has been proposed that particle selection and beam collimation of laser produced protons applicable for tumour therapy could be achieved by means of super-conducting magnetic systems [18]. Relativistic laser-plasma devices appear in principle more suitable to achieve the required angular and spectral control of laser-accelerated ion beams since they can withstand large ion beam currents, can be switched over ps time scales and can support large deflecting fields on micro-scales. Advances in ion beam tailoring have been achieved so far mainly by employing target engineering techniques. Geometrical focusing of laser-driven protons

has been attained by using curved targets [12]. Demonstration of this technique has been limited so far to focal distances of a few mm and to the low energy component of the proton spectrum. Very recently, quasi-monochromatic acceleration from laser irradiated micro-structured targets has been reported ([19] ,[20]). In these approaches, the focusing or energy selection effect is achieved by directly acting on the source. As a consequence, these techniques rely on relatively complex target fabrication or preparation procedures.

In this work an alternative approach which provides tuneable, simultaneous focusing and energy selection of MeV proton beams is described. This approach decouples the beam tailoring stage from the acceleration stage allowing for their independent optimization. This leads to a system with higher flexibility than the methods above, relaxing significantly the target fabrication constraints. The method employs a compact laser driven micro-lens arrangement which will be described in more details in chapter 5 of this thesis.

The author was involved in several experiments at the LULI Laboratory in France and the Rutherford Appleton Laboratory in the UK conducted in collaboration with Dr. Marco Borghesi and Dr. Julien Fuchs and supervised by Prof. O. Willi. During the experimental studies of the micro-lens the author had the full responsibility of all aspects concerning planning, preparation and execution of the experiments. The author has given substantial contributions to performing the experiments involving: setting-up the laser beam line; timing and synchronization of multiple beam; setting-up optical and proton diagnostics; target preparation and alignment as described in chapter 4. A special cutting machine for producing the cylinders was constructed. After the experiment the author reduced the collected data which involved image processing of the digitized films; detector calibration; mapping proton deflection and energy spectra extraction. To assist the analysis and interpretation of the data, the author used the PSC PIC kindly provided by H. Ruhl and specially extended the code to be used for simulations of the micro-lens. The output of the simulations was analyzed in detail, compared with the experiments and used in a ray tracing program to postprocess the proton propagation through the micro-lens.

A shot summary of the each chapter dividing this work is given now:

- Chapter 2 provides a brief description of the interaction of high intensity laser pulses with high density matter. First the light interaction with single atoms and then with a plasma is presented. The ionization, relativistic effects and heating

mechanisms are discussed. The next section of this chapter is focused on the acceleration mechanisms of electrons, protons and ions to multi-MeV energies. Conventional and state of the art beam manipulation techniques are presented. Theoretical and computational aids (SRIM) for solving the stopping of ions in matter are shown. The last section will introduce the Plasma Simulation Code (PSC). A very brief description of the concepts leading to the Vlasov-Boltzmann equation, one of the equation solved by PSC is followed by more details about the numerical scheme used by the code.

- Chapter 3 gives a detailed description of the diagnostics that were employed during this work. An absolute calibration of various types of RadioChromic Films (RCF) and Fuji Image Plates (IP) has been conducted using protons at the MPIK Tandem Ion Accelerator Heidelberg.

- Chapter 4 describes the experimental setup used at the 100 TW laser facility at LULI laboratory in France and Target Area West at Vulcan laser at the Rutherford Appleton laboratory in UK. The specific details of the used laser systems and experimental setups are presented.

- Chapter 5 shows the experimental results of this work and gives the theoretical understanding of the physical processes that lead to the creation of radial electric fields from the cylinder walls. First the focusing and divergence manipulation of a laser accelerated proton beam with the aid of the laser triggered micro-lens is discussed. 2D Particle in Cell simulations of the plasma evolution from the cylinder are shown and discussed. A qualitative comparison with the experimental results is made. Symmetry requirements are derived. Then the energy selection capability of the laser triggered micro-lens is addressed. Ways of tuning the focusing properties of the lens are presented. At the end of this chapter various optical and proton probing experimental results concerning the electron transport in the cylinder are shown. A novel proton imaging setup capable of making continuous time resolved measurements is introduced applied for the study of instabilities growing on a 100 ps time scale from the cylinder wall. The chapter closes by presenting a scaling of the lens operation towards higher proton beam energies with the help of PSC simulations.

- Chapter 6 summarizes the experimental and computational results of this thesis and gives an outlook for further developments of the laser triggered micro-lens towards applications.

Chapter 2

Laser-Plasma-Interaction

2.1   Introduction

When a high intensity laser light interacts with matter both matter and light react. Atoms will be ionized in shortest time, a plasma will be created and heated and this will change the properties of the irradiated light. The light energy is transformed in disordered particle motion associated to a temperature.

Certain intensity thresholds of the light wave intensity can be defined. The first intensity threshold is related to the motion of an electron on its first Bohr radius. At this intensity the electric field of the laser overcomes the Coulomb attraction force, the electron is freed and the atom is ionized. The second intensity threshold is the intensity at which the quivering motion of an electron in the light field becomes relativistic. The needed intensity is found to be:

$$I_{\text{rel e}} = 1.37 \times 10^{18}\,[\text{W/cm}^2]/\lambda^2[\mu\text{m}^2]. \tag{2.1}$$

At higher intensities ($4.5 \times 10^{24}\,\text{W/cm}^2$) the relativistic threshold for the quivering motion of the proton in the laser field is reached. For even higher ($\simeq 5 \times 10^{29}\,\text{W/cm}^2$) the breakdown of vacuum and creation of election positron pairs are expected [21]. Such high intensities are still to be experimentally demonstrated, but high power lasers are in consideration and it is very probable that they will be commissioned as non military facilities in the not very distant future ([22] and [23]). The laser intensities employed during this work varied between 10^{18} to $5 \times 10^{19}\,\text{W/cm}^2$, intensities that are easily provided by multi TW CPA glass laser systems.

The next section will provide the reader with a brief review of the ionization processes. Section 2.3 will describe the motion of a single electron in a laser field. Next the propagation and absorption of the laser by collective plasma effects will be addressed. The most relevant electron acceleration processes will be presented followed by a more detailed description of laser proton acceleration. This chapter is closed by showing the ion stopping mechanisms in solid targets and the computational aids for solving this problem.

2.2 Ionization

2.2.1 Optical Ionization

The creation of a plasma is associated with the production of free electrons. Ionization of neutral atoms can be done either interacting directly with the laser light or with particles. The most important optical ionization processes are introduced now [24].

- **MPI-Multi-Photon-Ionization.** At low intensities $I \ll 10^{12}\,\mathrm{W/cm^2}$ dominates a process, where an electron absorbs n-photons, so that $\hbar n \omega_L = E_{Ion}$, and is ionized from a bound state. The properties of MPI can be predicted with nth order perturbation theory. The rate of n-photon ionization is given by:

$$\Gamma_n = \sigma_n I^n, \tag{2.2}$$

  where σ_n is a generalized cross section and I the laser intensity.

- **ATI-Above-Threshold Ionization.** For higher intensity $< 10^{14}\,W/cm^2$ we leave the perturbation regime of the MPI. Electrons absorb more photons than needed for ionization. One finds a generalization of eq. 2.2: $\Gamma_{n+s} \propto I^{n+s}$, with s the number of excess electrons. The equation describing the energy of the photo-electron is:

$$E_f = (n+s)\hbar\omega - E_{ion}. \tag{2.3}$$

- **OFI-Optical Field Ionization.** At an intensity close to $10^{14} - 10^{15}\,\mathrm{W/cm^2}$ the laser electric field approaches the value of the atomic bounding fields. We pass to the regime of Optical Field Ionization. During this process the bounding field between electron and nuclei is suppressed. The **ADK-**model of tunnel ionization [25] after Ammosov, Delone and Krainov describes the OFI when the Coulomb

potential is just partially suppressed. When the Coulomb potential is completely suppressed we talk of **BSI** (Barrier Suppression Ionization).

- **Keldysh-Parameter.** The ionization dynamic can be described by the Keldysh-parameter:

$$\gamma^2 = \frac{2\omega_L^2 E_{ion}}{I_L}. \tag{2.4}$$

For $\gamma < 1$ dominates tunnel ionization and for $\gamma > 1$ the ionization is dominated by multi-photon processes.

2.2.2   Electron Impact Ionization

Even after the laser pulse is gone the ionization of neutral atoms or not fully ionized ions continues. Electron impact ionization is the process of ionization of a positive ion with a charge greater than 1 by an electron impact. A collision of this type may be described by the scheme:

$$A_{z,q} + e^- \rightarrow A_{z+1,q'} + 2e^-,$$
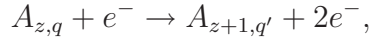
where the subscript $z = 2, 3, 4, ...$ denotes an ionization stage of the target-ion A_z, the subscript q denotes a state (energy level) to be ionized and the subscript q' denotes a state of product ion A_{z+1} just after removal of the electron.

The shortage in the experimental cross section data motivated a search for empirical formulae capable of reasonably accurate prediction for any transition. The most successful expression was proposed 30 years ago by Lotz [26] for total direct ionization cross sections $\sigma_{zq}^{ioniz}(\varepsilon)$, i.e. for ionization into all possible final states

$$\sigma_{zq}^{ioniz}(\varepsilon) = 4.5 \times 10^{-14} \sum_k \zeta_{zqk} \frac{\ln(\varepsilon/E_{zqk})}{\ln(\varepsilon) E_{zqk}} \text{ cm}^2.$$

Here ε is the incident electron energy, the subscript k runs over all $nl-$subshells of $A_{z,q}$, E_{zqk} is the minimal energy required for ionization from state q into state k (which may be an excited state) and ζ_{zqk} is the number of equivalent electrons in the nl-subshell which has to loose one electron for the transition.

Using the GENIE database (`http://www-amdis.iaea.org/GENIE/`) an empiric fit function can be found for the ionization cross sections using fit functions as recommended by Bell et al. in [27]. A specific set of fit parameters for each element and each charge stage can be found at GENIE.

2.3 Single Electron Motion and Ponderomotive Potential

Charged particles feel a force and begin to move as soon as laser light interacts with ionized matter. The laser fields can be expressed in the case of SVEA (slow varying envelope approximation) for vacuum and linear polarization as [28]:

$$
\begin{aligned}
\vec{E}(\vec{r},t) &= E_0(\vec{r},t)\vec{e_x}e^{i(\omega t - kz)} \\
\vec{B}(\vec{r},t) &= B_0(\vec{r},t)\vec{e_y}e^{i(\omega t - kz)} \qquad \text{with} \qquad B_0 = \frac{E_0}{c},
\end{aligned}
\tag{2.5}
$$

and $\vec{e_z}$ the propagation direction, $\vec{e_y}$ and $\vec{e_x}$ perpendicular to $\vec{e_z}$ and c the vacuum light speed. These fields are very difficult to measure directly, therefore the intensity is used for measuring the strength of a light wave:

$$
I(\vec{r},t) = \left\langle \left| \vec{E} \times \frac{\vec{B}}{\mu_0} \right| \right\rangle = \frac{\varepsilon_0 c}{2} \left| E_0(\vec{r},t) \right|^2 .
\tag{2.6}
$$

The usual intensity unit is [W/cm^2], ε_0 is the vacuum permittivity and μ_0 the vacuum permeability. The force that acts on a charge Ze, moving with a velocity $\vec{\beta} = \vec{v}/c$ is the Lorentz force:

$$
\frac{\mathrm{d}\vec{p}}{\mathrm{d}t} = \frac{\mathrm{d}(\gamma m c \vec{\beta})}{\mathrm{d}t} = Ze(\vec{E} + c\vec{\beta} \times \vec{B}),
\tag{2.7}
$$

with m particle mass and $\gamma = 1/\sqrt{1 + v^2/c^2}$.

For non-relativistic particles viz. $\beta \ll 1$, the second term in eq. 2.7 can be neglected. The resulting motion is a transverse harmonic oscillation in the electric field with a maximum amplitude and a speed in the order of:

$$
s_0 \simeq \frac{|Ze|}{m}\frac{E_0}{\omega^2} \qquad \text{and} \qquad |\vec{v}| \simeq \frac{|Ze|}{m}\frac{E_0}{\omega}.
\tag{2.8}
$$

The oscillation amplitude is larger for electrons due the higher charge to mass ration Ze/m.

A useful parameter can be defined as the dimensionless light amplitude:

$$
a_0 = \frac{eE_0}{\omega m_e c},
\tag{2.9}
$$

m_e is the electron mass. Using this parameter the laser fields can be rewritten:

$$E_0 = a_0 \frac{2\pi m_e c^2}{e\lambda} \quad = \quad \frac{a_0}{\lambda[\mu m]} 3.2 \times 10^{12}\,\text{V/m} \tag{2.10}$$

$$B_0 = a_0 \frac{2\pi m_e c}{e\lambda} \quad = \quad \frac{a_0}{\lambda[\mu m]} 1.07 \times 10^7\,\text{T}$$

$$I = a_0^2 2\varepsilon_0 c \left(\frac{2\pi m_e c^2}{e\lambda} \right) \quad = \quad \frac{a_0^2}{\lambda^2[\mu m^2]} 1.37 \times 10^{18}\,\text{W/cm}^2.$$

The oscillation amplitude and velocities become for electrons:

$$s_0 \simeq a_0 \frac{\lambda}{2\pi} \quad \text{and} \quad |\vec{v}| \simeq a_0 c. \tag{2.11}$$

The motion becomes relativistic when a_0 nears unity. For a laser wavelength of $\lambda \simeq$ 1 μm an intensity of $10^{18}\,\text{W/cm}^2$ is needed to reach the relativistic threshold.

Three different effects start to play a role. At first, the electron oscillation velocity approaches in every light cycle the speed of light. The average mass of the electron increases hereby. The motion of the electron becomes anharmonic, the relation 2.8 for the maximal transverse amplitude remains valid. Finally, a forward drift occurs. The reason therefore is that the magnetic field of the laser cannot be neglected any more in equation 2.7 at relativistic intensities. The figure of motion described now by the electron is complicated but still periodical. The electron figure of motion in frame moving with the averaged drift velocity in the laser propagation direction resembles a shape of an 8 (2.1(b)). The cross product of the transverse velocity and the magnetic field leads to a forward drift. The mean drift velocity is

$$\vec{v_D} = \frac{a_0^2}{4 + a_0^2} c \vec{e_z}. \tag{2.12}$$

Despite of having a high kinetic energy during the laser pulse duration, the net electron energy gain is zero. As soon the laser pulse has overtaken the electron this forward motion will cease. The electron has just drifted some distance in the laser propagation direction (2.1(c)). This effect is valid just for a planar wave of finite pulse length.

Taking into account the transverse profile of the laser and assuming a focused laser beam (as typically used in experiments to reach high intensities), electrons can gain energy. This can be understood qualitatively by using the following picture: During one half of laser oscillation, the electron is pushed away from the laser axis into an area with less intensity. In the second half of the oscillation, the electron is pushed back
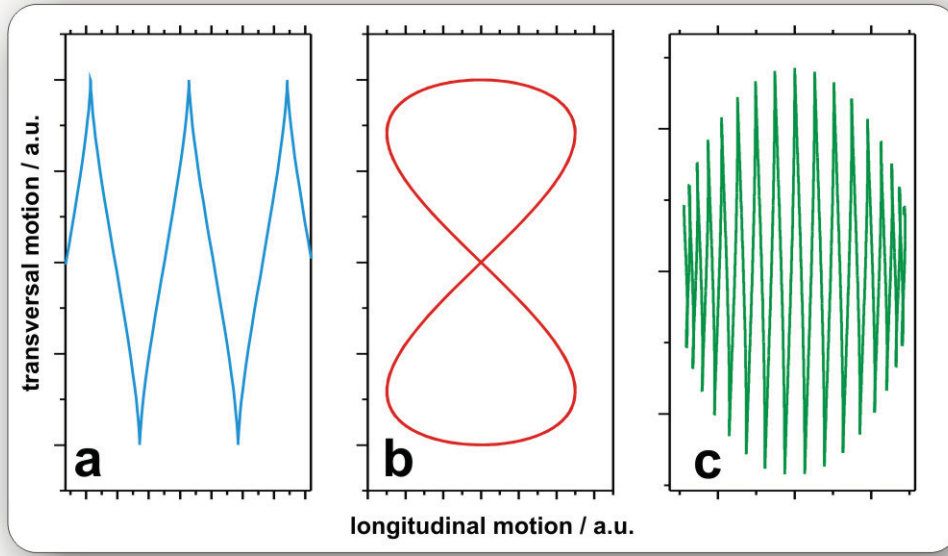
Figure 2.1: Relativistic motion of an electron in the laser field **(a)** in the laboratory reference frame , **(b)** in the drift reference frame , **(c)** for a finite planar laser pulse.

towards the laser axis by a weaker force and gets therefore not back to the original position.

This effect can be described quantitatively by introducing a pseudo potential, the ponderomotive potential given by:

$$\Phi_P = \frac{m_e c^2}{4\overline{\gamma}} a_0^2, \tag{2.13}$$

with $\overline{\gamma}$ the averaged $\gamma-$factor over an oscillation. Electrons slide down the potential, the associated ponderomotive force is $F_P = -\nabla\Phi_P$.

Focusing the laser leads also to another effect: While the unfocused laser has just transverse field components this situation changes. A focused beam exhibits longitudinal fields. An electron can gain directly energy in these fields. The angle at which the electron leaves the laser focal region is a function of the end energy. For an electron with zero start energy Quesnel and Mora find [29]:

$$\cos\theta \simeq \sqrt{\frac{\gamma - 1}{\gamma + 1}}. \tag{2.14}$$

Electrons are expelled from high intensity regions, the kinetic energy gained is of the order of magnitude of the ponderomotive potential.

2.4   Laser Plasma Coupling

The previous sections showed how a high intensity laser pulses ionizes matter and the motion of the hereby freed electrons in the light wave. This behavior changes, as soon the laser interacts with a plasma. The first effect is that electrons are pushed out of the laser focus in all directions. Many electrons respond in a similar way to the influence of the external laser field, the plasma particles reorder, positive and negative charges separate and internal plasma fields are created.

The microscopic electron motion leads to macroscopic effects: high intensity laser light propagation in a plasma will strongly affect the plasma density and geometry, then again the plasma will affect the laser propagation.

The plasma properties are mostly given by the free electrons viz. from the electron density and plasma electron frequency:

$$\omega_p = \sqrt{\frac{e^2 n_e}{\varepsilon_0 \overline{\gamma} m_e}}. \tag{2.15}$$

The plasma electron frequency is the resonant frequency of electron collective oscillation against the ion background. Is the plasma frequency larger than the laser frequency $\omega_p > \omega_L$, then we have an overdense or overcritical plasma. If the electron density n_e is less than the so called critical density

$$n_c = \frac{\omega_L^2 \varepsilon \overline{\gamma} m_e}{e^2}, \tag{2.16}$$

then we have the case $\omega_p < \omega_L$ called an underdense or undercritical plasma. Light can propagate, the phase and group velocity are given by:

$$v_p = \frac{c}{n_p} \quad \text{and} \quad v_g = c n_p, \quad \text{with} \quad n_p = \sqrt{1 - \frac{\omega_p^2}{\omega_L^2}}, \tag{2.17}$$

where n_p is the plasma refraction index.

Only now due to the collective nature of the plasma response to the influence of an electromagnetic wave, particle acceleration to energies far beyond the ponderomotive potential becomes possible as discussed in the next sections.

2.5 Particle Acceleration

2.5.1 Electron Acceleration

Although the huge strength of the electric fields generated at relativistic intensity these fields are highly oscillatory and they are orientated transverse to the propagation direction of the laser pulse. Due to collective plasma effects transverse laser field energy can be transformed in a longitudinal field making particle acceleration to energies higher than the ponderomotive potential possible. One can distinguish between effects that are associated with the transmission of a laser pulse in an underdense plasma or with the absorption of a laser pulse in an overdense plasma.

Electron Acceleration in the underdense Plasma Regime

One of the most impressive collective plasma effects leading to electron acceleration is the so called LASER WAKE FIELD ACCELERATION (LWFA) proposed by Tajima and Dawson [30] already in 1979. They made use of the Langmuir type electrostatic wave exited in the wake of a laser pulse propagating in an underdense plasma. The excited electric field is longitudinal and its frequency ω_{pe} does not depend on the laser pulse wave vector. This means that the group velocity of the Langmuir wave in a cold plasma is zero and the plasma wave keeps the position in the plasma for a long time making charged particle acceleration possible. At the same time the plasma phase velocity equals the group velocity of the driving laser pulse that is close to the speed of light. Such a plasma wake is most effectively generated if the length of the driving electromagnetic wave is half the wavelength of the plasma wave. Electrons will be accelerated by the longitudinal field up to the time when their velocity is higher than the plasma wave phase velocity. Then they overtake the plasma wave and get decelerated because of the inverse field polarity. The maximal acceleration length is known as dephasing length $l_d = 2\omega^2 c/\omega_p^3$ and can be increased by lowering the plasma density. By using this mechanism energies up to 1 GeV have been achieved in [31] by using a 3 cm long plasma. If the laser pulse driving the wake wave is too large wakefield breaking will occur leading to a new physical situation called the BUBBLE ACCELERATION regime [32]. In the extreme case the first plasma wake wave will break both parallel and transverse to the laser propagation direction leading to both self modulation of the laser pulse and electron acceleration. Because the electron acceleration takes place

just in one plasma wake the accelerated electrons have a spectrum that is intrinsically mono-energetic ([33, 34, 35]). In the interaction between a ns long laser pulse and matter the inverse Bremsstrahlung (a collisional based process) and the Stimulated Raman and Brillouin Scattering (instability based processes) play a very important role. Details of these absorption processes that can be neglected in the context of this work can be found in [36].

Electron Acceleration in the overdense Plasma Regime

To understand the interaction of a light wave with an overdense plasma one has to study the wave equation describing the laser pulse transport:

$$\nabla^2 \vec{E} - \nabla(\nabla \vec{E}) + \frac{\omega^2}{c^2} \left(1 - \frac{\omega_p}{\omega_L} \right) \vec{E} = 0.$$

For a linear rising electron density preformed plasma $n_e(z) = n_c \frac{z}{L}$ and an angle θ between incoming beam and the normal to target surface the equation becomes:

$$\frac{d^2 E(\zeta)}{d\zeta^2} - \zeta E(\zeta) = 0, \tag{2.18}$$

with $\zeta = \sqrt[3]{\frac{\omega^2}{c^2 L}}(z - L)$. This equation is known as Stokes differential equation and can be solved by the Airy functions Ai and Bi. The solution is a standing wave created by the incoming and the reflected wave. The point of reflection is found where the density reaches $n_c \cdot \cos(\theta)$. Still a part of the electric field will tunnel behind the reflection point and close to the critical density [36]. Here an electron plasma wave is driven resonantly, .i.e. $\omega_p e = \omega_L$ by the field component parallel to the electron density gradient. The plasma wave grows until wave breaking leads to production of an over-thermal electron population effect known as RESONANCE ABSORPTION [37] . Typical for resonance absorption is the production of electron bunches each full laser cycle. The temperature scaling is found in [38] according to

$$T_{res} = 0.1 \times \left(\frac{I \lambda_L^2}{10^{17} \text{W/cm}^2} \right)^{1/3} \text{MeV}. \tag{2.19}$$

When using a high contrast sub ps laser pulse the preformed plasma scale length may be close to the wavelength of the laser employed and high density electrons can be directly accelerated by the laser pulse. In this case play two absorption effects a major role. The first the BRUNEL TYPE ABSORPTION also known as VACUUM HEATING can

be described as follows [39]: A p-polarized pulse with oblique incidence on a step density gradient interacts with the electrons at the critical surface. In the first half cycle of the laser oscillation the laser pulse pulls out an electron from the target into vacuum. In the second half cycle the electron is pushed back into the target. If the electron is fast enough not to be stopped over the plasma skin depth the oscillatory motion at the critical density will cease as no laser field is present in the overdense plasma to pull back the electron towards the vacuum. In such a way electrons are accelerated in bunches once per laser cycle and are directed normal to the target surface.

The second mechanism which gains in relevance at relativistic intensities is the so called $j \times B$-HEATING. It originates from a theoretical publication of Wilks [40]. From the section 2.3 we know that an electron will be accelerated forwards parallel to the laser propagation direction twice per laser cycle. Without a plasma the net energy gain is zero. If the electrons are pushed into an overdense plasma region the laser electric field will not decelerate them leading to a net energy gain. Wilks gives a scaling for the expected electron temperature:

$$T_h \simeq mc^2 \left(\gamma - 1 \right) = 0.511 \left[\left(1 + \frac{I \lambda_L^2}{1.37 \times 10^{18} \mathrm{W/cm}^2} \right)^{1/2} - 1 \right] \ \mathrm{MeV}. \qquad (2.20)$$

Normal laser incidence on to the target is favorable for this electron heating mechanism.

The acceleration of electrons leads to the generation of a charge imbalance. The plasma ions are heavier and cannot follow the electrons due to their inertia. The excitement of high electric fields in the plasma is the result. These fields created by the interplay of the hot electrons with the cold ion background leads to efficient ion acceleration, physical processes described more in detail in the next section.

2.5.2 Proton and heavy Ion Acceleration

The irradiation of a thin over-critical foils has led to the discovery of proton and ion acceleration from an expanding plasma. An initial controversy about the origin of these ion beams is in the meantime solved. Two ion population can be distinguished: ions accelerated from the front surface of the foil (the one directly irradiated by the laser pulse) and ions accelerated from the rear surface.

Ions from the front

The protons originating from the front surface are directly accelerated by the inter-action between the laser pulse and the target front surface. Sentoku develops in [41] a model and gives an estimate for the maximal possible energy to be gained by these protons. For laser pulse intensities higher than 10^{18} W/cm^2 the relativistic character of the accelerated electrons pushes the critical plasma density towards the target surface. The ponderomotive force pushes the electrons that regroup in front of the laser pulse. The strength of the emerging electrostatic potential associated to the charge separation is of the order of the ponderomotive potential and accelerates protons and ions towards the target. The maximum energy gained is a function of the laser pulse length and the ion acceleration time, and is for laser pulses long compared to the acceleration time of the ions maximal of the order of the ponderomotive potential.

Ion acceleration from the front has been already reported for sub relativistic pulse intensities [42]. A high power CO_2 laser pulse produces in this case an expanding isotropic electron population. The heavy ion background follow the electrons driven by the subsequent charge separation in an ambipolar expansion gaining a temperature of $T_i \simeq 2T_e$. Characteristic for this ion acceleration is a beam divergence of 2π.

Ions from the rear

The ions accelerated from the rear side of the target are the result of the propagation of hot electrons through the target. The acceleration mechanism can be described as follows. The laser pulse accelerates a hot electron population that is fast enough to propagate through the target without being stopped [43, 44]. At the rear side of the target these electrons will generate a charge separation that is of the order of the Debye scale length, typically of μm in size. The electrostatic field created due to the charge imbalance has a characteristic field strength of TV/m and will ionize

the surface of the target and accelerate perpendicular to the surface ions. A plasma expansion driven by a hot electron Debye sheath follows. The hot electron energy is transferred bit by bit to the ions up to the time where the ion acceleration stops due to cooling of the hot electrons. In the year 2000 several experiments reported for the first time the observation of a highly collimated $E_{max} > 10$ MeV energy proton beam [2], [4], [3]. The proton beam had an exponential decaying energy spectrum with maximal energies between 10 and 55 MeV, the divergence angle getting smaller for higher proton energies. After these discoveries the results were reproduced and extended by various groups using wide range of laser and target parameters some summarized in table 2.1. The proton origin dispute is solved by Fuchs et al. in [49]. The author shows that

Laser System	τ(ps)	E_{laser} /J	I/(Wcm^{-2})	L/μm	E_{max} /MeV
NOVA PW [3]	.5	200	3×10^{20}	100	58
RAL PW [45]	.7	400	3×10^{20}	100	44
RAL Vulcan [46]	1	90	1×10^{20}	10	36
LULI 100TW [47]	.32	30	6×10^{19}	20	20
LOA [48]	.04	0.8	6×10^{19}	6	8

Table 2.1: Summary of various experimental parameters of laser proton acceleration studies. The NOVA PW energy record still holds today. The laser pulse duration, the pulse energy, focused irradiance, target thickness and maximal proton energy are given.

front and rear size proton acceleration are parallel occurring processes and the rear side acceleration dominates in both particle numbers and energies to the front side acceleration. In experiment just 3% of the protons were accelerated from the front. One particular property of the proton beam accelerated from the rear target surface is the laminarity and the small virtual source size. By using structured targets Cowan et al. [11] showed that for proton energies >10 MeV, the transverse and longitudinal emittance is at least 100-fold and may be as much as 10^4-fold better than conventional accelerator beams and the ion beam source size is measured to be less than 15 μm (FWHM) for proton energies >10 MeV. Hegelich et al. demonstrate in [50] that by careful cleaning of the metallic foils used for proton acceleration the proton beam is suppressed and a heavy ion beam can be efficiently accelerated. The usual measured protons are originating from the impurities (hydrocarbons and water) on the metal foil surface.

Target Sheath Normal Acceleration

After the first experimental demonstration theoretical studies have progressed the understanding of laser proton acceleration. The TARGET SHEATH NORMAL ACCELERATION model has proven to describe best the physical situation at the rear side of the irradiated foil. This model is also known as PLASMA EXPANSION INTO VACUUM and is based on the early work of Gurevich [51]. P. Mora applies this model in [52] and [53] to the motion of a relativistic electron fluid, and finds a self similar solution describing the plasma time evolution and subsequent proton acceleration. The details are summarized in the next paragraphs:

After traversing the thin foil the hot electrons accelerated by the laser pulse are distributed corresponding to their energy distribution. The Mora model assumes a semi infinite plasma. At $t = 0$ we have a physical situation where for $x < 0$ we have a constant ion density $n_i = n_{i0}$ and cold ions with $T_i = 0$. A sharp vacuum interface extends from $x > 0$ with $n_i = 0$. On the other hand the electron density is continuous and has the form of a Boltzmann distribution as illustrated in figure 2.2:

$$n_e = n_{e0} \exp\left(\frac{e\Phi}{k_B T_e}\right)$$

with n_{e0} denoting the electron density of the undisturbed plasma at $x = -\infty$, Φ is the electrostatic potential and T_e is the hot electron temperature. The boundary conditions at $x = -\infty$ impose also $\Phi = 0$ and the quasi-neutrality $n_{e0} = Zn_{i0}$, with Z the ion charge state.
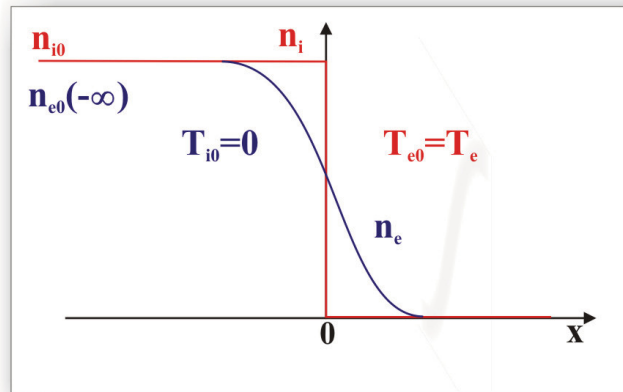

Figure 2.2: Initial conditions for the plasma expansion in vacuum.

The potential Φ obeys the Poisson equation

$$\epsilon_0 \frac{\partial^2 \Phi}{\partial x^2} = e(n_e - Z n_i). \tag{2.21}$$

Integration between $x = 0$ and $x = \infty$ yields a simple expression for the electric field strength built up at the plasma vacuum interface at $x = 0$:

$$E_{front,0} = \sqrt{2/e} E_0, \text{ with } E_0 = \sqrt{n_{e0} k_B T_e / \epsilon_0}. \tag{2.22}$$

The initial electric field is a function of the density, the hot electron temperature, a sharp plasma vacuum boundary and high intensity laser pulses are necessary for efficient acceleration.

The electron motion is balanced by the electrostatic potential Φ for $t > 0$. The ion expansion can be described with the continuity and motion equations:

$$\left(\frac{\partial}{\partial t} + v_i \frac{\partial}{\partial x} \right) n_i = -n_i \frac{\partial v_i}{\partial x}, \tag{2.23}$$

$$\left(\frac{\partial}{\partial t} + v_i \frac{\partial}{\partial x} \right) v_i = -\left(\frac{Ze}{m_i} \right) \frac{\partial \Phi}{\partial x}, \tag{2.24}$$

where v_i denotes the ion velocity. Mora finds a self similar solution for $x + c_s t > 0$ while assuming the quasi-neutrality of the expanding plasma: From $n_e = Z n_i = n_{e0} \exp(-x/c_s t - 1)$, $v_i = c_s + x/t$ follows:

$$E_{ss} = \frac{k_B T_e}{e c_s t} = E_0 / \omega_{pi} t \tag{2.25}$$

where the subscript ss denotes the self similar solution, $c_s = (Z k_B T_e / m_i)^{1/2}$ the ion-acoustic velocity and $\omega_{pi} = (n_{e0} Z e^2 / m_i \epsilon_0)^{1/2}$ the ion plasma frequency. The self similar electric field solution is the result of a positive charge $\sigma = \epsilon_0 E_{ss}$ at $x = -c_s t$ and a negative charge $-\sigma$ at the plasma front. The self similar solution does not hold if the Debye-length:

$$\lambda_{D0} = (\epsilon_0 k_B T_e / n_{e0} e^2)^{1/2}$$

is larger than the typical length $c_s t$ of the self similar solution or $\omega_{pi} t < 1$. A limitation of this isothermal solution is the diverging speed gained by the ions for $x \to \infty$. A rough estimation of the position of the ion front can be obtained by noting that the self-similar solution becomes invalid when the local Debye length, $\lambda_D = \lambda_{D0}(n_{e0}/n_e)^{1/2} = \lambda_{D0} \exp[(1 + x/c_s t)/2]$ equals the density scale length $c_s t$. This position corresponds to $1 + x/c_s t = 2 \ln(\omega_{pi} t)$. At this point the self-similar solution predicts a velocity

$v_{i,front} = 2c_s \ln(\omega_{pi}t)$. Note that this implies that the electric field at the ion front is twice the self-similar field E_{ss}:

$$E_{front} \simeq 2E_{ss} = 2E_0/\omega_{pi}t. \tag{2.26}$$

For supporting this findings Mora presents numerical results by solving the Poisson, the continuity and the motion equations with a Lagrangian code. Figure 2.3 shows the
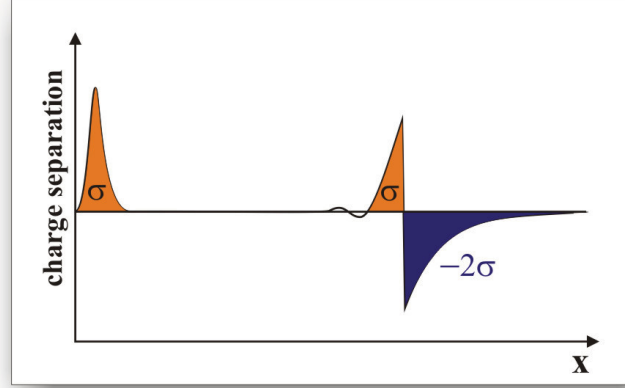

Figure 2.3: Charge separation evolution as predicted in [52]

computed time evolution of the charge separation. At the position $x = -c_s t$ where the expansion starts a surplus of net positive charge is built up. The expanding front consists of a -2σ charge of electrons that drag a charge σ of ions. The corresponding electric field distribution is shown in figure 2.4.

The electric field rises up to E_{ss} to stay constant up to the position of the ion front where it rises fast to $2E_{ss}$ to drop afterwards exponentially. Mora computes a interpolation formula for the time evolution of the field strength:

$$E_{front} \simeq 2E_0/(2e + \omega_{pi}^2 t^2)^{1/2} \tag{2.27}$$

with $e = 2.71828$.

By integrating in time the equations $dv_{front}/dt = ZeE_{front}/m_i$ and $dx_{front}/dt = v_{front}$ using E_0 from 2.27, taking the asymptotic evolution for the limit $\omega_{pi}t \gg 1$ one obtains the ion front velocity and position:

$$\begin{aligned}
v_{front} &\simeq 2c_s \ln(2\tau) = c_s[2\ln(\omega_{pi}t) + \ln 2 - 1] & (2.28)\\
x_{front} &\simeq 2\sqrt{2e}\lambda_{D0}\tau[\ln(2\tau) - 1] \\
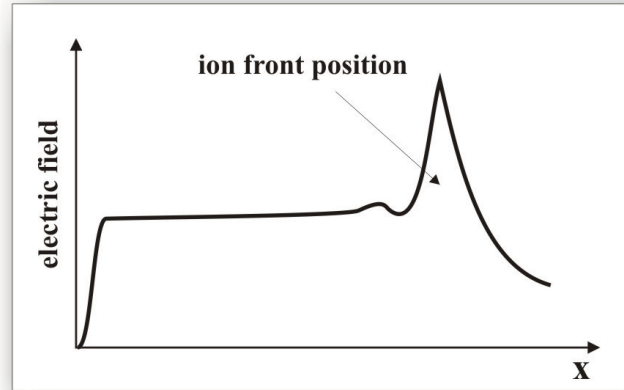&= c_s t[2\ln(\omega_{pi}t) + \ln 2 - 3] & (2.29)
\end{aligned}$$

Figure 2.4: Electric field distribution corresponding to the charge separation in Fig. 2.3

with $\tau = \omega_{pi} t / \sqrt{2e}$. A very important prediction of the model is the exponential shape of the energy spectrum:

$$\frac{dN}{d\mathcal{E}} = \frac{n_{i0} c_s t}{\sqrt{2\mathcal{E}\mathcal{E}_0}} \exp{-\sqrt{2\mathcal{E}/\mathcal{E}_0}}, \qquad (2.30)$$

whit $\mathcal{E}_0 = Zk_B T_e$. The cut off energy is estimated from 2.28 by stopping the acceleration at a time τ: $\mathcal{E}_{max} \simeq 2\mathcal{E}_0[\ln(2\tau)]^2$. A natural choice of this cut off time is the employed laser pulse duration. Indeed by comparing experimental results, computational PIC results and the analytical solution for the maximal energy Fuchs et al. finds in [54] a cut off time $\tau = 1.3 \times \tau_{laser}$. The isothermal model was extended by Mora in [53] to include the effects of hot electron cooling. He finds that the peak to plateau electric field ratio of 2 from the isothermal model changes to rise linearly in time, E_{ss} dropping now with $\propto t^{-3}$ while $E_{front} \propto t^{-2}$. This double layer electric field structure was experimentally discovered by Romagnani et al. [55] in an experiment investigating the acceleration of multi-MeV protons from the rear surface of thin solid foils irradiated by an intense and short laser pulse by means of using transverse proton probing. The structure of the electric field driving the expansion of the proton beam has been resolved with high spatial and temporal resolution. The main features of the experimental observations (see figure 2.5), namely an initial intense sheath field and a late time field peaking at the beam front, are consistent with the results of the thin plasma expansion into vacuum.

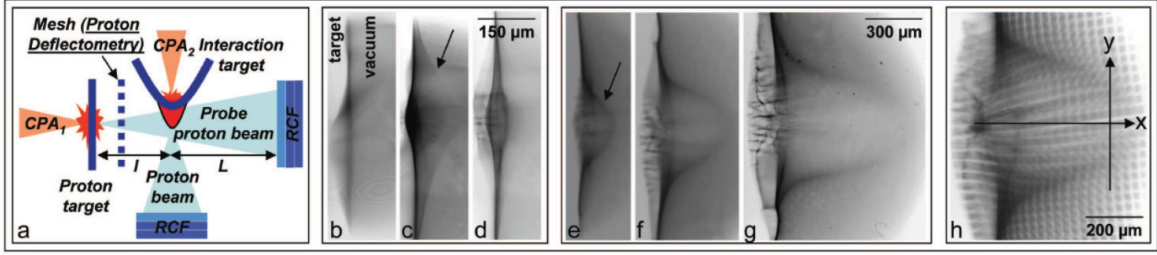The acceleration of MeV ions from the interaction of high-intensity laser-pulses with

Figure 2.5: a. Experimental set-up used in [55]. b-g. Proton Imaging data at probing times $-4, 0, 3, 7, 13$ and 25 ps respectively. h. Proton Deflectometry data at 11 ps. The magnification was 30 in (b-d) and 15 in (e-h). The scales refer to the object plane. The initial intense Debye sheath field (pointed at by an arrow in (c)), and a late time field peaking at the beam front (pointed at by an arrow in (e)) have been probed for the first time directly.

thin solids has major applicative prospects due to the high beam quality of these ion bursts [10], [11]. Such proton beams are already applied to produce high energy density matter [12] or to radiograph transient processes [13], and offer high prospects for tumour therapy [14], isotope generation for positron emission tomography [15], fast ignition of fusion cores [16] and brightness increase of conventional accelerators. However, as these proton beams are poly-energetic and divergent at the source, reduction and control of their divergence and energy spread are essential requirements for most of these applications. The next section will give a status quo of the efforts of the laser particle acceleration community on the way to meet the above mentioned requirements.

2.5.3 Status Quo: Ion Beam Focusing and Energy Selection

Focusing of energetic proton beams is usually achieved using electrostatic or magnetic lenses [17] that have several drawbacks, namely: slow switching times, large sizes, asymmetry in the transverse plane for the focused beam, aberrations, inability to focus large currents, and large heat dissipation. It has been proposed that particle selection and beam collimation of laser produced protons applicable for tumour therapy could be achieved by means of a superconducting magnet system [18]. Relativistic laser-plasma devices appear in principle more suitable to achieve the required angular and spectral control of laser-accelerated ion beams since they can withstand large ion beam currents, can be switched over ps time scales, and can support large deflecting fields on micro-scales. Patel et al. [12] reports that geometrical focusing of laser-driven protons has been achieved by using spherically shaped laser targets to produce a focused proton beam.

Parallel to this work the energy selection has been reported from laser irradiated micro-structured targets. Two papers recently published in Nature are similar and deal with the production of laser produced quasi-monoenergetic heavy ion [19] and proton [20] beams by target engineering. This is achieved by placing controlled layers of particular compounds on the solid target rear surface and by removing the contaminants that are otherwise present on the target surfaces, using either laser ablation or resistive heating of the target. From the analysis presented by the authors of the two papers, they succeeded in the production of quasi-monoenergetic beams either by the use of a thin compound layer in the target [19] or by the use of a thin dot with a limited spatial extend [20].

These techniques have however limitations. For example: i) micro-structured target techniques demand extreme control in the target production and interaction environment, and focusing of the proton/ion beam has still to be demonstrated, ii) in case that the energy-dependence of the focal length of curved targets is demonstrated, energy selection with this scheme would involve transverse spatial filtering close to the surface, iii) curved targets cannot be used to transport, collimate and focus an externally generated beam, iv) the focusing possibility of curved targets has not been demonstrated over the mm range yet, and v) target debris contamination of the ion focus region cannot be avoided.

An other technique using a target of limited spatial extension is the production of quasi mono-energetic deuteron bursts as reported by [56]. Here a quasi mono-energetic

peak within the ion energy spectrum was observed when heavy-water microdroplets were irradiated with ultrashort laser pulses of about 40 fs duration and high (10^8) temporal contrast, at an intensity of 10^{19} W/cm^2.

A new scheme demonstrated by Nakamura et al. in [57] is the combination of the conventional RF acceleration technique with laser-produced protons to improve the spectral properties of the laser accelerated protons. A short-pulse high-power (210 fs and 1 TW) laser was focused on a tape target 3 to 5 μm in thickness. Protons produced by this laser with an energy spread of 100 % were found to be improved to create peaks in the energy distribution with a spread of 7 % by the application of the RF electric field with an amplitude of ±40 kV synchronous to the pulsed laser. The authors found to have good reproducibility for every laser shot with the capability of adjusting the peak positions by control of the relative phase between the pulsed laser and the RF electric field at 10 Hz operation.

The focusing and energy selection technique reported in this work also decouples the beam production stage from the beam tailoring stage. Therefore it reduces the target production demands. The bulk target material is commercially available and has just to be cut into the desired dimensions. Using two targets has also the advantage of independently optimizing the beam production or the beam tailoring stage in respect to specific applications. The need of a second laser beam to trigger the micro-lens does not increase the laser demands. A beam with 0.1 the energy beam can be easily split of proton production beam and is intrinsic optically synchronized.

2.5.4   Perspectives of laser proton acceleration

The past few years have seen remarkable progress in the development of laser-based particle accelerators. The ability to produce ultra-bright beams of multi mega electronvolt protons routinely has many potential uses from engineering to medicine, but for this potential to be realized substantial improvements in the performances of these devices must be made. The determination of the scaling laws is a necessary step to achieve this optimization. Fuchs et al. compares in [54] experimental deduced scaling laws with the prediction of a simple fluid-based model of proton acceleration. This enables the evaluation of the laser parameters needed to produce high-energy and high-quality proton beams of interest for radiography of dense objects or proton therapy of deep-seated tumours. Schreiber et al. present in [58] a general analytical expression for the maximum ion energies observed in experiments with thin foils irradiated by

high-intensity laser pulses. The model is based on a radially confined surface charge set up by laser accelerated electrons on the target rear side. The only input parameters are the properties of the laser pulse and the target thickness. Both Fuchs and Schreiber conclude that a 200 MeV beam could be accelerated with a PW level laser with an optimal duration of 150-200 fs (see figure 2.6). Beside the Target Normal Sheath Accel-
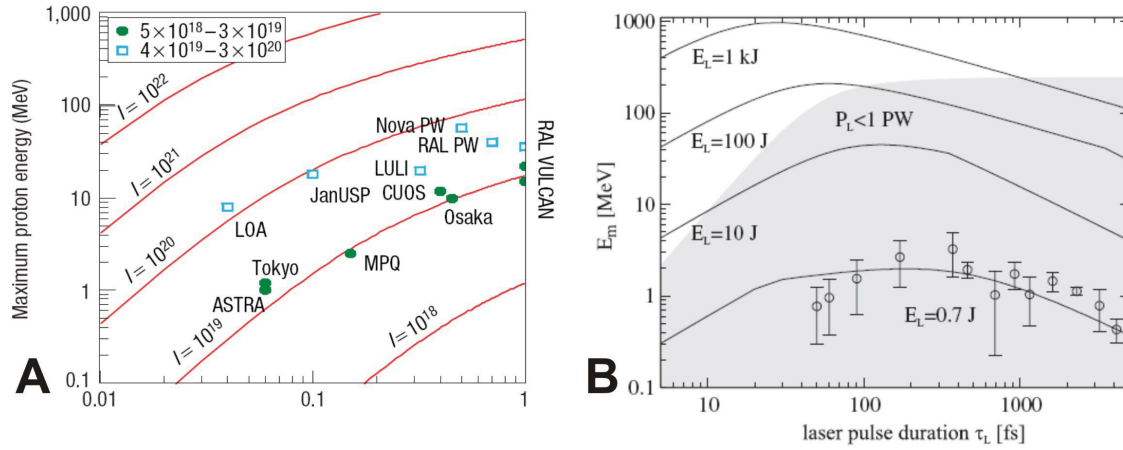

Figure 2.6: Scaling of the expected proton energy as a function of pulse length and energy A) from Fuchs et al., Nature Physics (2005) and B) from Schreiber et al. Phys. Rev. Lett. 97 (2006)

eration exploited by the above mentioned authors other paths for pursuing the increase of the maximal accelerated energy have been reported. Antici reports in [59] that a new regime of laser acceleration of protons, which relies on the interaction of ultrahigh contrast laser pulses with ultrathin targets, has been validated using experiments and simulations. Proton beams were accelerated to a maximum energy of 7.3 MeV from targets as thin as 30 nm irradiated at 10^{18} W/cm^2 with an estimated peak laser pulse to pedestal intensity contrast ratio of 10^{11}. This represents nearly a tenfold increase in proton energy compared to the highest energies obtainable using non contrast enhanced pulses and thicker targets 5 μm at the same intensity. Beside the reduction in thickness of the targets also a global reduction of the mass of the targets is followed. First results show a stronger electron confinement to the target and thus a stronger electric field leading to enhanced acceleration (priv. comm J. Schreiber, M Hegelich and T. Cowan).

2.6   The electron fountain effect

While the TNSA proton acceleration model presented above was one dimensional in reality the physical processes take place in three dimensions. Especially the propagation of the hot electrons in front, through and at the rear side of the target is dominated by the higher dimensionality. As a result the proton acceleration field is spatially irregular. Associated with the hot electron motion is the buildup of a strong magnetic field structure. Inside the target the hot electron current is compensated by a cold electron collisional current and underlies the Weibel instability [60]. The beam filaments and the spatial separation of the forward and return currents generates an azimuthal magnetic field effect that has been extensively studied both experimentally [61, 62, 63, 64, 65] and theoretically [66, 67, 68].

As soon as the hot electrons will exit into vacuum from the plasma rear surface, a 'fountain' like effect leads to large-scale azimuthal magnetic field generation in the nearest vicinity of the surface [69]. The generated magnetic fields computed by Pukhov are of the order of 10 MG. This fountain like motion of the hot electrons has been stud-
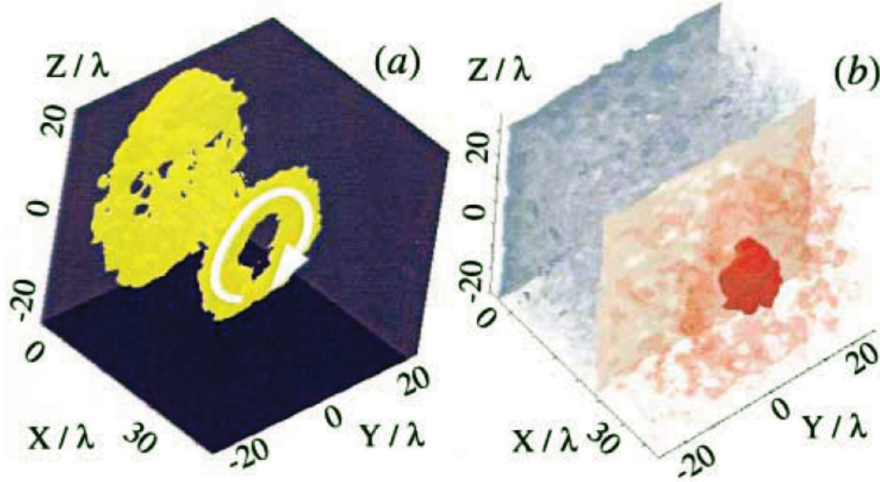

Figure 2.7: 3D perspective views from [69] (a) Quasistatic magnetic field, the isosurface $|B| = 10$ MG is shown; the white arrow shows the field direction. (b) The accelerating electrostatic field isosurfaces is shown at normalized values of: -0.05 (blue), 0.05 (light red); the dark red blob in the middle marks the Debye sheath with the highest electric field of 0.1

ied more in detail in [70] by Nakamura and Sentoku [71] and is summarized as follows:

In an initial stage at the back side of the interaction region the electrons will build up strong electric Debye-sheath field E_s. A fraction of the electrons will be electrostatic trapped thus returning toward the surface. As a result of the spring fountain like motion of electrons a strong magnetic azimuthal field $B_\circlearrowleft$ is excited perpendicular to the plane of motion. This field propagates at the speed of light following the hot non collisional electrons. At the same time the electrons are pushed sideways by the Lorentz force in the direction of $E_s \times B_\circlearrowleft$ increasing the extension of these fields. A similar hot electron motion is occurring also at the front side of the target and leads also to a hot electron propagation along the target surface.

This effect is of special importance for this work because it will be identified as the mechanisms responsible for the heating of the plasma driving the laser triggered micro-lens.

2.7   Stopping of ions in matter

The next section of this introductory chapter describes how the laser produced protons interact with matter. Radiation looses intensity during the passage through matter (target). Depending on the type of radiation one can distinguish: Heavy particles moving in average with sub-relativistic velocities loose their energies mostly by ionization of the target. Light particles like electrons and hadrons with relativistic velocities release their energies in form of electromagnetic radiation. Of great interest for this work is the slowing down of ions in matter. While moving through the target, the particles can collide both with the electrons and the ions of the target. The total absorption cross section is obtained by adding an electronic and atomic contribution. The electronic part consists of several terms [72]:

1. Direct energy transfer due to collision with electrons
2. Excitation and ionization of the target atoms
3. Excitation of band or conduction electrons
4. Excitation, ionization and electron capture by the ionizing particle.

The atomic contribution to the total cross section describes the energy loss to the target nuclei. This contribution is 10^3 times smaller than the electronic cross section for the energy range of the ions produced during this work and can therefore be neglected. No complete theories exists describing the absorption cross section for a given particle pair. There are three approximations that cover three different energy ranges:

1. The velocity for energies lower than 10 MeV/amu is similar to the velocity of the target electrons. In this case the interaction between single target atoms must be considered. The Lindhart approximation is valid for low energy collisions and models the target as an electron plasma.

2. The Bethe Bloch theory is valid for medium energies 10 MeV/amu up to 1 TeV/amu. The energy transfer is modeled as scattering between a charged particle with a single atom.

3. For energies higher than 1 TeV/amu radiative processes like bremsstrahlung and pair creation play the major role.

The Bethe-Bloch equation describes the energy loss per length for a certain particle:

$$-\frac{dE}{dx} = Kz^2 \frac{Z}{A} \frac{1}{\beta}^2 \left[\frac{1}{2} \ln \frac{2m_e c^2 \beta^2 \gamma^2 T_{max}}{I^2} - \beta^2 - \frac{\delta}{2} \right] \tag{2.31}$$

with $T_{max} = 2m_e c^2 \beta^2 \gamma^2 / (1 + 2\gamma m_e/M + (m_e/M)^2)$. T_{max} is the maximal kinetic energy

that can be transferred by the projectile to a free electron. M is the mass of the projectile, Z the charge number, A the atomic number of the target and z the charge state of the projectile. β and γ are the usual relativistic parameters, $K = 4\pi N_A r_e^2 m_e c^2$, I is the average ionization energy and δ a density correction factor. This equation is valid up to 1% error for proton energies in the range from 1 to 100 MeV.

2.7.1   SRIM

The Bethe Bloch equation has not been solved directly. A programm group named SRIM (The Stopping and the Range of Ions in Matter) developed by J. Ziegler [73] has been used to compute the stopping and straggling of ions in different target materials. SRIM is used in a very simple geometry. Foils of different thicknesses can be stacked. Starting from a point source the propagation of an ion beam through these foils can be simulated. SRIM has been used to compute the energy deposition in the detectors to be presented in chapter 3. Figure 2.8 shows exemplary a SRIM computation of the stopping of 10 MeV protons in mylar, a hydrocarbon foil with 1.4 g/cm^3 density. As mentioned by the previous section for this projectile energy range and confirmed by the SRIM computation the electronic contribution to the stopping power dominates the atomic contribution.
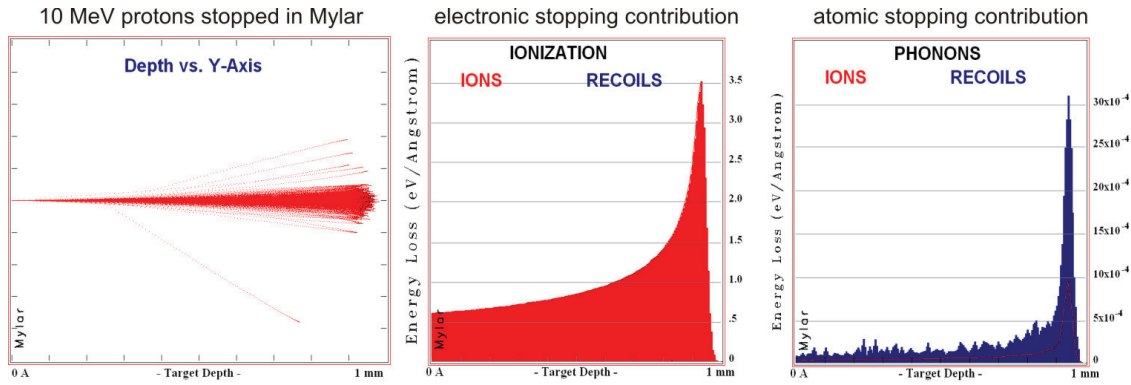

Figure 2.8: SRIM computation of the stopping of 10 MeV protons in mylar a plastic foil. The electronic and and atomic contribution to the stopping power are shown.

2.8 The Monte-Carlo-Particle-In-Cell Plasma Simulation Code PSC

The Plasma Simulation Code (PSC) was used to understand the physical processes creating the proton lens reported in this thesis. PSC is a three-dimensional Monte-Carlo-Particle-In-Cell simulation code kindly provided by Hartmut Ruhl. It uses a Cartesian geometry to solve collisional kinetic plasma equations. The code solves the relativistic Vlasov-Boltzmann equations coupled with the Maxwell equations. It can use an arbitrary number of particle species. The code is designed to be run on distributed computing platforms and is highly parallelized.

We consider a plasma consisting of electrons and ions, which are represented by distribution functions $f_k(\vec{x}, \vec{p}, t)$ with $k = e, i$ for electrons and ions. The distribution function f_k is one of the fundamental parameters of plasma physics giving the probability to find a particle of type k in a given volume of the phase space. All other plasma parameters can be calculated as higher order moments of the distribution function. The motion equation solution of a N particle system taking into account all possible interactions between the particles is known from statistical mechanics as the Liouville equation describing the evolution of the distribution function in the 6N dimensional phase space. This highly dimensional equation can be divided in a set of N lower dimensional equations known as the BBGKY hierarchy after Bogoliubov, Born, Green, Kirkwood and Yvon. The first equation of the BBGKY hierarchy connects the evolution of a one particle distribution function with the two particle distribution function. Stepwise the distribution function of i particles is connected with the distribution function of i+1 particles. The problem of solving this chain of equations is connected with the question where to break it: meaning which higher order effects are to be neglected? In the case of a plasma where the kinetic energy of the particles is very high compared to Coulomb potential between the particles themselves, for example in a high relativistic plasma, the distribution function is affected just by external electromagnetic fields (relativistic intensity laser pulse). The BBGKY hierarchy is cut after the first equation giving the well known kinetic plasma description of the Vlasov equation (left hand side of equation 2.32):

$$\left(\partial_t + \vec{v}_k \partial_{\vec{x}} + q_k \left[\vec{E} + \vec{v_k} \times \vec{B} \right] \partial_{\vec{p_k}} \right) f_k = \sum_{l=n,e,i} \int d^3 p_l v_{kl} \int d\Omega \sigma^{kl} \left(f'_k f'_l - f_k f_l \right). \quad (2.32)$$

This equation gives the total time derivative of the distribution function. It sums up the sources and drains as partial time derivative, diffusion as partial space derivative and the Lorenz-force as velocity derivative. The Vlasov equation holds if the right hand side of equation 2.32 is zero.

In a high density plasma for example solid density or at sub-relativistic energies electrons and ions are subject not just to the influence electromagnetic radiation but also to collisions described by the right hand side of equation 2.32 known also as Boltzmann collisional operator. In this case the BBGKY hierarchy is broken also after the first equation considering any interaction between the particles as a two body effect. In equation 2.32 v_{kl} denotes the relative velocity between particle k and l, Ω the solid angle, σ the scattering cross section, f-s pre-collisional and f'-s are post-collisional distribution functions.

The coupling of the external electro magnetic fields to the plasma particles is given by the Maxwell equations:

$$\partial_t \vec{E} = c^2 \vec{\nabla} \times \vec{B} - \vec{j}/\varepsilon_0 \tag{2.33}$$

$$\partial_t \vec{B} = -\vec{\nabla} \times \vec{E} \tag{2.34}$$

$$\partial_t \rho = -\vec{\nabla} \cdot \vec{j}. \tag{2.35}$$

The charge and current densities are given by

$$\rho = q_e \int d^3 p_e f_e + q_i \int d^3 p_i f_i \text{ and } \vec{j} = q_e \int d^3 p_e \vec{v}_e f_e + q_i \int d^3 p_i \vec{v}_i f_i. \tag{2.36}$$

The numerical scheme adopted by the PSC code to solve the coupled Maxwell-Boltzmann-Vlasov equations is the Monte-Carlo-Particle-In-Cell scheme. The MCPIC method make use of a mesh representation of the Maxwell electromagnetic fields and a finite elements or a quasi-particle representation of the distribution function. The quasi particles can be seen as discrete volume elements in the phase-space corresponding to large number of particles with similar properties. Instead of solving the kinetic equation of N particles a lower number of equations are solved still giving representative results for the whole ensemble.

The MCPIC scheme time loop is described as follows: Before of each time-step increment the collisional part of the code is executed. First new particles are created, since the PSC code includes ionization implemented after the method of [74]. Neutral particles are therefore also included in the code. For the ionization events the ADK rates are evaluated giving the probability of ionization to take place. Then the binary
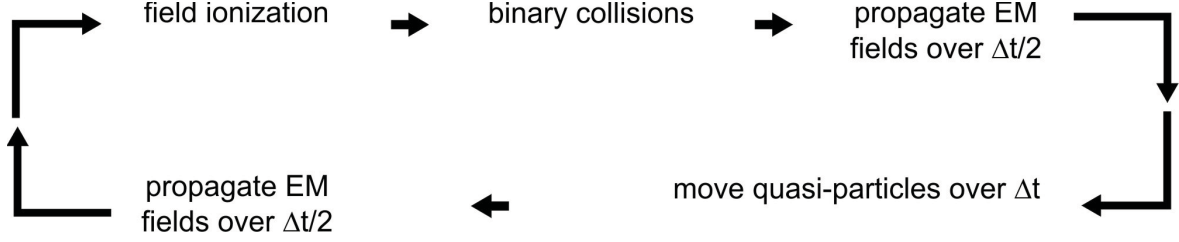
Figure 2.9: Flow chart of the PSC code

collisions are executed with an algorithm containing the Monte-Carlo part of the code. The quasi-particles are paired and random binary momentum transfer is carried out. The Maxwell equations are solved with a Finite-Difference-Time-Domain numerical scheme. In a first step the field evolution at time $t + \Delta t/2$ is calculated. Then the Vlasov equation is solved (for the whole Δt). As a third step the evolution of the Maxwell field at the last half of the time step is calculated taking into account the updated particle distribution. After a predefined number of time steps the state of the simulation is saved giving the possibility to access the computed plasma parameters.

The simulations shown in this work have been carried out on three different computers. First a two AMD Dual Opteron workstation (4 nodes) with 24 Gb RAM was used. For more time intensive tasks the HPC Cluster of the Rechenzentrum of the Heinrich Heine University was used. Here up to 144 Intel EMT64 Xeon nodes or 64 Itanium nodes were used. Later during this work the computational capabilities at the workplace of this thesis were extended by a homemade cluster build up of eight Intel Quad QX6600 with 32 nodes and 64 Gb RAM. The parallelization of the code has been achieved by using the Message Parsing Interface in the version MPICH2 in combination with the Intel Fortran Compiler version 8 or 9 that produced the fastest and most reliable code.

Depending on simulation resolution and size or number of particles computed the computational time of the simulation shown below varied between a few days to 2 months for the finest resolved simulation. Due to computational restriction the PSC code has been run just in 2 dimensional geometry.

Chapter 3

Detectors and Diagnostics

Laser particle sources provide higher currents and shorter bursts than the conventional accelerators. The use of Gafchromic RadioChromic Films (RCF) has been successfully demonstrated for the detection of laser accelerated high energy particles [75], [76]. This films can sustain and detect a high particle flux. Used in stacks these films provide directly a coarse resolution energy detector. Although intensively used by the laser plasma community the lack of an appropriate calibration of the response for protons has led just to different uncertainties. For low flux devices such as dispersive magnetic spectrometers conventional X-ray films or nuclear single particle track detectors as CR39 have been used up to the point of this work. After the successful use of novel Fuji Image Plates (IP) for electron detection at Düsseldorf [35] we have adapted this detection technique for ions and protons. IPs have a higher dynamic range and sensitivity than ordinary films therefore measurements of high resolution proton spectra were possible. Still the response of the IP films was an unknown. Therefore a calibration for both RCFs and IPs has been done at the TANDEM accelerator at the Max Planck Institute for Nuclear Physics Heidelberg. The RCF calibration was successful while during the Image Plate calibration difficulties were encountered making a direct calibration with the protons from the accelerator difficult. Still a cross calibration between Image Plates and RCFs is given. Also part of this chapter will present how RCFs can be used to discriminate between different proton energies. The setup of a magnetic spectrometer used during this work is described. At the end of this chapter the proton imaging as a transient electric and magnetic field diagnostic will be introduced.

3.1 RadioChromic Film

The main detectors of laser accelerated protons are Gafchromic RadioChromic Films (RCF) manufactured by ISPcorp. These are self developing films that are sensitive to ionizing radiation and are mainly used for medical imaging and dosimetric applications. After exposure the films change color and optical density in a specific way [77]. The RCF can be handled under sunlight condition, a darkroom is not required. RCF can be bought with different sensitivities that cover several orders of magnitude of dose detection. The RCFs are flexible and can be easily cut and bent in variable shapes.

Before going into details of the calibration the make-up of the MD-55 RCF is described in following.
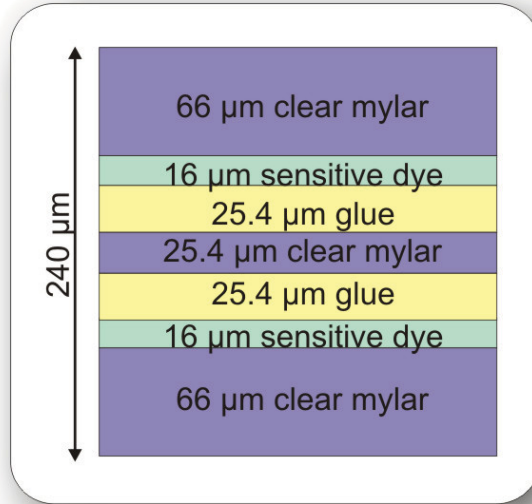
Figure 3.1: Setup of a MD-55 RadioChromic film

The MD-55 film has a typical thickness of 240 μm and consists of several layers as shown in figure 3.1. Between two transparent layers of 66 μm of polyetilen teraphtalat known also as mylar or polyester one finds two 16 μm layers of active dye separated by mylar and glue. For comparison the less sensitive HD-810 film has 7 μm of active dye and a 100 μm supporting mylar layer, HS the most sensitive film type has a dye layer 40 μm in thickness. Both the mylar substrate and the dye have an average density of 1.4 g/cm^3. After irradiation a polymerization process of the active organic dye takes place [77]. As a result the absorption in a spectral range around a peak of 660 nm is

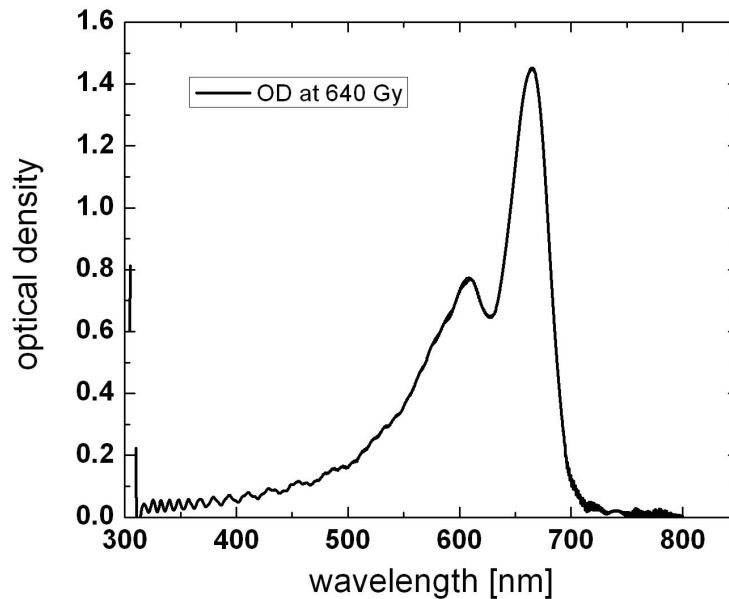increased (see figure 3.2). Three types of RCF MD-55, HD-810 and HS sensitive from

Figure 3.2: Absolute optical density of a HD-810 RCF spectral resolved with a photo-spectrometer

Gy to kGy in dose were used in the experiments and the response of these films was absolutely calibrated using a 8 MeV proton beam. The Tandem accelerator at Max Planck Institut für Kernphysik Heidelberg can deliver proton energies of up to 30 MeV with currents of hundreds of nA. For the calibration a proton energy of 8 MeV was chosen in order to make use of the plateau region of the energy deposition curve of protons in mylar (see figure 3.6). Protons with this energy will pass through the RCF and will deposit during the transit a constant amount of energy in the whole film depth. No higher energies were used in order to minimize activation of the films and therefore increased handling precautions. To get a homogenous irradiation the accelerator beam was enlarged using quadrupole magnets and then sub-apertured with a pinhole leading to an uniform irradiation of the films with a beam of 1 cm in diameter. At the same time the current passing through the RCF was captured and online monitored by a Faraday cup. The films were irradiated with different amounts of proton numbers by changing the current intensity and exposure time.

The films were read out using a Mikrotek ARTIX 1800f commercial flatbed transmission optical scanner. As reported in [78] the dynamic range of the films depends

strongly on the spectral range used for the readout. It can be increased by using a combination of three wavelengths by reading out the red, green and blue channels of the scanned image separately. The RCFs were scanned using the Silverfast AI software of the scanner as 48 bit RGB uncompressed TIFF files turning off any automatic software image enhancements. The postprocessing was done using RSI IDL 6 scripts. A typical scanned calibration wedge can be seen in figure 3.3. Assuming that the beam

Figure 3.3: HD-810 RCF irradiated by 1-10 nC of 8 MeV protons

profile used for irradiation is uniform the film response becomes just a function of the deposited dose (energy/mass) in the films. The energy deposition was calculated using SRIM. For the 8 MeV protons and mylar as a target material SRIM calculates 10 keV/μm/proton. Figure 3.4 and 3.5 shows the complete set of calibration points for all three RCFs. By combining the various RCF types 3 orders of magnitude of detected dose can be covered. By scanning the RCF in color mode one can also extend the detection range of a certain type. While the red channel saturates very quickly the green and blue channel follow later, because of the decreased absorption for these wavelengths. One important issue is that the blank films posses an intrinsic optical density (OD). The OD is for each film type specific (noted as I_0 in fig 3.4, 3.5 and shown in table 3.1) and has to been subtracted for the film calibration. The shown calibration curve is specific for the used scanner. The OD given are not absolute OD but calculated from scanner intensity counts.

I_0	Red	Green	Blue
MD-55	54100	56500	58100
HD-810	65500	65531	65531
HS	52300	55400	53100

Table 3.1: Intrinsic background of the RCFs for each scanned color channel
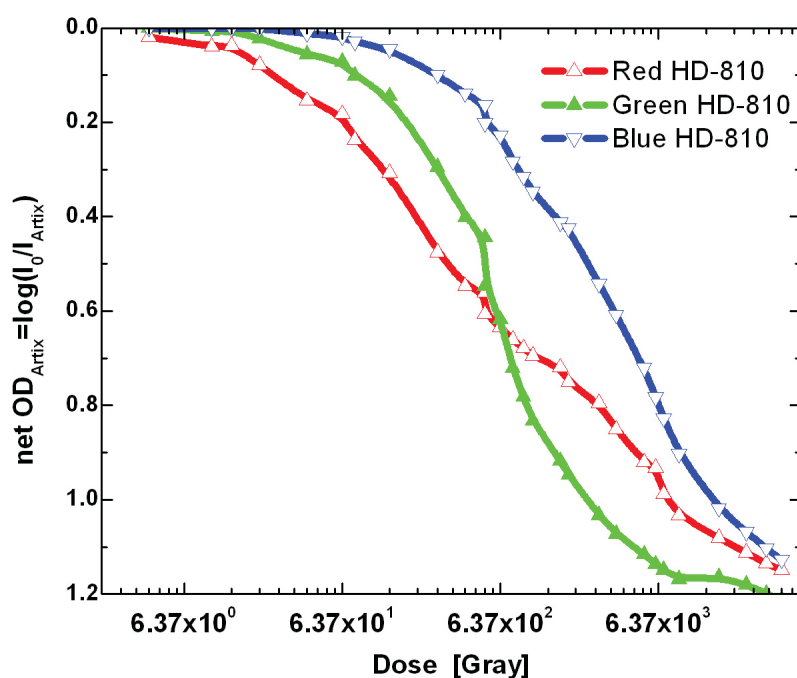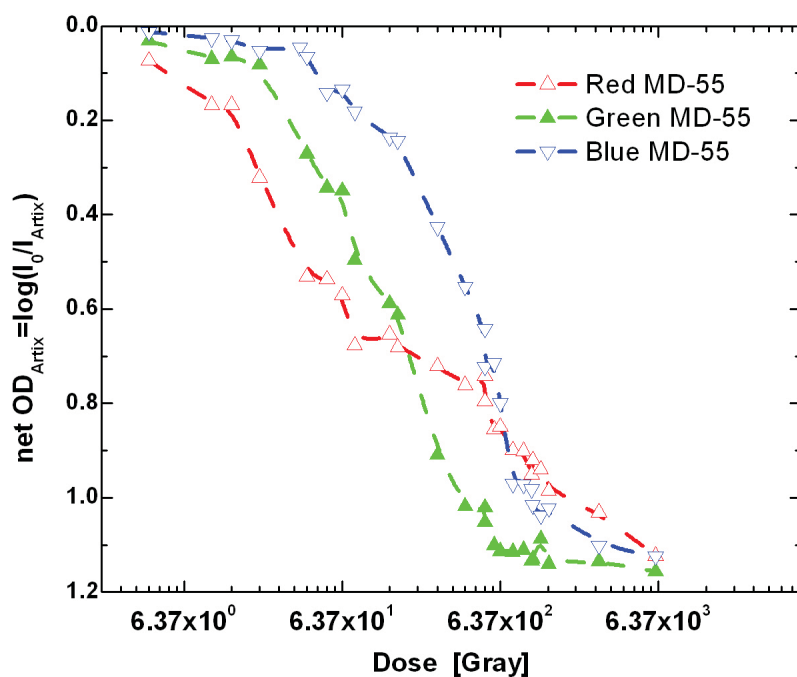
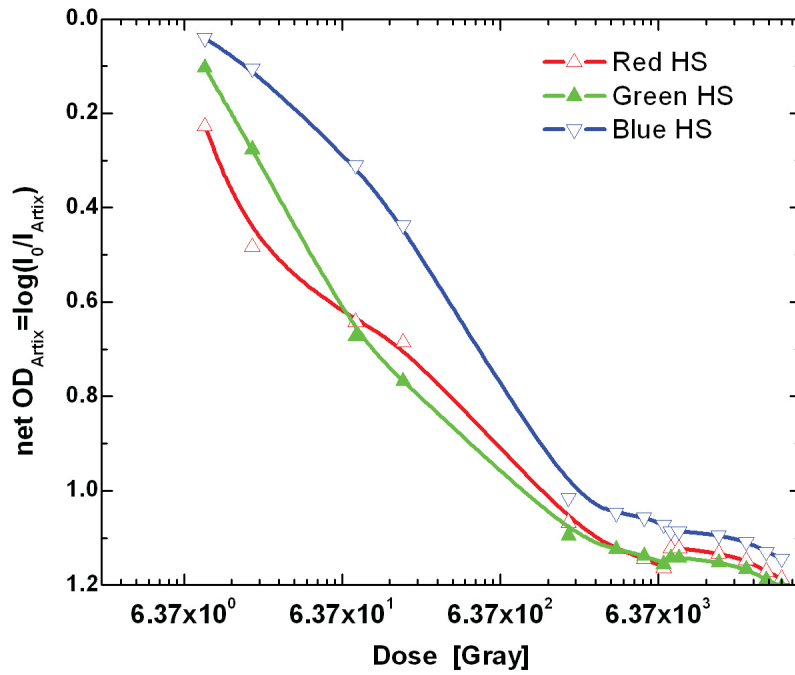Figure 3.4: Calibration curves for a RCF of type Md-55 and HD-810

Figure 3.5: Calibration curves for a RCF of type HS

If the calibration curve is to be used with any other scanner a cross calibration between the two scanners with an optical wedge has to be carried out. Actually the calibration curve gained in this work has been already used by partner groups at LULI laboratory and Queens University Belfast. At this point absolute measurements of proton flux are possible with RCF.

3.2   RCF as an Energy Detector

A stack of RCFs can be used as a coarse energy detector by making use of the energy deposition curve (known as Bragg curve) as a function of penetration depth and incident particle energy. For mylar with a solid density of 1.4 g/cm^3 as a target material the energy deposition curve for protons as calculated with SRIM is given in figure 3.6 A. An aluminium foil 11-15 μ in thickness wrapped around the RCF stack to block any direct laser exposure of the film is also considered, but has only marginal influence (increased stopping power) for the low energy protons. At the end of their trajectory the protons reach the highest energy deposition in the so called Bragg peak. Up to one third of the incident energy can be deposited in this peak. Analyzing the shape and magnitude of the energy deposition curve a normalized curve f_{Bragg} can be found for several energies by normalizing the Bragg curve ordinate to the maximal energy deposition at the Bragg peak and the abscissa to the position of the Bragg peak. The normalized Bragg curve is shown in 3.6 B. Two empiric fit functions can be found describing the energy dependence of the Bragg peak position $x_{Bragg}(E)$ (figure 3.6 C) and energy loss at the Bragg peak $E_{max}(E)$ (figure 3.6 D). Using the normalized Bragg curve the energy loss in the films can be approximated for a incident proton energy E as:

$$-\frac{dE_{dep}}{dx}(E, x) = E_{max}(E) f_{Bragg}\left(\frac{x}{x_{Bragg}(E)}\right), \tag{3.1}$$

with $1 < E < 22$ MeV and x the depth in the film.

A RCF will detect predominantly the one energy reaching the Bragg peak at the position of the sensitive layer. By stacking RCFs the energies reaching the Bragg peak in the sensitive layer will be detected. Because the exponential function of the proton numbers with the energy the dose deposited by the particles transmitted can be neglected. The RCF stacks used in most of the experiments contained 4 HD-810 films and 8 MD-55 films. The HD-810 films have less sensitivity but are thinner and allow better energy resolution at the low part of the spectra detected. The proton energies corresponding to such a RCF stack calculated with the equation 3.1 are 1, 3.1, 4.5, 5.5, 7.35, 9, 10.5, 11.9, 13, 14.2, 15.4 and 16.2 MeV. This aluminium layer in front of the first layer defines a minimal energy being detected as the sensitive part of the HD-810 films is oriented towards the proton beam.

For low flux application such as detection of protons inside a magnetic spectrometer a second detector type was used, the Fuji Image Plate.
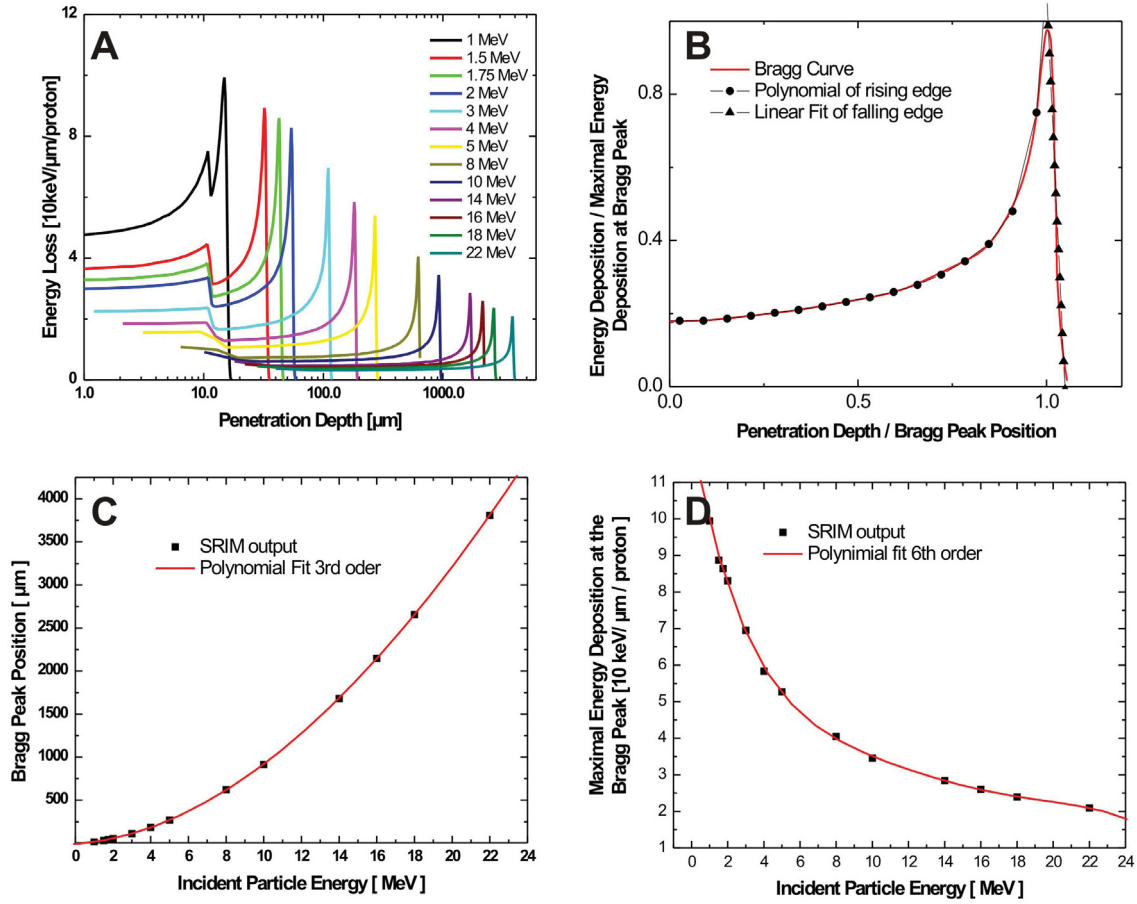
Figure 3.6: A. Energy deposition in function of penetration depth and proton energy. B the self similar normalized Bragg curve. C. Bragg peak position. D the maximal energy deposition (at the peak of Bragg curve)

3.3   Fuji Image Plates

The second proton detector used in this work was an Image Plate (IP), a photostimulable phosphor plate that can be used to record a two-dimensional image produced by a short-wavelength (typically X-ray) electromagnetic radiation. The IPs are currently used in medical imaging applications and are a substitute for classic X-ray films. They are very interesting because of the much lower irradiation dose needed for exposing an image. Unlike conventional X-ray films, an IP can be reused. In combination with a dedicated scanner a dynamic range of 5 orders of magnitude can be reached.

The process on which the IP relays on is known as Photostimulable Luminescence

(PSL). The IP is a flexible image sensor in which arrays of very small crystals (grain size: about 5 μm) of photo-stimulable phosphor of barium fluorobromide containing a trace of bivalent europium as a luminescence center, formulated as BaFBr: Eu2+ are uniformly coated on a polyester support film. The sensitive layer of the Imaging Plate of type BAS TR used in this work was 50 μm thick [79].

After exposure the IP was scanned with a FUJI BAS 1800 II commercial scanner. The IP is scanned with with a resolution of 50 μm per pixel by a focused laser beam and the PSL released is collected by a photomultiplier and digitized. The exposed IP is reusable after erasing the residual latent image with uniformly irradiated visible light, therefore daylight protection handling precautions have to be considered. The data saved by the scanner has a logarithmic format, the unit being called PSL. More details can be found in the scanner manual.

For measuring an absolute flux of protons a calibration curve is required. While the response curve for electrons is known ([80, 79]) no calibration for protons was found in the literature. During the RCF calibration run at MPIK Heidelberg also IPs were irradiated. While the RCF could be placed directly in the accelerator beam this method was inappropriate for irradiating IP because of lower saturation flux of these films. The accelerator was set already for the RCF calibration in minimal current and exposure settings. For decreasing the proton flux measurements employing a scattering geometry was used. While transmitted through a thin solid foil a fraction of the protons are scattered changing the propagation direction. The Rutherford scattering cross section describes this process [81]. For the 8 MeV proton beam used in Heidelberg and a target aluminium foil 10 μm in thickness a scattering efficiency of 10^{-7} for a scattering angle of 18 deg can be calculated. This decrease in flux was enough in order not to saturate the signal on the films. While analyzing the data it turned out that the IP was not irradiated only by protons but also by the X-ray produced during the scattering process of the protons. The X-ray produced such a strong background that the energy deposited directly by protons could not be discriminated. Even a second calibration run with better shielding of the films was not successful.

At this point the calibration strategy was changed. A cross calibration of the IP with a RCF was done. For this calibration a proton beam was generated in the conditions described in chapter 5.10. This poly-energetic diverging beam was detected by a stack of RCFs positioned a few cm after the source. A hole was drilled in the center of the RCFs, the transmitted proton beam was detected with a magnetic spectrometer. The

entrance slit of the magnetic spectrometer was placed 1 m after the source. At this distance the proton beam reached the optimal flux for the detection with the IP. The spectral energy distribution of the proton beam can be measured at the same time at discrete energies with the RCF stack and continuously with the magnetic spectrometer. From the absolute calibrated RC film a cross calibration of the IP was done by taking into account the beam solid angle detected by the spectrometer, the spectrometer slit size, and IP scanner pixel size. An incident proton energy dependent calibration factor has been found and is shown in figure 3.7. This curve is however valid just for the
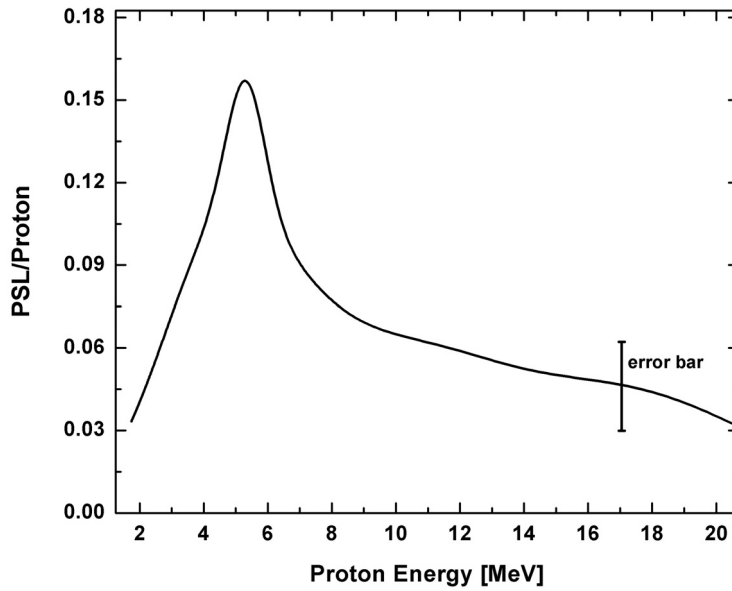

Figure 3.7: Calibration curve in function of the energy for the IP BAS TR. The curve was determined by cross calibration with a RCF.

magnetic spectrometer used during this work. This is because of the incidence angle of different proton energies on to the IP is specific for each spectrometer. Protons of different energies are stopped by different IP sensitive layer thicknesses. The curve can be understood as an energy deposition curve where protons with energies less than 5.2 MeV are stopped in the sensitive layer while the ones with higher energies are transmitted. The BAS TR IP was also checked to be linear for at least 3 orders of magnitude by varying the exposure.

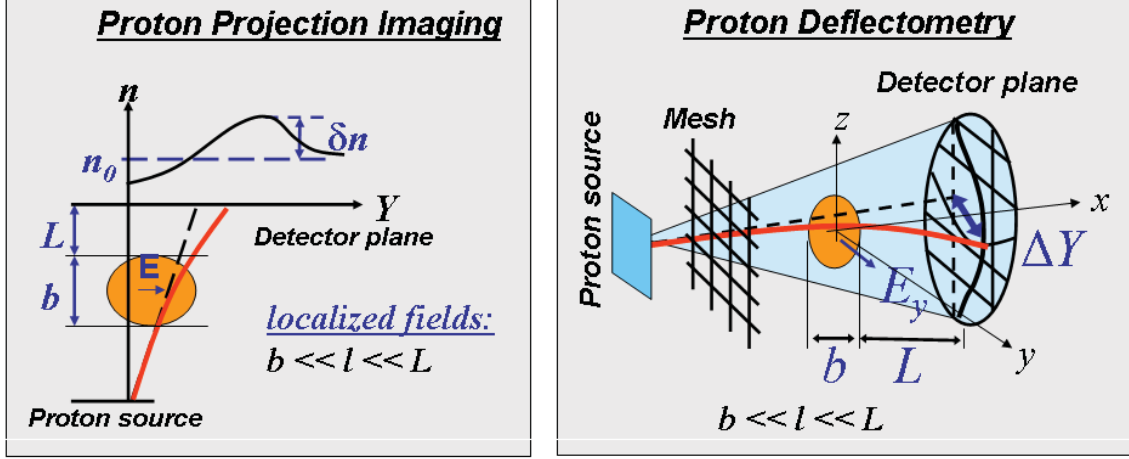# 3.4 Proton Imaging as a transient Plasma Field Diagnostic

Figure 3.8: Setup of Proton Imaging and Proton Deflectometry. Proton Deflectomety measures directly the proton deflection yielding the electric field map. Proton Imaging is sensitive to the field gradients yielding the charge density map

Proton probing techniques exploit the fact that the proton source, while being physically extended, is highly laminar and hence equivalent to a virtual point source. In Proton Imaging a point projection of the probed region is obtained [82, 83] with a spatial resolution set by the virtual source size, which is typically of the order of a few μm, and a magnification given by $M = (L + l)/l$, where L is the distance between interaction volume and detector and l is the distance between proton source and interaction volume. This technique is mainly sensitive to field gradients, which are detected via proton density modulations in the probe beam cross section. In Proton Deflectometry [83] a mesh is additionally inserted between the proton target and the interaction target in order to pre-imprint a periodical pattern on the proton beam cross section. Proton deflections can be measured from the mesh imprint deformation, providing a direct measurement of the fields. The deflection of a proton by an electric field E constant in time can be expressed as:

$$\delta = \frac{\Delta mv}{mv} = \frac{\int eEdt}{mv} = \frac{eE}{mv}\frac{b}{v}, \tag{3.2}$$

where mv is the momentum of the proton, Δmv is the acquired momentum in the E-field, b is the length of the interaction.

Equation 3.2 becomes for the Proton Deflectometry setup shown in figure 3.8:

$$\Delta Y \approx \frac{eL}{mv^2} \int_{b/2}^{b/2} E_y(x,Y)dx. \tag{3.3}$$

The electric field integrated over the probed volume can be further deconvolved using techniques such as the inverse Abel transformation to extract the local electric field in the probed volume [84].

When the proton beam is detected with an RCF stack the individual layers will measure snapshots of the field distribution at different times. This is due to the different times of flight of the protons detected by each layer to the interaction volume. By changing the probing geometry also continuous time resolved measurements are possible as proposed and demonstrated in chapter 5.12.1.

3.5   Optical Shadowgraphy and Schlieren Imaging

Optical Shadowgraphy and Schlieren Imaging are established qualitative plasma diagnostics. They are used to visualize the plasma density variation and the associated refractive index gradients. In Schlieren Imaging, the collimated light passing the probed plasma is focused with a lens, and a knife-edge is placed at the focal point, positioned to block about half the light. In plasma of uniform density this will simply make the image on the detector half as bright. However in a plasma with density variations the beam is distorted and focuses imperfectly, and part the of the beam which was focussed in an area covered by the knife-edge is blocked. The result is a set of lighter and darker patches corresponding to positive and negative density gradients in the direction normal to the knife-edge. When a knife-edge is used, the system is generally referred to as a Schlieren Imaging system, which measures the first derivative of density in the direction of the knife-edge. If a knife-edge is not used, the system is generally referred to as a Shadowgraphic System, which measures the second derivative of density [85].

3.6   Magnetic Spectrometer

Image plates of type BAS TR were used for the detection of MeV protons in a magnetic spectrometer. The magnetic spectrometer used during this work has been already used in [47] for proton detection. It consists of a 15 cm long 0.5 T magnet and can be used for the detection of protons with energies higher then 2 MeV. The spectral resolution determined by the slit width and the dispersion of the spectrometer is 0.2 MeV at 6 MeV and 0.7 MeV at 15 MeV. A slit width of 250 μm was used. The energy calibration of the spectrometer was done by filtering the proton beam with aluminium of different thickness to create a defined minimum detected energy cut off.
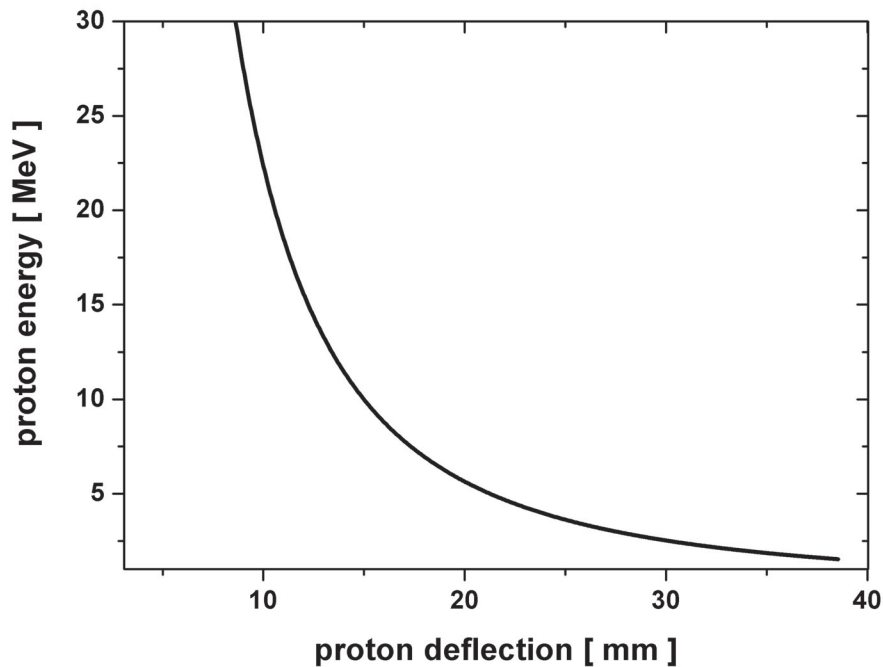

Figure 3.9: Calibration curve of the magnetic spectrometer used. The proton deflection as a function of the energy is shown.

Chapter 4

Experimental Setup

For the experimental part of this thesis two laser systems have been used. The lasers and experimental setups employed for creating the laser matter interaction are similar. Still the uniqueness and advantages of each system and experiment will be presented in the next sections. It has to be stated that all the experimental data used in these thesis was collected during experimental runs at the 100 TW laser at the Laboratoire pour l'Utilisation des Lasers Intenses (LULI) at the Ecole Polytechnique Palaiseau in France and at the Vulcan Target Area West at the Rutherford Appleton Laboratory Didcot, United Kingdom. The access to this facilities was supported by the EU LASERLAB ACCESS program.

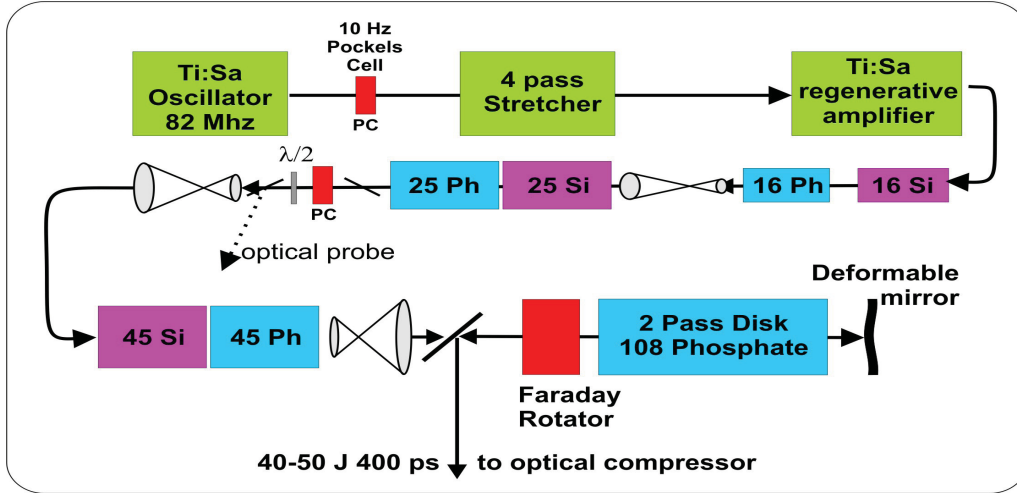# 4.1 Laser Systems

4.1.1 The 100 TW LULI Laser System

Figure 4.1: Setup of the 100 TW laser system. The main amplifiers consist out of neodymium silicate (magenta) and phosphate (blue) doped glass rods 16, 25 and 45 mm in diameter pumped optically by flash lamps. In between the amplifiers the beam is the magnified by telescopes. The last amplifier is a double pass glass disk 108 mm in diameter.

Figure 4.1 shows a simplified sketch of the Nd:glass LULI laser system delivering pulses to the 100 TW experimental laboratory. The laser is operated at a wavelength of 1.054 μm. A Ti:Sa active mode locked oscillator generates laser pulses of 100 fs in duration and 1 nJ in energy. As necessary for the CPA scheme [1] the pulses are stretched with an Oeffner Type Stretcher to around 1.3 ns. This pulse is seeded into a Ti:Sa regenerative amplifier pumped by a 20 mJ, 10 Hz doubled YAG laser at 532 nm. The energy at this point reaches 1 mJ in a pulse length of about 700 ps. The shorter pulse length is gained at cost of the amplified bandwidth, thus recompression to the original 100 fs is not possible anymore due to gain narrowing. The further amplification of pulse is done by using single pass neodymium silicate and phosphate glass rod amplifiers of increasing diameters 16 mm, 25 mm and 45 mm and telescopes for beam size readjustments. The glass rods are pumped using flash lamps. The last amplification stage is done with a 108 mm double pass neodymium glass disk amplifier.

The double pass is realized by using a polarization dependent mirror and a Faraday rotator. This mirror is a dynamic adjustable deformable mirror. This mirror is used to correct static phase aberration due to different optics in the beam path and also dynamic aberration created by the thermal load of the glass rods and disk after the discharge of the flash lamps. The maximal repetition rate at full energy is 1 pulse every 20 min although active nitrogen gas cooling of the glass amplifier is employed. At this repetition rate the use of the deformable mirror for phase correction is mandatory. 80 J can be reached in a beam 8 cm in diameter and 400 ps long pulse before recompression. Two beams are created using a beam splitter and each beam is transmitted with a separated beam line into an independent optical compressor. One compressor is placed in vacuum allowing 20 J to be compressed and one in air allowing 10 J of energy to be compressed to 350 fs FWHM short pulses. Due to the nonlinear refractive index of air with increased intensity (also known as B-integral) leading to the loss of phase coherence no higher energy could be used with the air compressor while the energy limitation of the vacuum was the damage threshold of the gold coated compressor gratings. After focusing with an f/5 off axis parabola the vacuum beam reaches an intensity of 5×10^{19} W/cm^2 while the air compressed beam reaches 3×10^{18} W/cm^2. The one order of magnitude found in the focal spot intensities are the result of the pulse energy difference and due to the different focal spot qualities, the air compressed beam having a poor phase wavefront distribution. The contrast of the laser measured with diodes and a 3-rd order autocorrelator is 10^{-7} from ns to 20 ps before the main pulse. After the 25 mm rod amplifier a fraction of the beam can be split using a half wave plate and a polarization dependent mirror. This beam is recompressed in air and is normally used as a synchronized mJ level optical probe beam.

The advantage of this laser system is the flexibility it has due to the use of the two independent compressors. While keeping one beam as a constant probe beam scaling experiments can be done while easily changing the pulse duration of the pump. Also the splitting ratio of the energy can be varied.

4.1.2 The Vulcan Laser System

Vulcan is a large scale Nd:glass laser system capable of delivering several synchronized laser pulses covering a whole range of energy and pulse length. Three areas are at the disposal of the experimentalists. The newest one the PW area is delivered by a 500 fs and 500 J laser pulse [86, 87]. The older experimental areas where designed to have

up to 8 synchronized high energies pulses. While the Target Area East uses 80 ps to 2 ns pulses in duration in the Target Area West two of the 8 beams can be optically compressed to 1.2 ps. One of the two beams reaches 100 TW level containing up to 100 J the other one is used as an low energy optical probe beam. The LULI 100 TW laser has emerged from the VULCAN laser design, so parts of the LULI laser can be found in the VULCAN laser setup as seen in figure 4.2. During this thesis the CPA beam called beam 8 delivering the Target Area West was used. The pulses are created by a saturable absorber mirror (SAM) oscillator. Before fed into the VULCAN main amplification chain, the oscillator pulses are stretched from 170 fs to a duration of several hundreds of ps and pre-amplified using 9 mm rod amplifiers from nJ to sub-100 μJ energy level. The beam is now cut and spatially split in two beam, one half of the beam has a longer path hence being optically delayed compared to the second. The two beams are then rejoined and follow a parallel path with some spatial separation through the remaining amplification stages. As in the LULI 100 TW laser the pulse is amplified with 16 mm, 25 mm, 45 mm rods single pass and a 108 mm double pass disk amplifiers in combination with a Faraday rotator. At the end of the double pass a deformable mirror is employed for the correction of static aberration.
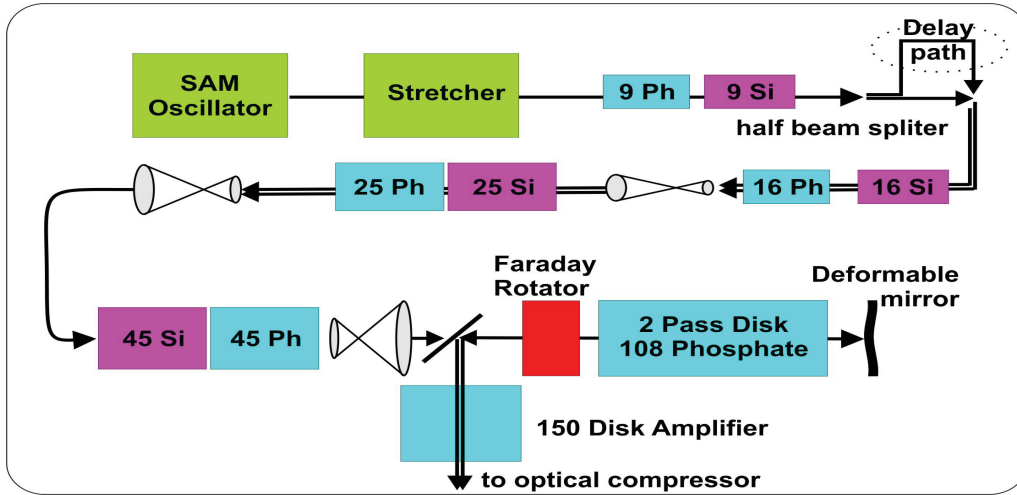

Figure 4.2: Setup of the RAL VULCAN laser system. Specific for this laser is that the oscillator beam is preamplified in a 9 mm glass rod amplifier and then split in two halves, that can be optical delayed to each other. The beam is then amplified by glass amplifiers 16, 25, 45, 108 and 150 mm in diameter.

Compared to the LULI 100 TW laser the VULCAN pulse is amplified further by

a 150 mm single pass glass disk amplifier to 100 J level. Vacuum spatial filters are used to expand and clean the beam between each amplification stage. The pulse compression to 1.2 ps is done by using a double pass optical compressor, where just the last grating is placed under vacuum. The two halves of beam 8 are simultaneously compressed therefore not allowing independent pulse length settings. The advantage of the VULCAN laser over the LULI laser is the higher pulse energy and the smaller focal spot compared to the beam compressed in air used at LULI. The contrast level was measured during the experiment to be 1×10^{-6} in intensity at 8 ns before the main pulse. With this pre-pulse contrast the laser had to be used at half nominal pulse energy and proton production was impossible with targets with less than 20 μm in thickness that limited the maximal accelerated proton energies to 14 MeV.

4.2   Experimental Setup

After introducing the two laser systems used during this work the experimental setup specific for each experiment will be described in the next sections.

4.2.1   Setup at LULI

The laser beam setup in the experimental chamber of the 100 TW LULI laboratory is shown in figure 4.3. The two high energy laser pulses CPA1 and CPA2 are entering the chamber from opposed ports. Each beam is reflected with a turning mirror and then focused by an off axis parabolic mirror. The two parabolas with 40 cm focal length and f/5 allowed reaching intensities of $I = 5 \times 10^{19}$ W/cm^2 for the CPA1 laser and $I = 3 \times 10^{18}$ W/cm^2 for CPA2. The CPA1 laser pulse duration was set in optimum compression mode at 350 fs FWHM while the laser pulse duration of CPA2 was varied between 350 fs and 1.2 ps. The path of the CPA2 was variable in length, the optical delay introduced being controlled with ps resolution. The incidence angle of the CPA2 compared to CPA1 is 105 deg. The optical synchronization between CPA1 and CPA2 was done by first spatially overlapping the two focal spots on an angled thin glass slab. The angle was set in such way that the transmitted and reflected beam overlap spatially. The focal spot was then imaged on the entrance slit of a streak camera or an optical spectrograph. First a rough optical synchronization from ns to 100 ps level was done with the help of the streak camera. In the absence of a faster sweeping time of the streak camera the ps synchronization was done by minimizing the interference pattern
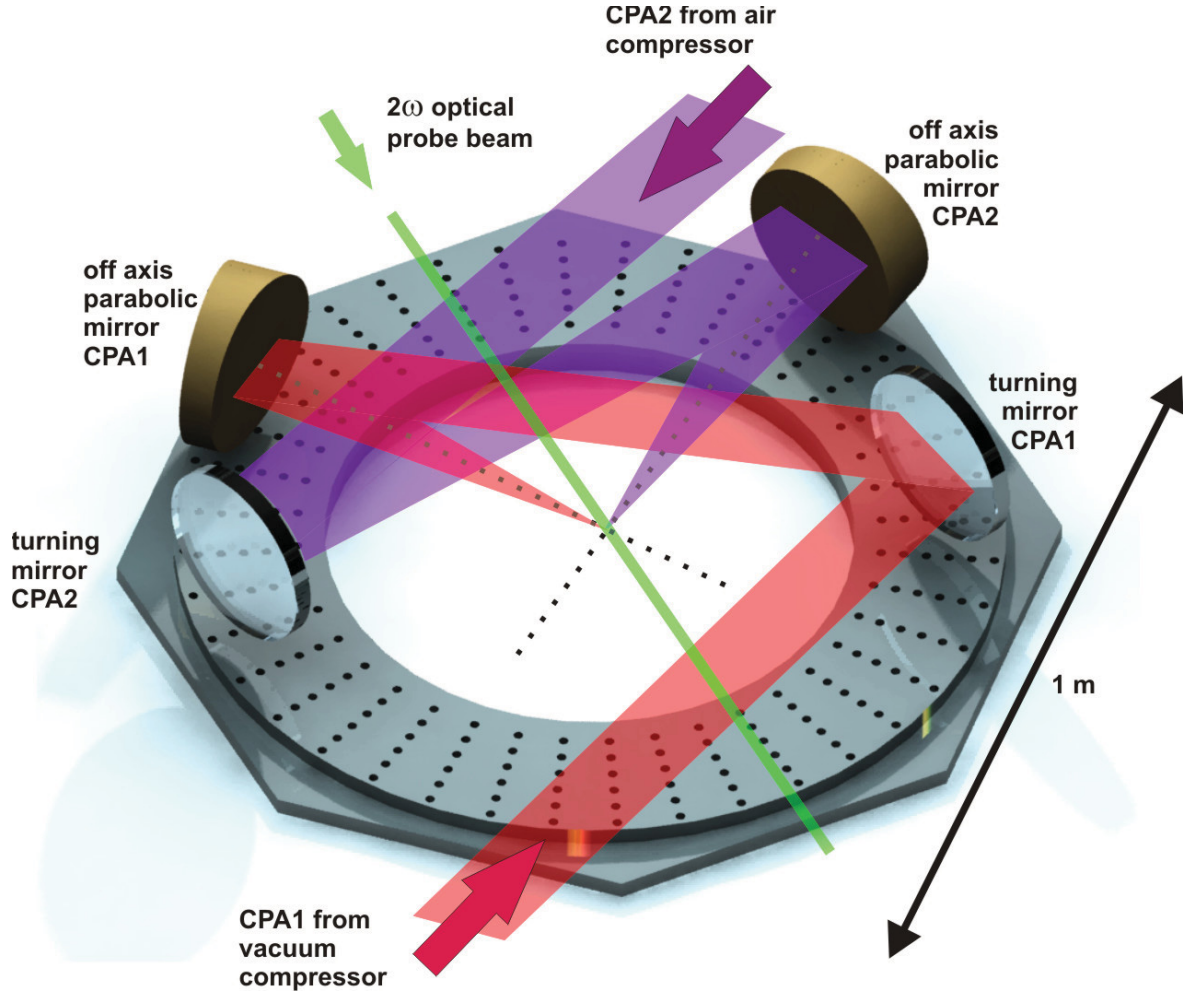
Figure 4.3: Beam setup of the LULI 100 TW experimental chamber.

in the laser spectra seen by an optical spectrograph. While the two laser pulses travel in the spectrograph they are stretched in time. If the pulses overlap in time to some degree the spectrum of each pulse will interfere due to the time and consequent phase mismatch. Then the optical delay is changed in such a way that the wavelength of beat pattern of the interference seen is maximized. If the two pulses overlap perfectly in time no phase difference exists and the intensities of the two spectra will add without any interference term. After doing this synchronization the laser focal spots were separated by several mm specific to each experiment done. The CPA1 laser was used for the acceleration of a MeV proton beam used during the experiments as a probe. The pump beam was the CPA2 laser which created the plasma to be studied. The

proton beam was detected with a stack of Radio Chromic Films or in some cases with a magnetic spectrometer. While the RCFs were placed at variable distances from the proton source, the entrance slit of the magnetic spectrometer was fixed at 70 cm from the source.

For some experiments the third beam delivered by the 100 TW laser a low energy laser pulse was employed as an optical probe beam (green beam in figure 4.3). This collimated beam was injected into the target chamber at 45 deg compared to the CPA1 focal axis. The laser pulse was converted to 2ω with the help of a SHG crystal. The interaction volume to be probed was then magnified and relayed for detection outside the target chamber using a 4 f relay imaging setup, the detection being done with an ANDOR 16 bit CCD camera. Before the camera 2ω spectral filters were used to filter out direct scattered laser light and plasma fluorescence from the probe 2ω light. A second delay line allows for independent synchronization of the optical probe with CPA1 or CPA2. The vacuum pressure in normal operation of the target chamber was in the order of 10^{-4} mbar.

The mount of the target holder consisted of two sections. The interaction targets are mounted on an exchangeable holder. This holder can be fixed with a magnetic base inside the target chamber on a stage driven by steping motors (3 translations and 1 rotation). The targets were positioned inside the interaction chamber with the help of long range microscopes. The pre-alignment of the targets was done in air. Three microscopes observing the targets from perpendicular directions allowed for the positioning with $\sim 10~\mu$m accuracy.

4.2.2 Setup at Vulcan Target Area West

The experimental setup inside the target chamber used at Target Area West at the Rutherford Appleton Laboratory is sketched in figure 4.4. The two laser beams delivered by the beam 8 of VULCAN are compressed by a single optical compressor to 1.2 ps. These beams enter the target chamber separated in height by a few cm. While the CPA2 beam is directed onto a off axis parabolic mirror a half mirror is used to separate the path of the CPA1 beam. After being reflected by this turning mirror the CPA1 beam is also focused by an off axis parabolic mirror with 60 cm focal length. Both CPA1 and CPA2 reached a focused intensity of $5 - 9 \times 10^{18}$ W/cm^2. The focal spot size created by the f/3.2 parabolas was checked under low energy conditions with a CCD camera to be 11 μm FWHM. The CPA1 laser was used for the acceleration of

a MeV proton beam used in the experiments as a probe. The CPA2 laser pulse created the plasma to be studied.
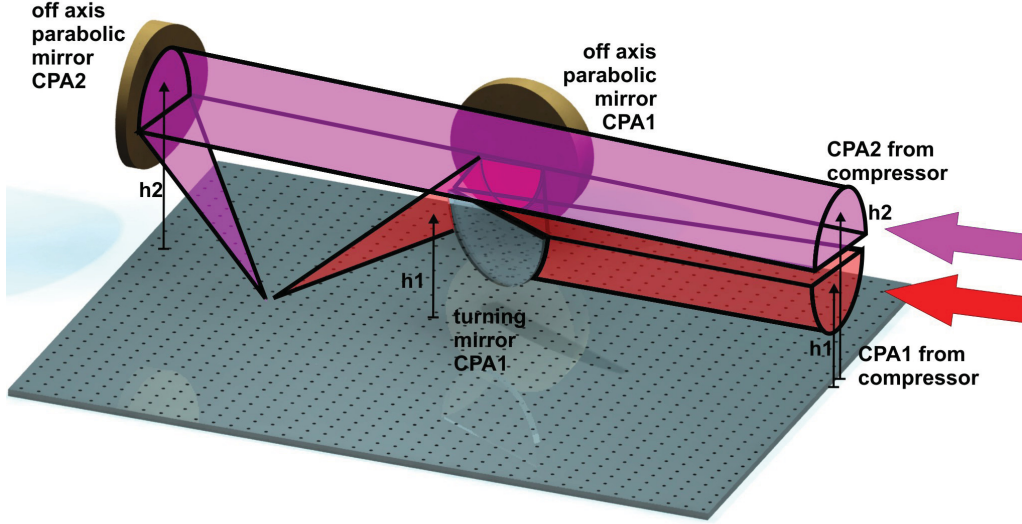

Figure 4.4: Beam setup at the RAL TAW experimental chamber. The two CPA beams exit the compressor in different heights. While the CPA2 beam is directed onto a off axis parabolic mirror a half mirror is used to separate the path of the CPA1 beam before focusing.

The synchronization of the two beams was done in a similar way as described above employing this time just a FESCA HAMAMATSU high speed streak camera with 500 fs resolution as a detector. The proton beam was detected with a stack of Radio Chromic Films or in some cases with a magnetic spectrometer. While the RCF were placed at variable distances from the proton source, the entrance slit of the magnetic spectrometer was fixed at 120 cm from the source. The vacuum condition in normal operation of the target chamber was in the order of 5×10^{-5} mbar.

As in the LULI 100TW experiments the interaction targets were also pre-aligned in air and placed inside the vacuum chamber on an exchangeable target mount connected to a magnetic base with 2D translation and one rotation motorized stages. Because of motorization with DC linear motors the absolute translation was measured using SONY MAGNESCALE probes.
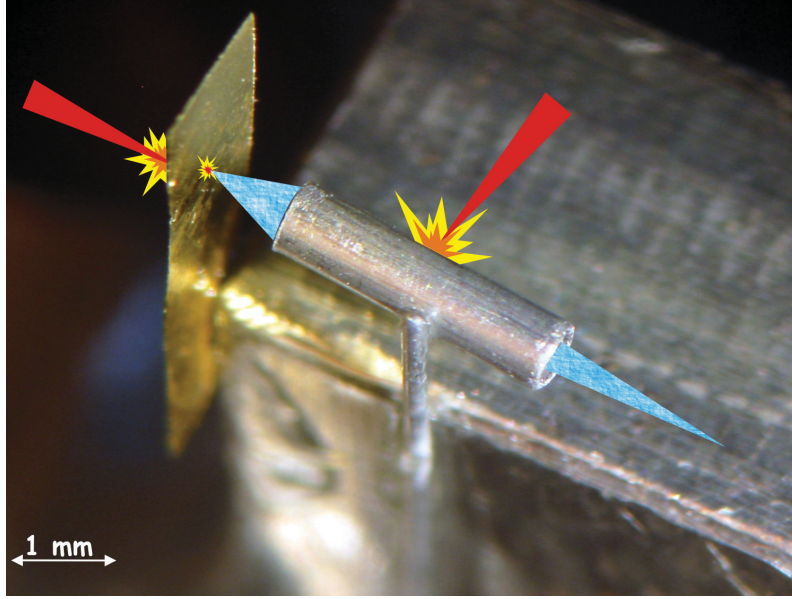
Figure 4.5: Typical interaction target setup. The gold foil is used to accelerate an MeV proton beam. The laser triggered micro-lens is created inside a hollow cylinder irradiated by a relativistic intensity laser pulse. The cylinder diameter was varied between .5 and 1.5 mm and the length from .3 to 3 mm.

Figure 4.5 shows an exemplary photographic image of the interaction target used during this thesis. The CPA1 laser accelerates a MeV proton beam from a metallic foil 10 - 20 μm in thickness. A hollow cylinder is irradiated by the CPA2 laser pulse and the laser triggered micro-lens is created inside the cylinder. Both the acceleration foil and the hollow cylinder target can be easily produced, the bulk materials are commercially available and can be bought from Goodfellow GmbH Friedberg. Still a cutting machine had to be developed during this work for producing the needed cylinder lengths from the 10 cm tubes delivered. More details to the targets geometry are given in the next chapter being specific for each experiment done.

Chapter 5

Experimental and Computational Results

Laser-driven acceleration of protons is a revolutionary technique which has opened new perspectives for major applications in scientific, technological and medical areas. By simply directing a high-power ultra-short laser pulse onto a thin solid foil, it is now possible to produce beams of high-energy protons, having velocities up to one third of the speed of light, and characteristics so far only achieved employing conventional large-scale accelerators. The proposed applications of these beams include energy production via thermonuclear fusion, cancer therapy and production of radioactive particles for medical diagnosis. However, progress in these areas is conditional to addressing some of the present limitations of laser-accelerated beams. A particular concern is that the beams diverge quickly (e.g. they are difficult to transport over significant distances) and contain protons having many different velocities.

In this thesis a new approach is reported on how to overcome these problems. The technique employs electric fields generated for a very short time within a micro-cylinder irradiated by a short, intense laser pulse. These fields can focus efficiently a proton beam directed along the axis of the cylinder. An important point is that only protons reaching the cylinder while the fields are active (i.e. only protons having a specific velocity) will be focused. By discarding the unfocused part of the beam, it is therefore possible to select only protons having the same velocity, with major implications for all the applications mentioned above. Following each experiment PIC simulations done with the PSC code (kindly provided by Hartmut Ruhl) are shown and compared with the experiment. These simulations show if and how fields are build up inside a laser

irradiated cylinder and how this fields will evolve. The first sections of this chapter will concentrate on the laser triggered micro-lens capability to focus and energy select MeV protons. The later sections report of experiments elucidating how the lens is generated. With the help of simulations an upscaling of the lens capabilities for focusing higher energy proton beams as required by several applications will be done. This chapter will present also computational results done by external collaborators leading to the understanding of some aspects of the physics behind the micro-lens.

5.1 Initial experiments

The next section gives a brief overview of the electromagnetic field measurements that lead to the development of the laser triggered micro-lens. The experiments were carried out at the LULI Laboratory, employing the 100 TW laser operating in the *Chirped Pulse Amplification* mode (CPA). After amplification, the laser pulse was split into two separate pulses which were then recompressed in separate grating compressors. This allowed the use of two pulses (CPA1 and CPA2) of 350 fs and 350 fs to 1.2 ps duration. The delay between the two CPA pulses was controlled optically with picosecond precision. The CPA1 pulse (irradiance I= 5×10^{19} W/cm^2) was used to accelerate a high-current, diverging beam of up to 15 MeV protons from a 10 μm thick Au foil target (the protons are produced from hydrocarbon impurities on the target surface). The CPA2 pulse (I = 3×10^{18} W/cm^2) was focused onto foil targets of various geometries. The proton beam from the first foil was detected with a stack of RadioChromic Films positioned at a variable distance from the proton source.
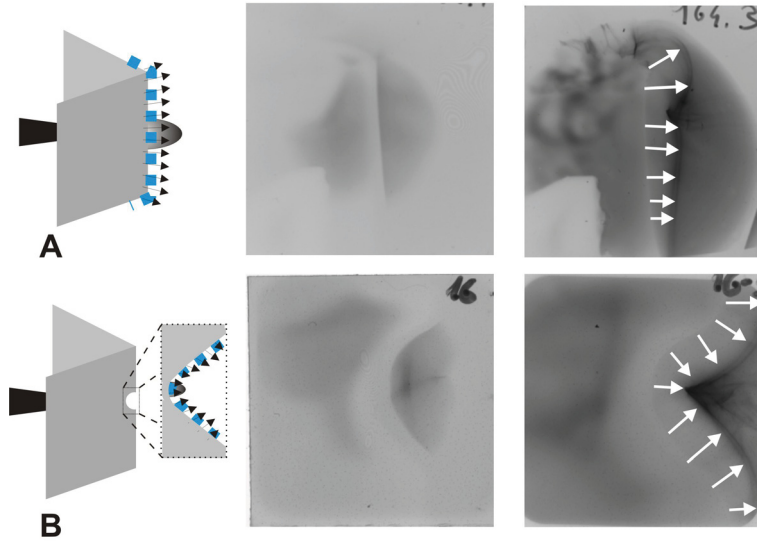

Figure 5.1: Proton probing experiments leading to the development of the laser triggered micro-lens. Left) radiographs of the targets are shown. Right) Proton probe beam is deflected. Large extension fields limit the measurement close to the target surface. A) Proton probing of TNSA fields from a V-shaped target. B) Probing of fields from a dented target.

Proton imaging was used as an electric and magnetic field diagnostic, the exact setup is being described in [55]. In Romagnani et al. the point of interest is measuring directly the fields responsible for ion and proton acceleration. It is shown that beside the ion accelerating fields one finds fields that develop over the whole target surface and exist for some tens of ps. Figure 5.1 has been measured in the same experiment as reported by Romagnani et al. It has a lower magnification, thus the V-shape of the target can be clearly seen (figure 5.1 top). A strong proton deflection normal to the target surface is observed. This deflection is not localized just close to the interaction point, the whole target surface deflects protons away. Proton deflectometry measurements show that these large extension fields reach strengths of 10^7-10^8 V/m [84]. These fields cause a serious problem if one desires to probe an interaction close to the target surface. The probe protons will be deflected to early and will not pass trough the interaction volume of interest.

The goal of a second experiment performed also at LULI, in similar conditions as the one reported above, was probing the proton flow from curved targets, and specially probing the proton focusing properties of such targets. Patel et al. [12] have demonstrated that a focused proton beam is obtained by irradiating hemispheric targets. Because these hemispherical targets do not allow a clear field of view, V-shaped targets with a dent were employed. Again large extension fields deflecting the protons away from the target surface and not allowing measurements close to the targets surface were observed.

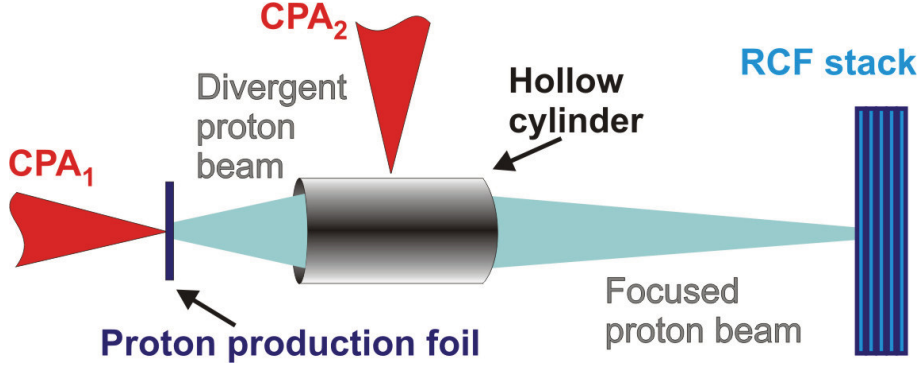## 5.2   Beam focusing with the micro-lens setup

Figure 5.2: Experimental setup of the laser triggered micro-lens

After observing large extension fields deflecting protons away from targets irradiated by a high-intensity short-pulse laser it was proposed to try to exploit these fields to focus a proton beam. Using the experimental setup presented in figure 5.2 focusing of MeV protons has been successfully demonstrated. The experimental data was gathered in a similar condition as in the previous section. The proton beam from the first foil was directed through the cylinder and detected with a stack of RadioChromic Films positioned at 2 cm distance from the proton source. The RCF stack was used to measure the proton beam collimation. It was shielded with an 11 μm Al foil allowing protons with energies above 1.5 MeV to be recorded. In addition, the distance between the proton production foil and the cylinder and the distance between the cylinder and detector were changed. At a source-cylinder distance of 1 mm the proton flux increase due to focusing by the micro-lens was so strong that saturation and thermal load damage of the film occurred. Quantitative data could only be obtained when the cylinder was moved 4 mm away from the proton foil, in order to collect just 1/4 of the diverging proton beam.

Figure 5.3 shows different layers (5 and 6 in the stack) of an RCF pack recording the proton beam after its propagation through a laser-illuminated Dural (a 95% Al, 4% Cu, 1% Mg alloy) cylinder 3 mm in length, 700 μm in diameter and 50 μm in wall thickness that was placed 4 mm from the proton producing foil. In this case, the total distance from the proton-producing foil to the laser pulse incident on the cylinder was 5 mm. The proton energies reaching the Bragg peak in the layers are shown in figure
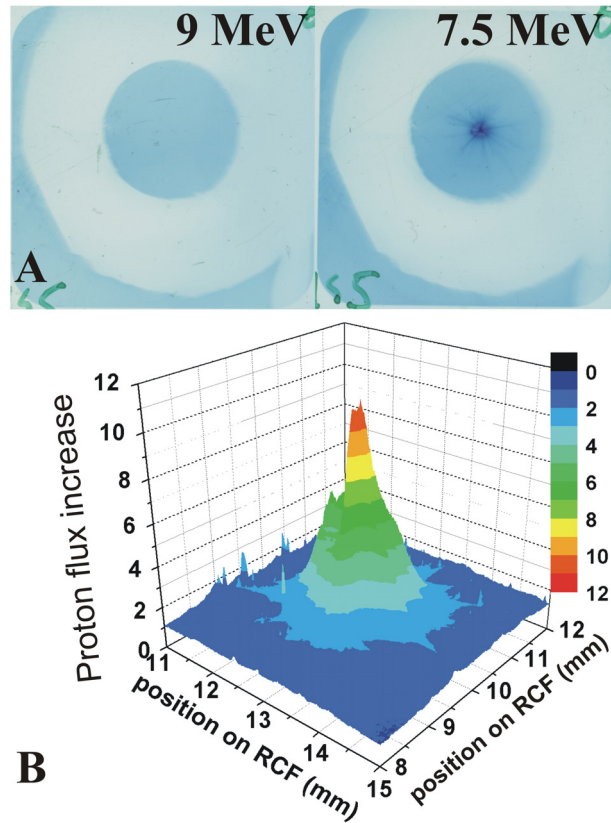
Figure 5.3: A. Beam focusing is observed for 7.4 MeV protons while the 9 MeV have exited the lens before the fields were present. B. The flux increase is given.

5.3A. As expected, no focusing effect is observed for the 9 MeV protons as they enter the cylinder at -61 ps relative to the peak of the CPA2 pulse. Indeed, as the transit time for these protons through the cylinder is 72 ps, the electric field is just triggered by the laser pulse when these protons exit the cylinder. For the 7.5 MeV protons that enter the cylinder at -52 (their transit time is 79 ps) the electric field has developed while these protons are still within the cylinder and a small spot with about 600 μm (FWHM) in diameter is seen at the centre of the cylinder. The flux increase at the film plane is up to 12 times (Fig. 5.3B). The total current for the focused part of the protons with the focusing field to be active for about 10 ps (corresponding to a focused energy range of about 1 MeV) can be estimated as follows: From a typical energy spectrum distribution measurement one finds $\simeq 2 \times 10^{10}$ protons/MeV/srad for an energy range of 6-7 MeV. The total focused current is:

$$I = \frac{2 \times 10^{10} \textbf{ protons/MeV/srad}}{10 \textbf{ ps}} \times \frac{\pi(350 \ \mu\textbf{m})^2}{4 \textbf{ mm}^2} \textbf{ srad} \times 1.6 \times 10^{-19} \textbf{ C/proton} \simeq 7 \textbf{ A}.$$

Under different conditions a 200 μm FWHM spot was measured. No focusing effect is observed in figure 5.4 for the 7.6 MeV protons as the transit time (to the exit of the cylinder) was -5 ps relative to the peak of the CPA2 pulse (incident on the left of the cylinder) and hence no electric field had yet developed inside the cylinder. For the 6.25 MeV protons (transit time +14 ps) a small spot with about 200 μm (FWHM) in diameter is seen at the center of the cylinders shadow. In this case the flux increase at the film plane is up to 15 times as can be seen in figure 5.4. The spot seen in the layer 3 (Bragg peak corresponding to $\sim$ 5.0 MeV) is caused by focused protons with energies higher than 5 MeV, which reach their Bragg peak later in the film pack, but due to the local flux increase, release a significant amount of dose in this layer. The background level seen inside the cylinder is generated by the unfocused higher energy protons. The annular proton pileup outside the cylinder can be explained by an E-field of opposite sign as on the inside. The electric field points away from the wall and creates a defocusing lens effect outside the cylinder.

Particle ray tracing simulations have been carried out to interpret the proton images. The simulation assumes an initially homogeneous proton beam and computes the deflection of single protons in a given electric field configuration. At the detector plane the resulting proton beam density distribution is obtained. The simulated proton image of figure 5.4 fits qualitatively well with measurements of beam collimation at an early stage (first 20 ps) of the interaction. Various field structures have been tested and
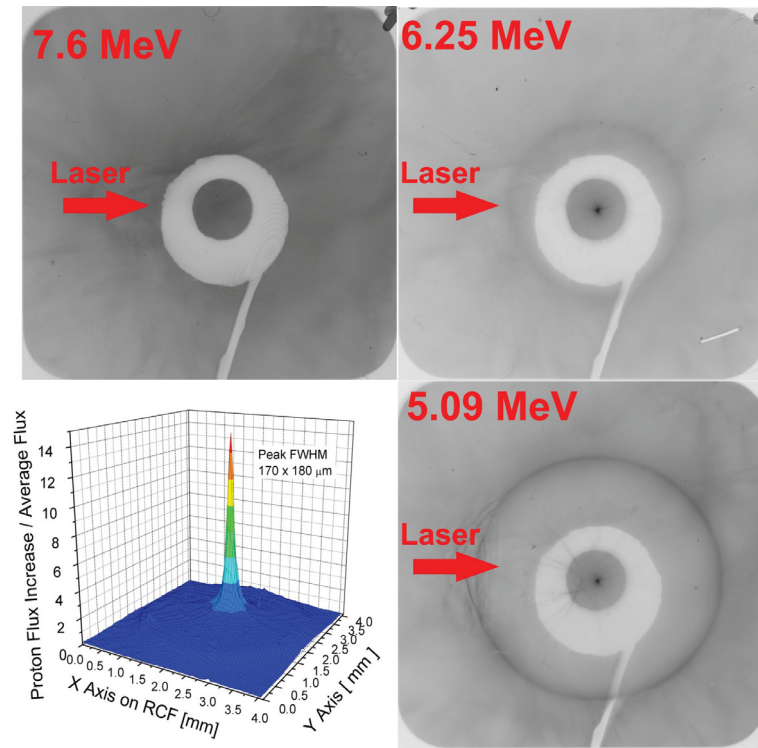
Figure 5.4: Beam focusing is observed for 6.25 MeV protons while the 7.6 MeV have exited the lens before the fields were present. A flux increase is observed.
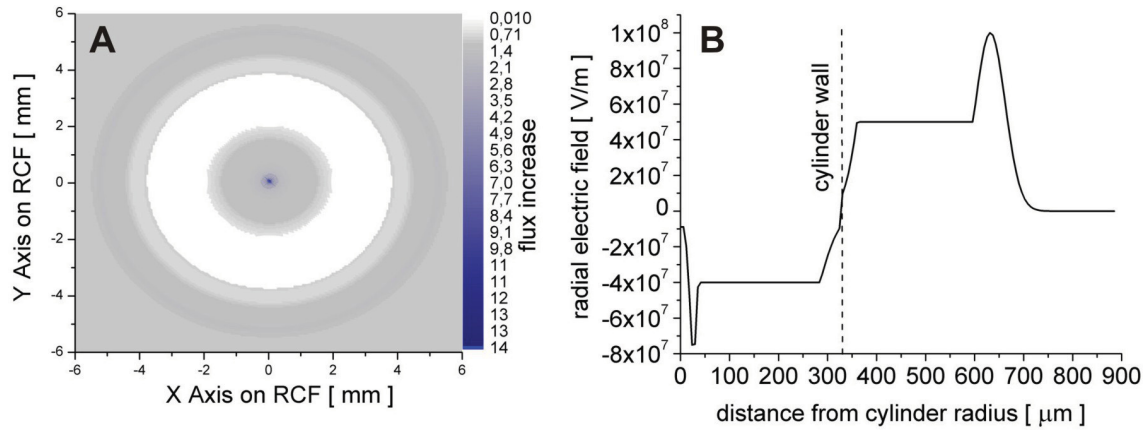

Figure 5.5: Particle ray tracing results. A) Simulated proton signal on RCF detector to fit the image of 5.4 (proton energy is 6.25 MeV). B) Radial electric field as used in simulation.

the electric field that resulted in the best agreement with the measurement is shown in
figure 5.5. The choice of this field is motivated by the field structure predicted by P.
Mora shown in section 2.5.2. It has to be mentioned that the measured proton signal
could be reproduced just by using a peaked field structure. Simulations show that 70
% of the protons passing through the cylinder can be found in the peak, the rest in
a low density background around the peak. In addition, the ray tracing also revealed
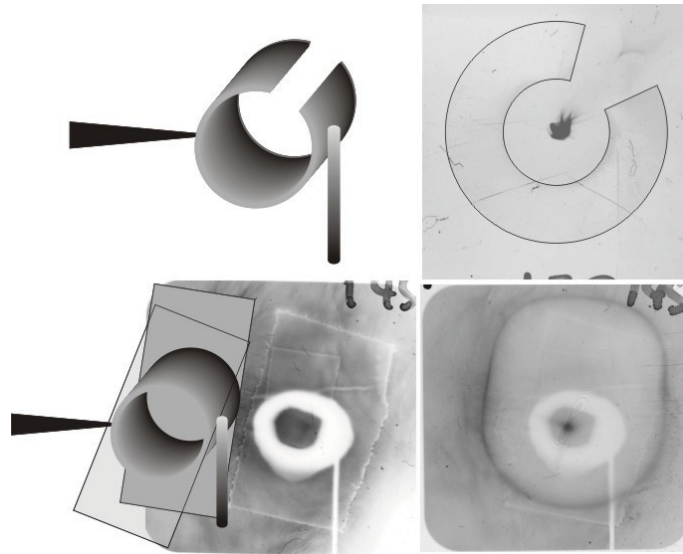that the outside electric field is expanding as a function of time.

Figure 5.6: Top. Focusing by a cylinder with a axial gap demonstrates that electric
fields create the lens. Bottom. Edge effects are not responsible for focusing since
closing the cylinder does not inhibit the lens.

To address the issue of the field's origin two tests were performed. In order to
focus protons passing along the axis of the cylinder one needs either radial electric or
azimuthal magnetic fields. Figure 5.6 shows the focusing properties of a cylinder having
an axial slit. The missing part should inhibit magnetic field effects. The experiment
demonstrates that indeed electric fields are responsible for proton focusing. The slit
brings in an asymmetry, the focal spot shows caustics in the direction of the slit. To
ensure that focusing is not produced by an edge effect at the cylinder ends we closed
the cylinder using 3 μm thick Al foil. Figure 5.6 proofs that focusing is still effective.
Note that in the classical case the hollow metal cylinder would act as Faraday cage if
charged up on the outside, and no field are expected inside the cylinder.

5.3 Focusing fields and field evolution

The goal of the first 2D simulations done with the PSC code is to check how the plasma evolves after an one sided irradiation of a cylinder. The incident laser pulse has a 1 μm wavelength and a transverse spot size on target of 2.6 μm (FWHM). The laser intensity is 1×10^{19} W/cm^2 and the pulse duration is 40 fs. The temporal and spatial (transverse) profiles are Gaussian and the pulse is injected at the left side of the simulation box. It interacts with the target at normal incidence, and its electric field is in the simulation plane (p-polarization). The peak of the pulse reaches the target surface 110 fs after the beginning of the calculation. The simulation box has a size of 50×50 μm^2 and sampled 12 grid points per μm and 26 particles per cell. The plasma is a 32 micron diameter cylinder with 2 micron thick wall composed of aluminum neutral atoms at 10 fold critical density 1.1×10^{22} atoms/cm^3. Figure 5.7
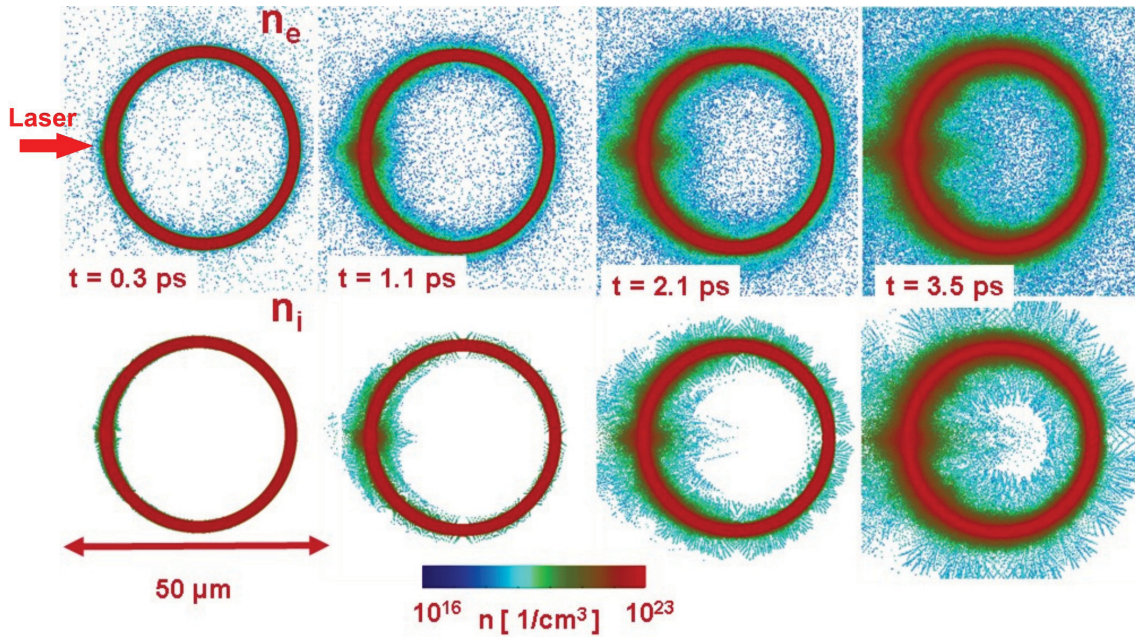

Figure 5.7: Time evolution of the electron and ion density at .3 ps, 1.1 ps 2.1 ps and 3.5 ps after the start of the simulation. The pulse is injected from the left of the simulation box. Although the irradiation is from one side the late time plasma expansion is surprisingly uniform.

shows the electron and ion densities late time evolution at .3 ps, 1.1 ps 2.1 ps and 3.5 ps after the start of the simulations. Although the irradiation was done just on one side

of the cylinder the plasma expansion seen is surprisingly uniform. Only at the rear side of the interaction point some stronger heating is observed. In the experimental reality having a long 3D cylinder surface this localized asymmetry will be dominated by the symmetric plasma expansion from the cylinder wall. We observe in the simulation a quasi neutral expansion both inside and outside of the cylinder. The next question to
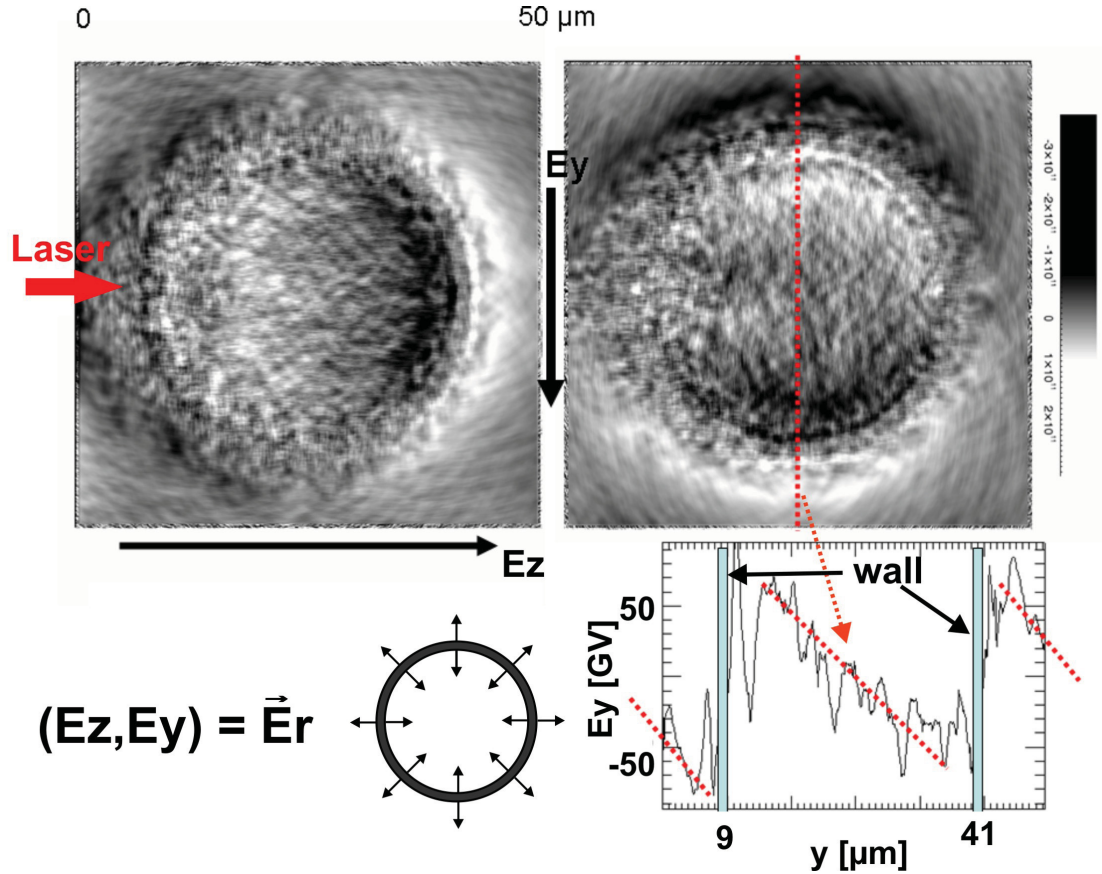

Figure 5.8: Snapshot of the electric field distribution at 2.1 ps. A radial electric field is built up.

be answered is if fields acting as a collecting lens on positive ions can be seen in the simulation. Figure 5.8 shows snapshots of the electric field distributions at 2.1 ps. The upper part shows the electric fields in the laser propagation direction (called z from now on) and in laser polarization plane (called y from now on). In the bottom part a line plot along the middle of the cylinder in y direction is shown. Indeed the fields found here point radially towards the center of the cylinder and can focus positive charged ions. The fields found in this simulation are in the order of several tens of GV/m.

5.4   Transient nature of the lens

Looking at the effect of the lens on a whole range of proton energies the transient nature of the lens can be measured. The protons are leaving the lens with different divergences and reach the detector plane with various spot sizes.
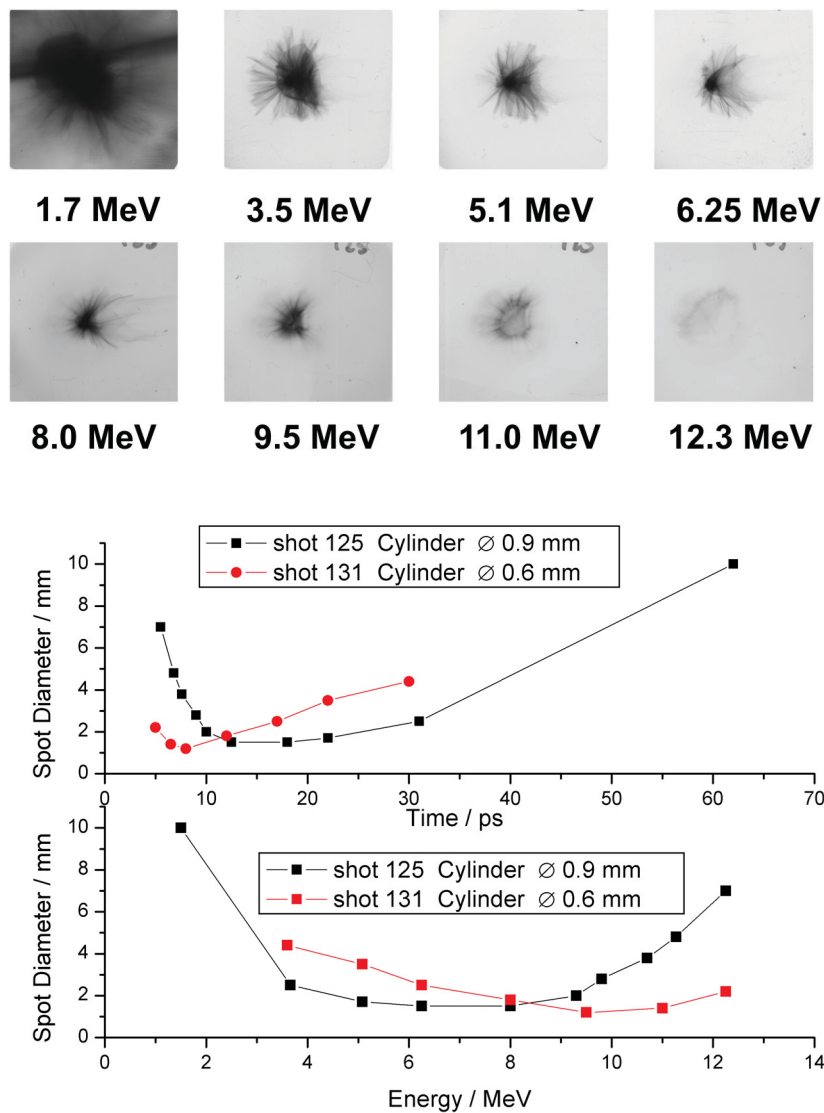

Figure 5.9: Raw RCF data for different energies for the shot # 125. The measured spot sizes for two different cylinder sizes are shown.

In figure 5.9 the spot sizes for the different energies are shown for a 0.9 diam and
0.6 diam cylinders 1 mm in length and placed 1 mm from the rear side of the proton
producing foil target. By measuring the spot size on the detector one can estimate
a typical time range of 15 ps where the lens efficiently deflects protons. The highest
proton energies reach the lens when the fields have just built up. The closing of a
annular structure is observed. The smallest spot size on the film is generated by
protons with energies between 6 and 8 MeV. For lower energies a bigger spot size at
the detector is observed. The differences of time where a minimal spot size is reached
is due to different fill up times of the cylinder with plasma. The plasma implosion
time is longer for the larger cylinder and at the same time the plasma is expected to
be colder when reaching the axis.

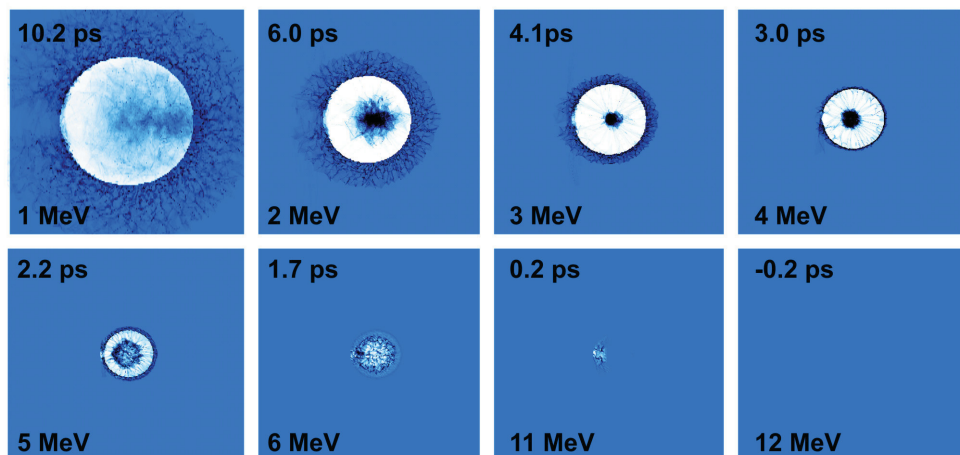## 5.5   Collimating Lens Effect on a Proton Beam

Figure 5.10: Shows the proton intensity at the simulated detector plane after ray tracing
the PSC computed lens effect on a proton beam for 1 MeV proton energy steps. The
transit time to the exit of the cylinder is given.

For a qualitative comparison between the experimental and computational data a
simulated focusing experiment has to be done. The trajectories of a poly energetic
proton beam have been ray traced through the time dependent electric and magnetic
field distribution post processed from the PSC output. The fields have been sampled
every 6 fs for 3.4 ps. A scaled down simulation with geometric properties as described

in section 5.3 was run. To simulate the 3D experimental situation the 2D PSC slice output has been repeated for a length of 100 μm. The center of the cylinder was placed 150 μm from the source and the proton distribution after passing the lens has been sampled at 212 μm corresponding to a virtual detector plane. The fields are triggered 4.2 ps after proton production so that 12 MeV protons will pass the lens unaffected. Any retardation effect in the plasma response perpendicular to the PSC simulation plane has been neglected. The ray tracing and image construction algorithm is done with the program developed in [84].

Figure 5.10 shows the linear proton density at the simulated detector plane for 1 MeV steps. Due to the time of flight and cylinder irradiation time set no deflection of 12 MeV protons can be seen. The 11 MeV protons are probing the rising edge of the interaction while the 10 MeV probe a time where the hot electrons have redistributed over the whole surface. For a longer time just small localized fields are probed. Beginning with the 6 MeV protons strong radial deflection can be measured resulting in a ringlike structure shrinking inside the cylinder and growing in diameter for the protons that have passed outside the cylinder. The 3 MeV protons exit the cylinder 4.1 ps after the cylinder has been irradiated and produce the smallest spot size at the plane of the detector, afterwards the spot becomes bigger. To estimate the contribution of the pure electric and magnetic fields the ray tracing simulation was repeated by inhibiting either the electric or the magnetic field. No lens effect is seen when turning the electric field off. The experimental measured features are qualitatively reproduced by the ray tracing simulation demonstrating that the physics of the process can be scaled up to experimental sizes.

5.6 Field Origin and Symmetry

After finding the focusing field coming from a plasma expanding from the wall into vacuum, the next question to be answered is what generates the plasma. At the same time an answer to the uniformity and symmetry of the plasma expansion is searched. To answer this questions a more detailed study of the interaction between the laser pulse and the cylinder wall was conducted. While the radius of the cylinder is much larger than the focal spot of the laser the study can be simplified to the interaction between a laser pulse and a solid foil as a good approximation.

A 2D simulation run was performed. The target was set up as a planar 10 fold
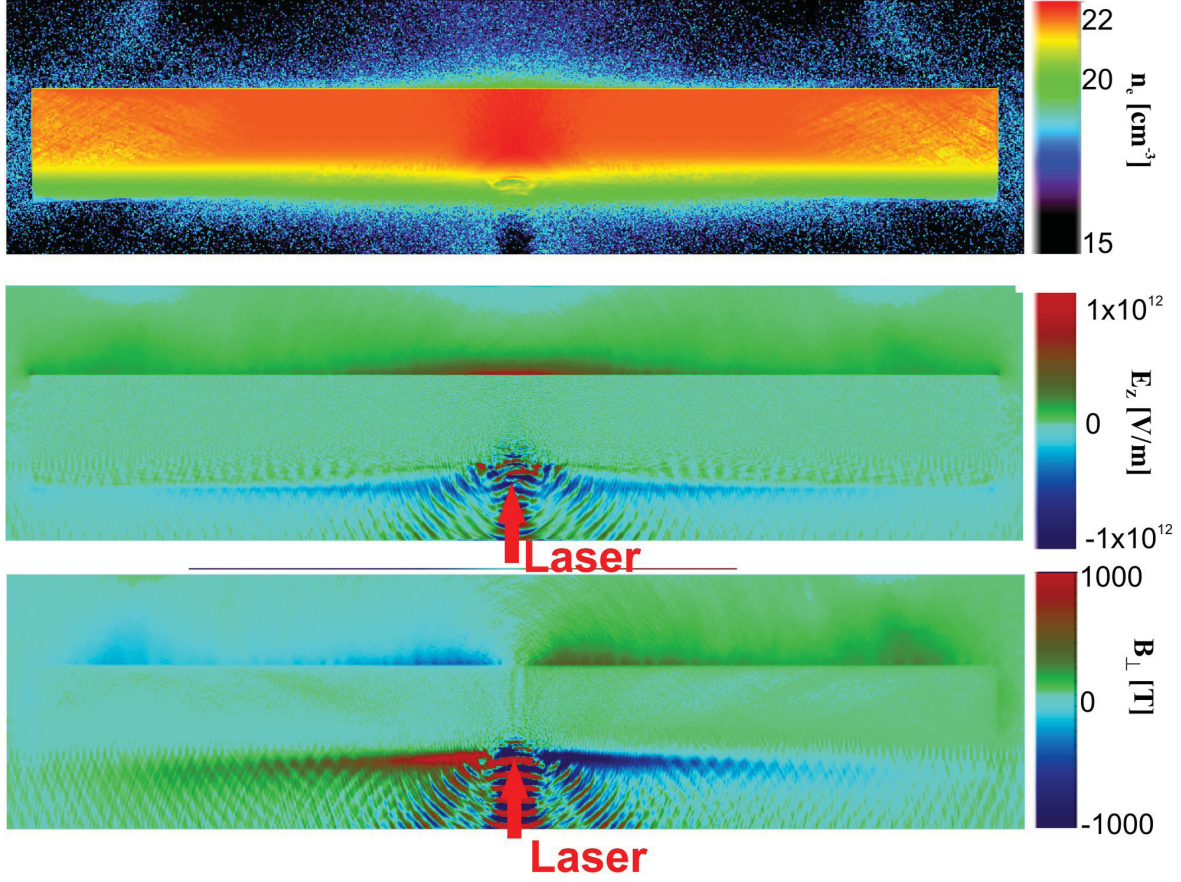
Figure 5.11: Showing snapshots at 800 fs after the beginning of the simulation of the electron density, the electric field in z direction and the magnetic field transverse to the simulation plane (from top to bottom)

critical density aluminium foil 74 μm in length and 5 μm in thickness with a preformed plasma with 1.5 μm scale length (FWHM) in front of the target. The simulation resolution is 25 grid points per μm and 50 particles per cell. The laser pulse has a Gaussian temporal profile with 300 fs FWHM focused on a 2.6 μm spot. Figure 5.11 shows a snapshot at 800 fs after the beginning of the simulation of the electron density, the electric field in the direction of laser propagation and the magnetic field transverse to the simulation plane. In figure 5.11 a strong electric sheath field with $E_z = 10^{12}$ V/m and an azimuthal magnetic field with $B_\perp = 1000$ T can be seen. The production of these fields can be explained as follows.

As soon the laser pulse hits the preformed plasma in front of the cylinder it will

begin to heat up electrons. The main absorption mechanism in a small gradient scale plasma is the $\vec{j} \times \vec{B}$ heating. Characteristic for this mechanism is the creation of two electron bunches per laser cycle.

The typical electron temperature can be estimated as $T_{hot} = [\sqrt{(1 + I\lambda^2/1.4 \times 10^{18})} - 1] \times 511$ keV [88]. For an intensity of $I = 3 \times 10^{18}$ W/cm^2 one calculates $T_e \simeq 370$ keV. These electrons will spray through the cylinder wall with an opening angle that can be estimated from [71]: The longitudinal momentum in the laser field can be approximated by $p_{\parallel} \sim a^2/2$ where $a = eE/m_e c\omega$ denotes the dimensionless laser amplitude. The transverse momenta in the laser field is proportional to a, $p_{\perp} \sim a$. The opening angle θ is given by $\tan\theta = p_{\perp}/p_{\parallel}$. For $a = 2$ the divergence angle is $\theta = 45°$. These estimates are consistent with the hot electron production as seen in the PSC simulations. The electrons are energetic enough to penetrate the solid foil or cylinder wall.

In an initial stage at the back side of the interaction region the electrons build up a strong electric Debye-sheath field E_s leading to ion acceleration. A fraction of the electrons will be electrostatically trapped thus returning towards the surface. As a result of the spring fountain like motion of electrons a strong magnetic azimuthal field $B_{\perp}$ is excited perpendicular to the plane of motion [70, 69]. This field propagates at the speed of light following the hot electrons. At the same time the electrons are pushed sideways by the Lorentz force in the direction of $E_s \times B_{\perp}$ increasing the extension of these fields. While extending these fields will ionize the surface creating a lower energy electron population. This wall plasma will expand into vacuum long after the laser pulse has passed sustaining the electric fields pushing ions away from the surface.

The whole physical scenario can be applied also on a cylindrical curved target as summarized in figure 5.12.

Two conditions as the ones derived in [89] have to be fulfilled for development of a symmetric electric field. The first is that the hot electrons have to redistribute on a shorter time scale τ_{hot} than the plasma implosion time inside the cylinder τ_p. Assuming that the cylinder wall is irradiated at half of its length the hot electrons have to travel for a maximal time $\tau_{hot} = \sqrt{\pi^2 R^2 + L^2/4}/c$ with c the speed of light. The plasma implosion time can be estimated with the ion velocity as $\tau_p = R/c_s$, with $c_s = \sqrt{Zk_B T_e/m_i}$. Symmetric expansion imposes:

$$
\begin{aligned}
1 &\gg \frac{\tau_{hot}}{\tau_p} \\
&\gg \frac{\sqrt{\pi^2 R^2 + L^2/2^2}/c}{R/(Zk_B T_e/m_i)^{1/2}}.
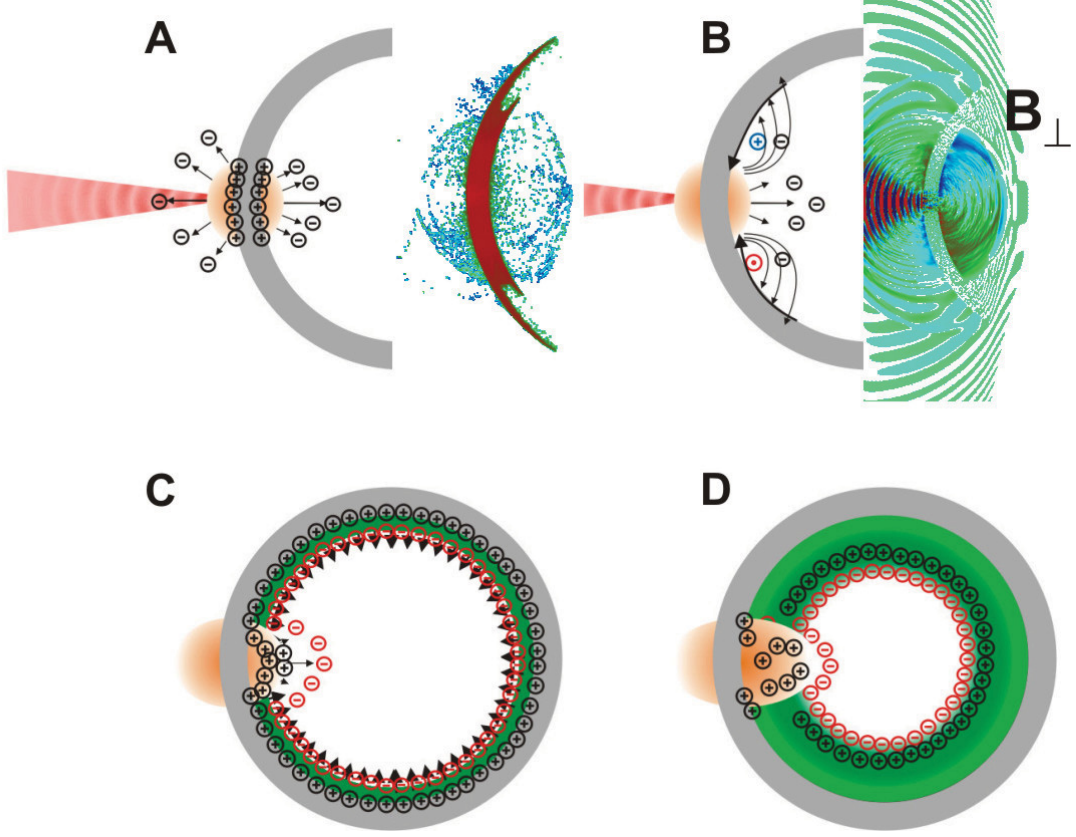\end{aligned}
$$

Figure 5.12: Principle scheme of the plasma generation and evolution inside a cylinder irradiated by a high intensity laser pulse. A) hot electrons are accelerated. B) The electron fountain motion drives azimuthal magnetic fields. The hot electrons are pushed sideways extending the fields, C) A surface plasma is created, D) The plasma expands towards the vacuum sustaining radial electric fields.

For conditions such as a imploding hydrogen plasma with T_e some tens keV, a cylinder radius of 350 μm and length of 3 mm this condition is easily satisfied. The hot electron redistribution is 35 times faster than the plasma implosion.

    The second condition for the formation of a symmetric plasma is that the collisional cooling time of the hot electrons is again slower than the redistribution time around the cylinder. The electron-electron collision frequency is given by [90]: $\nu_e = 2.9 \times 10^{-6} \lambda n T_e^{-3/2}$ s^{-1}. For a moderate hot electron temperature of 100 keV colliding with a solid density the collision time is $\tau_{col} \simeq 10$ ps. Thus the hot electrons have the possibility to move collisionless along the surface whilst loosing very little energy.

5.7   Divergence manipulation

The evolution of the beam size has also been studied, in the same experimental conditions as in figure 5.3, for the 7.5 MeV protons, as a function of the distance between the RCF stack and the proton source (figure 5.13). Note that for this energy, the beam size is only 8 mm after 70 cm of propagation whereas freely propagating, the size of the beam having a source divergence angle of 10 deg without transmission through the cylinder would have been 260 mm. This means that a narrow spectral range of energies in the proton beam can be ballistically transported over a long distance efficiently by the lens reducing the beam divergence to 0.3 deg for a narrow spectral range. It has to be mentioned that this can just be achieved if the beam is quasi-neutral an intrinsic attribute of laser accelerated proton beams. This divergence reconstruction
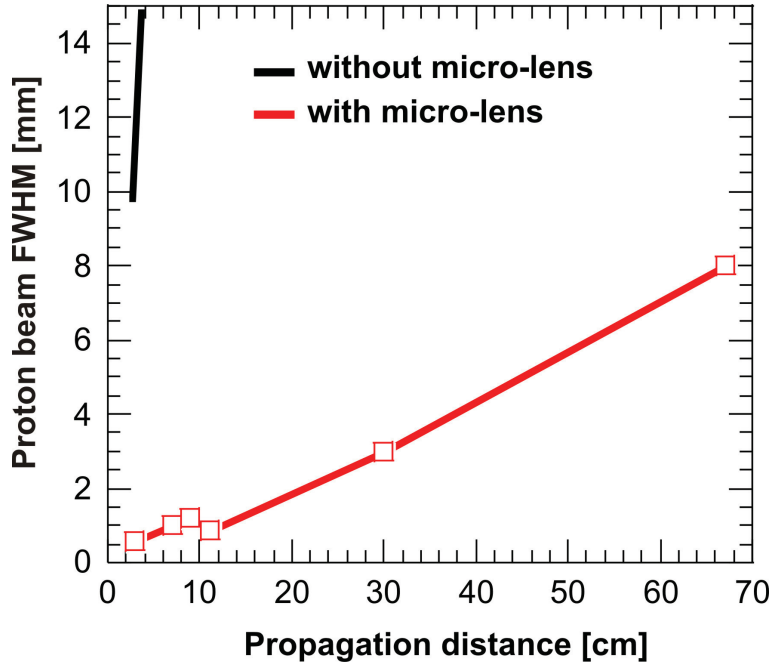

Figure 5.13: Scan of RCF position for retrieving the beam divergence of a 7.5 MeV proton beam

by variation of the detector position over long distances works reasonable just for the energies that have a high degree of collimation. To measure the divergence behavior of several energies strongly affected by the lens another experiment has been carried out and is presented in the next section.

5.8   Focal Length Properties

This experiment was carried out at the TAW of Vulcan at the Rutherford Appleton Laboratory. The experimental setup is shown in figure 5.14. The distance from the Au proton production foil and the cylinder entrance was 1 mm. The cylinder material was Dural (95% Al, 4% Cu, 1% Mg) with a length of 2 mm and an outer diameter of 810 μm. The wall thickness was 50 μm and the cylinder was held by a 100 μm tungsten wire. In order to investigate the energy dependent divergence of the proton beam altered by the micro-lens a thin Cu mesh with 2000 lines per inch was placed 10 mm after the exit of the cylinder. Protons with different energies will pass through the cylinder at different times and will be influenced by different evolution stages of the micro-lens. Thus the protons will exit the lens with different angles. Hence on the RCF different magnified images of the mesh will be recorded. In order to have enough magnification on the detector plane the RCF had to be positioned ~10 cm from the cylinder exit. At this distance the proton beam was very diluted and to maximize the contrast of the measurement the proton beam was subapertured with a 200 μm diameter pinhole that was placed 4.5 mm after the cylinder exit. Knowing that the distance between proton foil and mesh was set with several tens of μm precision the mesh geometric magnification defines the plane of the RCF detector, in the case of figure 5.15D (called 0-order) at 100.3 mm. The magnification in this case was 8.9 fold. The unaltered projected mesh can be seen in figure 5.15 and is produced by high energy protons and electrons that were not affected by the not yet triggered micro-lens.
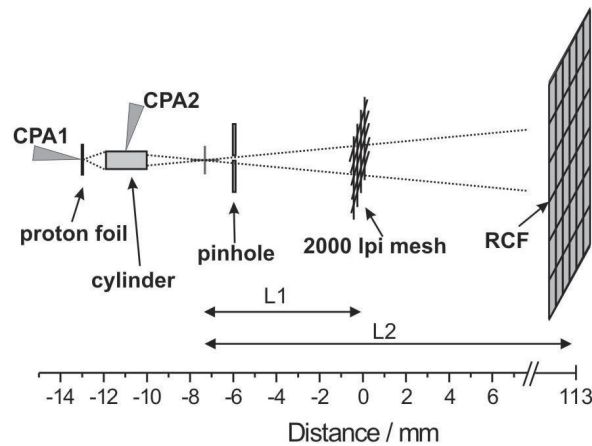

Figure 5.14: Experimental setup used for focal length measurements of the lens

Protons that are focused between the cylinder exit and the mesh will project a magnified mesh on the detector plane. Figure 5.15A-C top part shows the mesh projection by protons with energies of 1 MeV, 3.15 MeV and 4.4 MeV. To extract the periodicity of the magnified mesh the data was contrast enhanced and a double 2D Fourier transformation was performed masking out everything but the first order in the Fourier space. From figure 5.15 A-C bottom part a magnification of M=11.4, 12.2, 14.8 has been computed for the 1 MeV, 3.15 MeV and 4.4 MeV protons respectively. Simple geometrical ray tracing yields a focal length of .4 mm, 1 mm and 2.7 mm from the exit of the cylinder for the three energies mentioned above. In this case the calculated laser intensity hitting the cylinder was 8.5×10^{18} W/cm^2. By reducing the pulse energy and thus also the intensity by 20% to 6.7×10^{18} W/cm^2 and repeating the measurement a focal length (again compared to the exit of the cylinder) of .9 mm for 1 MeV, 2.8 mm for 3.15 MeV, and 4.7 mm for 4.4 MeV protons was determined. From
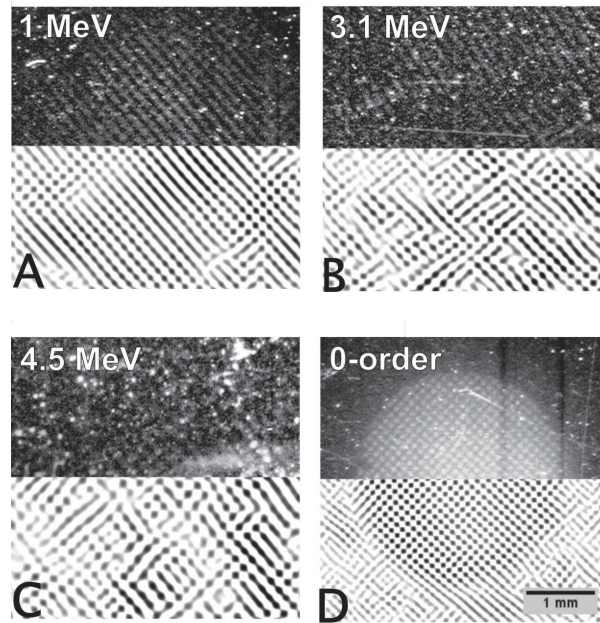

Figure 5.15: Divergence reconstruction data, top part show raw dose deposition on RCF, bottom part shows enhanced mesh images after Fourier filtering.

the deflection strength a time integrated average radial electric field can be estimated. Let us consider that the protons begin to be deflected as soon as the lens has been triggered and they will be deflected up to the time they will exit the cylinder or the field has collapsed. From measurements that are to be presented in section 5.12.2 it is

deduced that the field time evolution is peaked around 20 ps, collapses between 20 and 60 ps after triggering the field and expands over the cylinder surface close to the speed of light. Taking into account the optical delay between the two laser pulses and time of flight of the protons the following scenario of the field history was reconstructed. The 4.5 MeV protons are 80 μm before the exit of the cylinder when the lens is triggered. In other words having a transit time of 15 ps these protons will be deflected by the rising edge of the field and they will exit the cylinder before the maximal the field strength is reached. The 3.15 MeV protons are inside the cylinder during the whole interaction. Therefore they will be deflected the most. The 1 MeV protons are outside the cylinder when the lens is irradiated. They will reach the focusing field just when this field is on the collapsing edge, therefore feeling lower field strength. The time averaged field strengths are given in fig 5.16. Summarizing: several GV/m field strengths have been measured to deflect efficiently the proton beam and cause the lens effect.
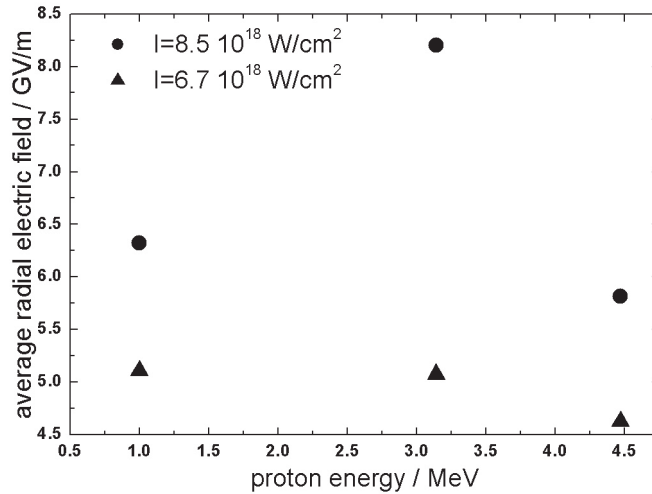

Figure 5.16: The radial electric field averaged over the proton transit time inside the cylinder is shown. 4.5 MeV protons exit the cylinder before the maximum field strength is reached. The 3.15 MeV protons are subject to the maximum field. The 1 MeV protons enter the cylinder on the collapsing edge of the field.

To understand these results further postprocessing of the PSC simulations was conducted. The imploding plasma electron temperature can be extracted from the PSC output. The plasma evolution the laser pulse intensity was varied from 1×10^{19} W/cm^2 also to 5×10^{18} W/cm^2. Figure 5.17 shows a frequency count plot of one

momentum component of all electrons present in the simulation. The plots can be fitted by an exponential slope decay with a temperature around 13 keV for the 1×10^{19} W/cm^2 simulation and around 6 keV for half of the intensity.
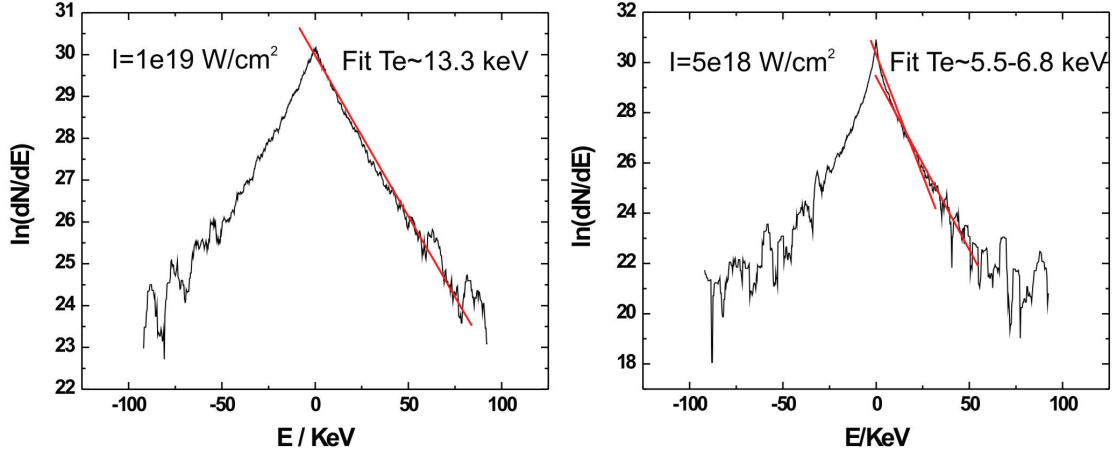

Figure 5.17: Impulse distribution for simulation runs with an average intensity of 1×10^{19} W/cm^2 (left) and 5×10^{18} W/cm^2 (right). The slopes are fitted with an exponential decay first order.

The average ionization stage extracted from the simulation is 4 respectively 3 for the lower intensity run.

A closer look on the radial electric field structure and time evolution reveals a close resemblance with the field structure presented in section 2.5.2. The field (see figure 5.18) is initially decaying exponentially with distance from the target. Later on a plateau ending with a peak structure develops and runs away from the target. The insets in figure 5.18 show the time evolution of the position of the field peak in respect to the cylinder wall. The model of plasma expansion into vacuum by P. Mora gives an expression for this distance:

$$x_{front} = c_s t [2 \ln(\omega_{pi} t) + \ln 2 - 3]$$

where $c_s = (Z k_B T_e / m_i)^{1/2}$ denotes the ion acoustic velocity and $\omega_{pi} = (n_{e0} Z e^2 / m_i \epsilon_0)^{1/2}$ the ion plasma frequency.

By using the average ionization states extracted from the PSC simulation and using the above shown expression the electric field peak position can be fitted (red continues

line in insets of figure 5.18). As a result of the electron temperature fit one finds: 13.2 keV for the 1×10^{19} W/cm^2 laser intensity and 5.4 keV for the 5×10^{18} W/cm^2 simulation run. These fitted electron temperatures are consistent with the temperatures directly evaluated from the PSC output. Thus the electric fields seen in the simulations can be understood with the analytical model of a plasma expanding into vacuum. Still some differences are to be expected. While the upper model is 1 dimensional the expansion from the cylinder walls develops in a 2 dimensional cylindrical geometry. The Laplace operator (in the Poisson equation) for a cylindrical geometry has a radial dependent component that manifests in different peak field strengths lower inside and higher outside the cylinder effect seen in the simulation.
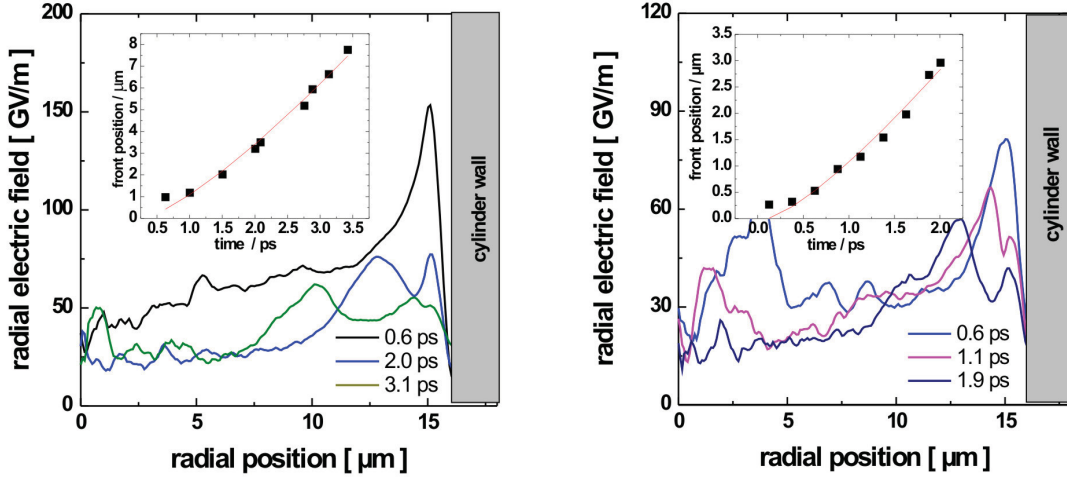

Figure 5.18: Radial electric field evolution for simulation runs with average intensity of 1×10^{19} W/cm^2 (left) and 5×10^{18} W/cm^2 (right). The insets show the position of the electric field peak. The red line fits the points with the peak field position as predicted by the model of plasma expansion into vacuum by P. Mora.

This result explains qualitatively the laser irradiance dependence of the focal length found in 5.8. The maximal electric field is a function of the electron temperature. By reducing the laser energy the plasma is less heated and longer focal lengths are measured. A computational scaling law of the expected electron temperature as a function of the laser intensity is derived later in 5.14.

5.9 Absolute Flux Measurements

The last question to be addressed concerning the geometrical properties of the lens of interest for application is the number of protons that can be focused. The simplest way to do this is using an absolutely calibrated detector. This experiment has also been done in the RAL setup as presented in the last section. For this task the calibration of several RCF types has been conducted at the Max Planck center for atomic physics in Heidelberg. As a rough estimation one can say that for the measurement shown in 5.19 B 3×10^8 protons at 5 MeV are found in a 300 μm spot. This number neglects the energy deposition contribution of protons with higher energies than the energy stopped by the layer of interest and of the electrons that were transmitted by this layer. A complementary absolute flux measurement has been done with the technique
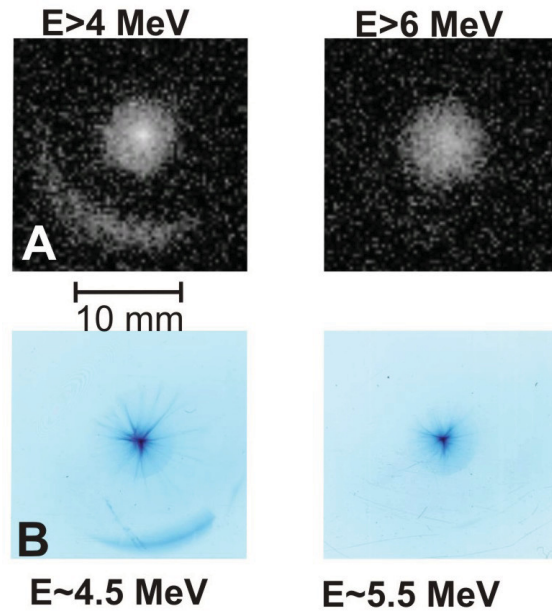

Figure 5.19: Raw dose distribution for measuring the absolute flux of focused protons. A: the distribution as induced on an Image Plate by activation of ^{63}Cu. B: measured with a HD-810 Radio Chromic Film

of induced contact radiography developed by Rob Clarke at RAL. This method uses the nuclear activation of a solid foil stack by protons. In our case Cu foils of 25 μm in thickness are employed. Cu can be activated by protons via two nuclear channels with significant cross sections ^{63}Cu(p,n)^{63}Zn and ^{63}Cu(p,n)^{65}Zn. Both Zn isotopes decay

over $\beta+$ ^{63}Zn having a half-life of 38 min, ^{65}Zn of 244 days. The activation cross section is maximal for 10-15 MeV protons with a lower energy cutoff around of 4 MeV. The use of a foil stack gives directly a coarse energy resolution similar as for RCF stacks. The activation of each foils in the stack must be individually measured by a calibrated $\gamma-$detector yielding the total number of Zn isotopes activated. Now the foils are placed in contact with a Fuji image plate. Here the remaining Zn isotopes decay and the radiation induces a two dimensional profile on the IP. After one hour of exposure the IP is read. In this way the absolute number of activated Cu nuclei and their distribution can be measured. With similar experimental conditions as in the RCF flux measurement one finds 2.5×10^4 induced isotopes by 5 MeV protons. From the number of reactions R per 25 μm (foil thickness) $R = N \times \sigma = 2.1 \times 10^{-5}$ where N is the number of atoms per cm^{-3} and σ the reaction cross section (in cm^2) one obtains 1.2×10^9 incident protons. From the two dimensional distribution one concludes that 0.15 of the protons can be found in a 600 μm radius around the peak. Comparable values of focused protons could be found both by measuring with calibrated RCFs and by the induced contact radiographic technique.

5.10   Energy Selection with the Micro-Lens

The previous sections showed that the laser triggered micro-lens has a very transient and chromatic behavior. By sub aperturing the beam the energy selection should be possible. Figure 5.20 shows the spectrum obtained in the same experimental configu-
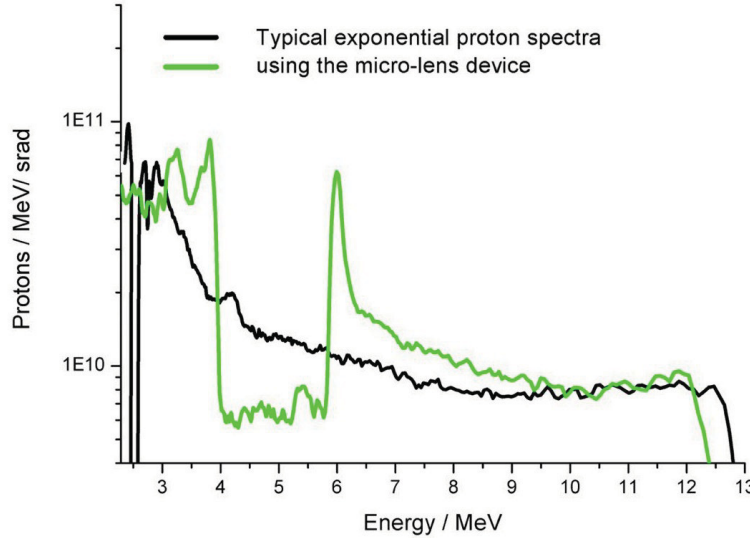
Figure 5.20: Proton spectra measured in the experiments using a magnetic spectrometer without micro-lens (black line) and with the micro-lens (green line) The distance between the micro-lens and the proton source is 4 mm.

ration as in section 5.2 by replacing the RCF detector with a magnetic spectrometer with an entrance slit of 250 μm positioned 70 cm away from the proton source. As a reference, also a typical exponential spectrum is shown collected in the same conditions without the micro-lens. The data shows clearly the energy selection capability of the micro-lens: due to selective collimation of the 6.25 MeV protons, these could be transmitted more efficiently through the spectrometer slit (acting as an angular filter), and their density after the slit in the spectrally dispersed plane is enhanced as compared to the free-space expansion case. For this shot, the 6.25 MeV protons entered the cylinder at -80 ps relative to the peak of the CPA2 pulse whereas their transit time through the cylinder is 86 ps. Note that we obtain an energy spread of 0.2 MeV - limited by the spectrometer energy resolution - for the peak located at 6.25 MeV.

In an other experiment done in the RAL setup, the optical delay between the

two laser beams was varied. The location of this peak on the energy axis can be tuned selectively, therefore allowing to tailor the energy distribution of the transmitted beam, a necessary step for many of the applications mentioned earlier. Compared to the first spectrum shown in figure 5.21 the second and third spectrum are measured with a relative delay of 23 ps and respectively again 67 ps later. The spectral peak position scales exactly with the time of flight difference of the protons to the lens exit. While in the first graph a peak of around 7 MeV is measured this peak is moved to 5.5 MeV and 3 MeV for the later times.

This is a robust knob for tuning the lens for applications. By repeating the shots and keeping the optical delay constant no change in peak position was measurable.
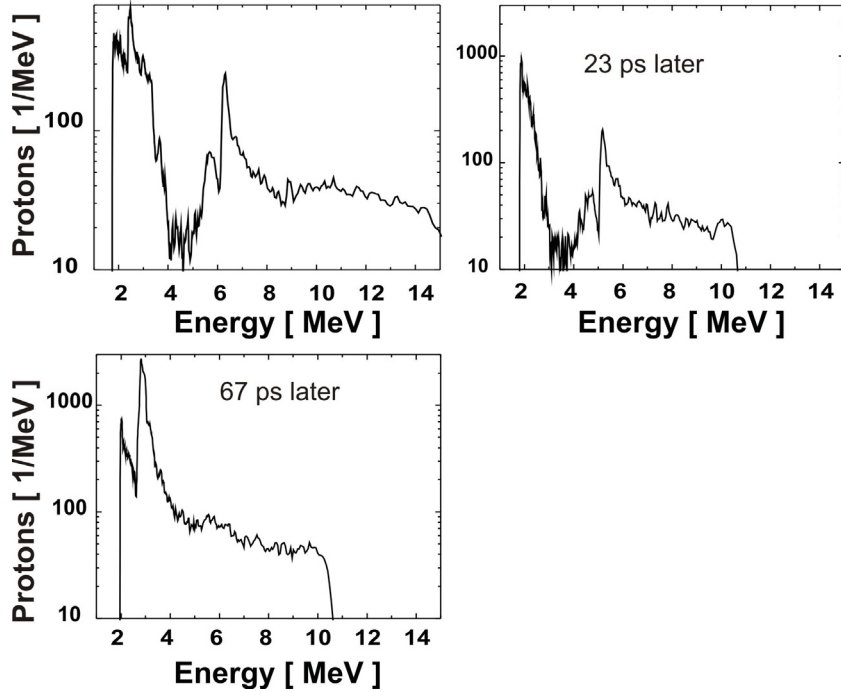

Figure 5.21: By varying the optical delay between the laser beams, the location of this peak on the energy axis can be tuned selectively, therefore allowing to tailor the energy distribution of the transmitted beam, a necessary step for many of the applications mentioned earlier.

The energy selection lens capability is based on its strong chromatic behavior. The experimental deduction that the protons almost exiting the cylinder will leave quasi-collimated leading to a flux increase a specific spectral range can also be illustrated by postprocessing the PIC simulation.
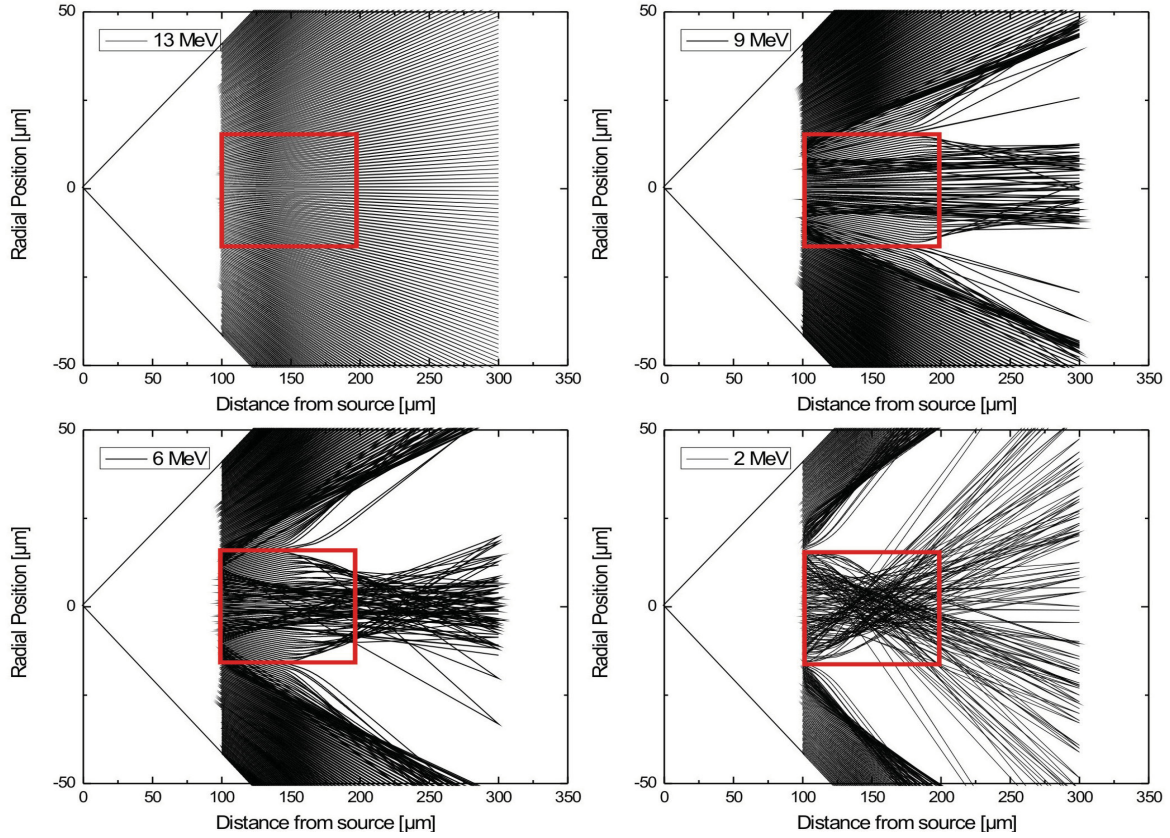
Figure 5.22: Ray tracing the path of a proton beam trough a downsized simulated cylinder. The simulations demonstrate that collimation and focussing of the beam is an effect of transit time in the cylinder.

Figure 5.22 shows the ray traced paths of protons with different energies in the same geometry as in section 5.5. The 13 MeV protons pass the cylinder before lens triggering. The 9 MeV protons almost exit the cylinder feeling the influence of the beam just for a brief time thus remaining highly collimated. The flux of this energy will be enhanced in the measured far field distribution. The 6 MeV find themselves in the center of the cylinder while the field is generated. Therefore focusing of the beam is computed. The 2 MeV protons feel the whole time evolution of the field thus being strongly focused. This ray tracing simulation confirms the experimental result shown in section 5.8. Moreover it is seen that the transient nature of the lens (collimation, focusing) is primary an effect of the total transit time of the protons in the cylinder while the fields are active, the proton energy plays a secondary role.

5.11 Investigation of the Transport of the Plasma Heating Electrons

The last sections answered experimentally questions relevant for applicative issues and concerning the action of the lens on a proton beam. With the help of PIC simulations the question how the lens is created was addressed. The next sections will engage the question of the lens generation from the experimental point of view. While the experiments shown in section 5.1 demonstrated that an electric field of several GV/m inside the cylinder is responsible for the action of the lens the explanation was that the field comes from a plasma inside the cylinder. Due to the thickness of the cylinder wall electrons are the natural candidates that could transport enough energy in order to generated the plasma needed. So the question to be experimentally addressed in this section is how the electrons responsible for plasma creation spread inside and outside the cylinder. Let us assume that the electrons are produced just at the interaction point between laser and cylinder wall. From here they could spray in a ballistic way or due to more complicated interaction spread along the wall. In order to clarify this issue two experiments employing proton probing and optical shadowgraphy were carried out.

5.11.1 Proton Probing

The setup used for the study of the lens is similar to the one needed for a proton imaging experiment this technique was used first to study the electron transport. The typical length of few mm of the cylinders used until now in the experiments are not suitable since it would reduce the time resolution of proton imaging. At the same time a too short cylinder would allow the plasma from the exterior and the interior of the cylinder to mix together making the analysis difficult. A good compromise between time resolution and decoupling the cylinder interior and exterior has been found in probing the interaction of a 450 μm long and 800 μm diameter cylinder. The cylinder was set 3 mm away from the proton generation foil. The probing result is shown in figure 5.23. Protons with 14 MeV energy (the layer called t) are timed to probe the rising edge of the electron spread. 2 ps later deflection on one half of the cylinder is detected, at $t + 4.5$ ps on the whole cylinder. Later the deflection gets stronger and extends to the holding wire.

In order to distinguish if the electrons are flowing along the surface we redo the
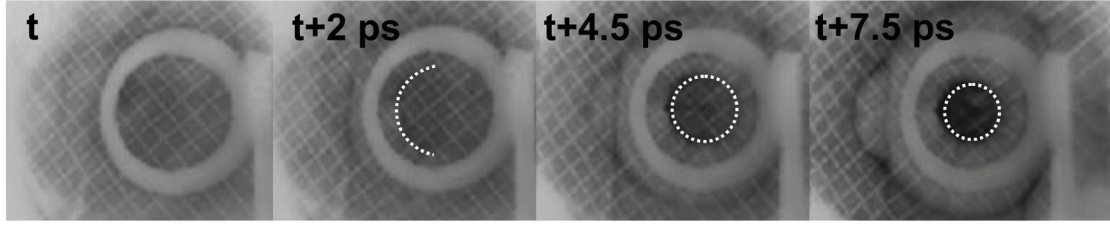
Figure 5.23: Probing the early stage of interaction with a short cylinder. The initial stages of the field extending around the cylinder can be followed.

experiment using this time two cylinder halves of the same dimension as above but separated by a 200 μm gap. Contrary to figure 5.23 even at later times fields can be detected just on the irradiated half. This is a very strong argument that the electron flow is bound to the surface and cannot extend over the gap.
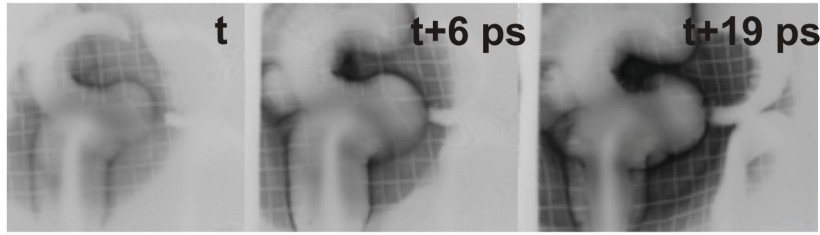

Figure 5.24: Probing the early stage of interaction with two cylinder halves separated by 200 μm. Fields are built up just on the irradiated half demonstrating that energy transport is bound to the surface.

5.11.2 Electron propagation test

To study the propagation and extension of the heating by a hot electron current, simulations irradiating a full cylinder and a cylinder cut in two halves with a gap of 10 μm were performed. Figure 5.25 s A-C shows the evolution of the magnetic field in time and space on the full cylinder. We notice that the magnetic field extends along the surface and loses strength in time, while the energy is used for wall plasma heating.

Figure 5.25 D-F show the simulations with the two halves of a cylinder. As in the experiment in section 5.11.1 the gap inhibits the electron transport. The current

Magnetic field perpendicular to simulation plane $B_\perp$
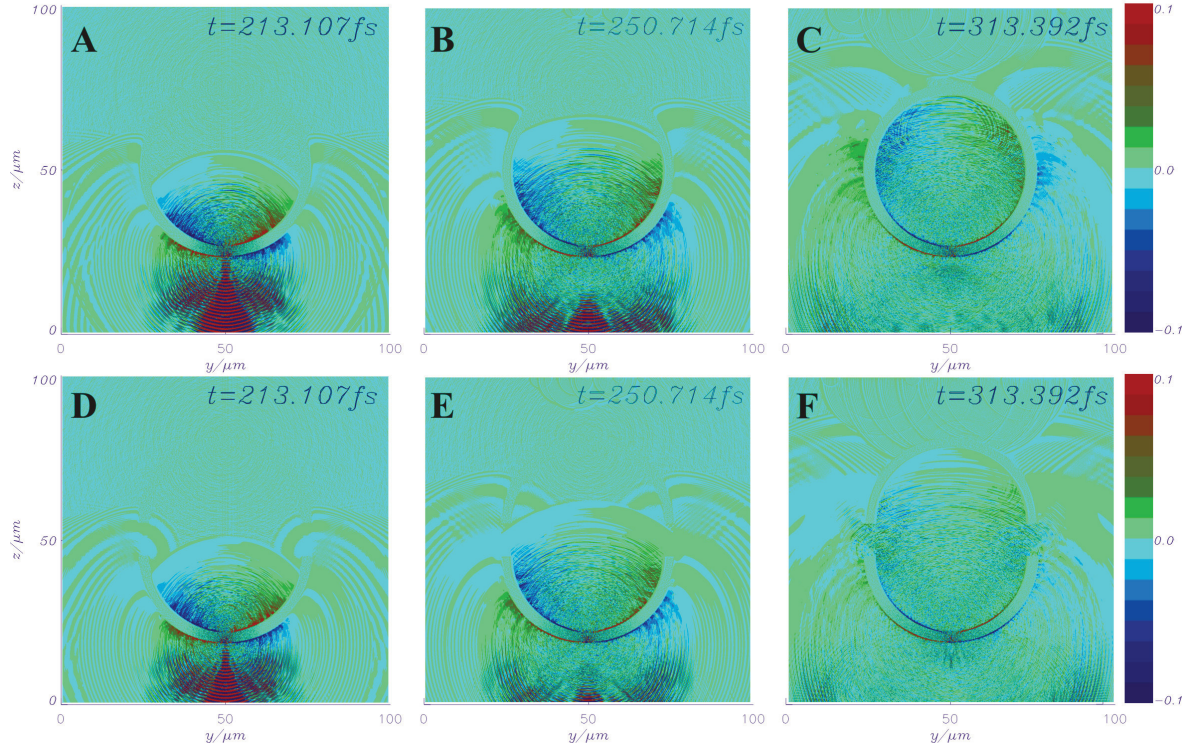
Figure 5.25: Magnetic field perpendicular to the simulation plane. In the top row the magnetic field extends in time over the full cylinder. In the bottom row the gap between the cylinder halves inhibits the electron transport along the cylinder surface, the magnetic loop breaks.

cannot follow the surface while extending and jump over the gap thus strong reduction of the magnetic field is observed. Later on significant reduced heating of the non irradiated cylinder half is observed in the simulation. The radial expanding plasma is not generated on the non irradiated half and no focusing field is built up similar as in the experiment.

5.11.3   Optical Probing

Via optical probing the late time plasma evolution can be measured. The motivation behind this experiment was probing the symmetry of the imploding plasma responsible for the lens effect. For this experiment the experimental setup (again in the LULI configuration) was changed as follows. The proton production foil was removed, and the CPA1 was exchanged by a collimated mJ probe beam doubled to 2ω with a SHG crystal. This beam was also compressed to 350 fs. Optical probing of the cylinders was made for different time delays between the CPA2 beam and the probe beam.
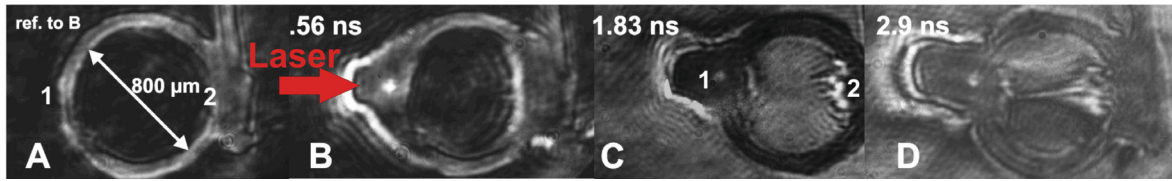

Figure 5.26: Optical shadowgramms probing the late stage plasma evolution at times of B 564 ps, C 1.83 ns and D 2.9 ns after the shot pulse. A shows the reference image for B taken before the interaction. The laser is hitting the cylinder from the left.

Figure 5.26 shows the snapshots of the plasma evolution produced by CPA at time delays of 564 ps, 1.83 ns and 2.9 ns after the interaction. The laser is hitting the cylinder from the left. Surprisingly these images show strong plasma expansion just at the interaction point (called 1) and at a point opposite to the interaction point at the interior of the cylinder (called 2). The plasma seen at the interaction point is associated with the direct ablation of target material by the laser pulse. Beside of this two jets no significant heating from the remaining walls is observed. The plasma at the point 2 shows a strong filamentary structure getting thinner towards the cylinder axis. In order to elucidate the origin of this jet an experiment with two separated cylinder halves where just one half is irradiated by a laser pulse has been carried out. The experiment should test if the jet is created by electrons and ions accelerated from the rear side of the interaction point that cross the cylinder interior and are stopped by the wall. If this hypothesis would be true the jet should appear.
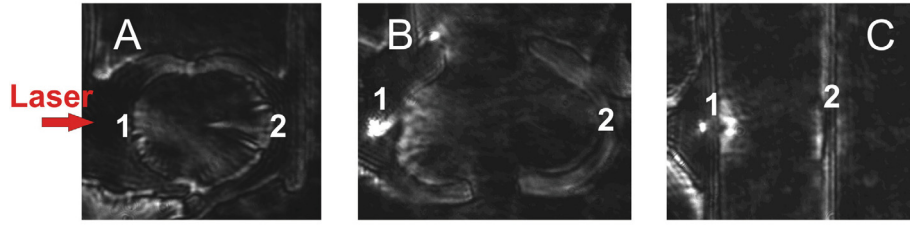
Figure 5.27: Optical shadowgramms probing the plasma evolution at a delay of 1.77 ns from two cylinder halves separated by a gap 100 μm (A) and 400 μm (B) wide and (C) from two foils separated by the cylinder diameter. The laser was incident from the left.

Figure 5.27 shows the result. The optical shadowgramms probe the late stage of the plasma evolution at a delay of 1.77 ns. In A where two cylinder halves are separated by 100 μm the plasma jet at position 2 is present. With a separation of 400 μm no jet can be detected any more. As a test the interaction from two foils separated by the cylinder diameter are also shown in C showing also no jet and demonstrating that the ballistically sprayed electrons or ions are not related with the jet appearance. Thus the jet emergence is related with energy transport along the wall. As seen in the previous section the expansion of the fields driving the lens is bound to the wall, hence a correlation between focusing and the late time jet emergence at position 2 must exist.

From the optical probe measurement a plasma expansion velocity $\simeq 1 \times 10^5$ m/s is measured. Assuming that an aluminium plasma expands with ion sound speed this would correspond to an electron plasma temperature of $T_e = 2.8/Z$ keV where Z is the charge state of the plasma.

5.11.4   Localized heating

A closer look at the field distribution inside the cylinder could explain the formation of a plasma jet observed in the last section via optical probing. As shown in section 5.11.2 associated with the motion of the hot electrons along the surface is the generation of an azimuthal magnetic field. We have the situation were two opposite oriented magnetic fields extend along the surface and because of the geometry coalescence of these fields will occur. During this event called magnetic reconnection the magnetic field topology

will change. As a result the magnetic field energy dissipates and a strong localized and oriented heating of electrons and ions is observed [91]. In our case the reconnection takes place on the cylinder side opposite to the irradiation point. For studying this phenomena a more detailed simulation was set up. A 100 μm simulation box contains a 50 μm diameter cylinder 5 μm in thickness consisting of simply ionized aluminium. A 250 nm thick layer of Hydrogen is added at the surface. The simulation was sampled with 4000×4000 grid points and 26 particles per cell. For this run a 100 fs FWHM Gaussian pulse with an intensity of $I = 1 \times 10^{19}$ W/cm^2 was used.
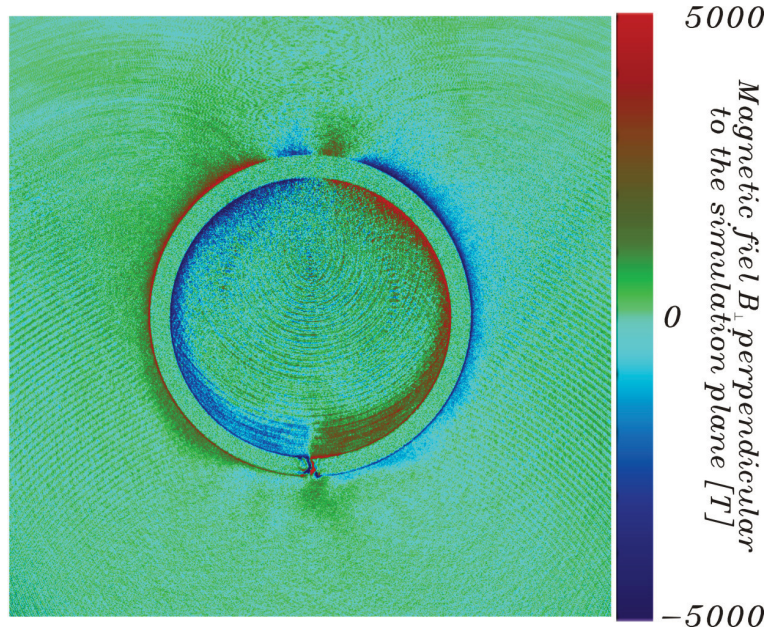
Figure 5.28: The magnetic field perpendicular to the image plane is shown. Two electron beams propagate close to the cylinder surface generating two opposite magnetic fields that coalesce during a magnetic reconnection event. The magnetic field energy is converted to particle motion leading to localized heating of the plasma. The laser irradiates the cylinder from the bottom.

The magnetic field perpendicular to the simulation plane is shown in figure 5.28. The laser irradiates the cylinder from the bottom. At this time step (610 fs) the opposite magnetic field is already connected. A strong decrease in the magnetic field strength in the contact area is measured. From 8000 T the field drops in the middle of the reconnection zone to virtually zero. The heating of the surface can be estimated from the magnetic field energy density $E_B = B^2/2\mu_0 = 2.5 \times 10^7$ J/cm^3 . If this energy

is dumped in the solid electron density of the aluminium one would get electrons with an energy of 2.5×10^7 J/cm^3 /($6\times^{22}$cm^{-3} $\times 1.6 \times 10^{-19}$J/eV Z) $= 2.6/Z$ keV/electron with Z the ionization state of the plasma.

This rough estimate is very close to the electron plasma temperature determined from the velocity of the jet experimentally observed with the optical probe in section 5.11.3.

Following the simulation at later times one sees that after the collision of the two contrary streaming electron beams some of the electrons will cross the cylinder wall. The experimental used cylinder has a wall 50 μm in thickness. Aluminium with this thickness is enough to stop completely a 50 keV electron and to slow down an electron with initial 100 keV to 20 keV.

A closer investigation of this localized heating is beyond the scope of this thesis. The creation of a solid density plasma in keV regime even of small dimension is of huge interest in the context of isochoric heating experiments. The laser community has reported the observation of magnetic reconnection events where the reconnection time reported was in the ns time scale [92, 93]. If the magnetic reconnection scenario is true, this thesis reports of a forced magnetic reconnection event on a hundred fs time scale involving some several tens of MGauss magnetic fields.

5.12   Temporal and spatial field evolution

This section concentrates on studying the temporal and spatial field extension and evolution developed after the irradiation of a mm size object by a ps high intensity laser pulse. The aim is to understand the transient nature of the micro-lens. From the time dependence of the focusing effect it was concluded that the lens is effective for around 15 ps. To confirm this conclusion the experiment shown in the previous section employing proton imaging was repeated. With this method just discrete time steps of the interaction can be measured. In order to overcome this limitation a new setup for making continuous time resolved measurements has been proposed and experimentally demonstrated during this work. The next section will present the continuous time resolved proton imaging setup first on a very simple target, a wire irradiated by a ps long high intensity laser pulse. Afterwards the method will be applied to the laser triggered micro-lens.

5.12.1   Continuous time resolved proton imaging setup

The experiment was conducted at Target Area West at the RAL Laboratory, employing the Vulcan laser operating in the Chirped Pulse Amplification mode (CPA). The two arms CPA1 and CPA2 of the VULCAN laser were compressed to 1.2 ps. The CPA1 pulse (irradiance I=8×10^{18} W/cm^2) was used to accelerate a high-current, diverging beam of up to 12 MeV protons from a 25 μm thick Au foil target. The CPA2 pulse (also $I = 8 \times 10^{18}$ W/cm^2) was focused onto the interaction target. The proton beam from the gold foil was directed through the interaction region created by CPA2 and detected with a stack of Radio Chromic Films positioned from 2 to 5 cm distance from the proton source. The RCF stack was used to measure the intensity modulations in the profile of the proton probe beam due to the field in the interaction region. It also provided a coarse energy resolution due to the energy deposition properties of the protons. It was shielded with an 11 μm Al foil allowing protons with energies above 1.1 MeV to be recorded.

The experimental setup is shown in figure 5.29. First the usual proton imaging setup was used to probe the interaction between CPA2 and a 100 μm thick aluminium wire. The wire is placed 3 mm away from the proton source. The distance between RCF stack and proton source is set to 22 mm giving a magnification factor of $\simeq$7.3. Using this setup the results published by [76] can be easily reproduced. Typical results
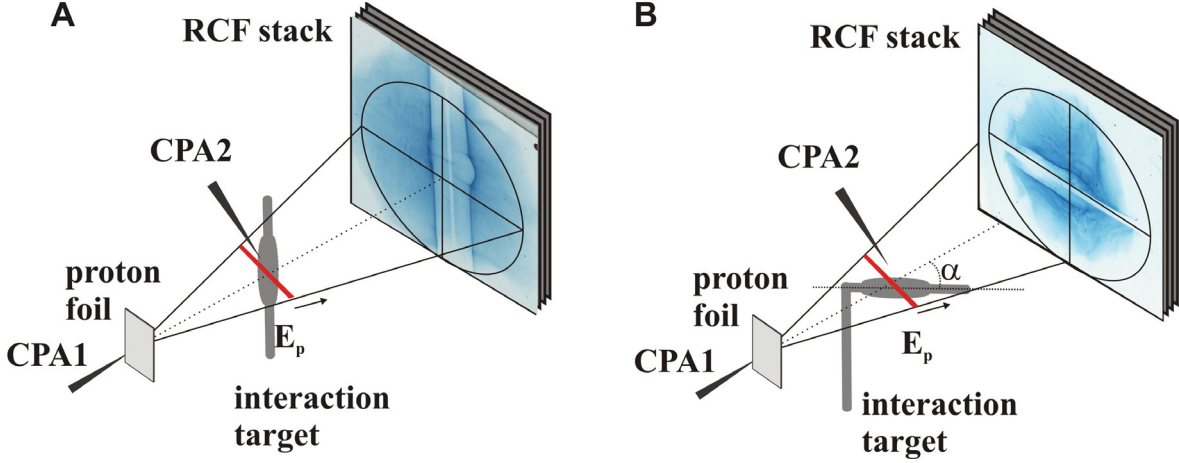
Figure 5.29: Experimental setup. A) The usual proton imaging setup, the whole interaction plane is perpendicular to the beam propagation direction and the region is probed by one proton energy at the time. B) The interaction plane is angled compared to beam propagation region so one proton energy will probe different interaction times according to the energy time of flight to the interaction region.

are shown in figure 5.30a. While the 6.5 MeV protons pass the wire before the main interaction pulse has arrived, the 5.5, 4.5 and 3.1 MeV protons pass at different stages of the interaction. One measures an increasing deflection peaking around 15 ps after the start of a measurable deflection. A time step later (36 ps) the deflection pattern changes dramatically, the previous smooth deflection perpendicular to the wire exchanges for a filamentary structure. Because of the fixed energies detected by the RCF stack intermediate time steps can be gained just if the optical timing between CPA1 and CPA2 is changed. This method is time consuming and subjected to shot to shot variations.

To eliminate this variation a novel proton probing geometry is proposed as shown in figure 5.29 B. Compared to the previous setup the interaction target is placed in an other plane. The wire is set in the plane of proton beam propagation, and angled to the source detector line. The RCF stack is used in the same configuration as above having the same energy detection capability. Now the protons of one energy will have not the same time of flight to the interaction target as above, they will probe the interaction target at different times. The most distant part of the wire compared to the proton source will be probed at latest times, the nearest at earliest interaction time. CPA2 is

still focused at 3 mm from the proton source, the wire being rotated compared to this point. In figure 5.30 B and C the RCF layers corresponding to energies of 5.5 MeV and 3.1 MeV are shown. While part of the 5.5 MeV proton beam arrives at the wire before the field has developed, the 3.1 MeV proton beam probes the deflecting field on the entire wire. The probing time corresponding to each position on the wire is given below the raw film intensity data. By combining the data of both layers a time history of 150 ps was reconstructed. The deflection peaks around $15 - 20$ ps. After 20 ps a filamentary structure grows to reach maximal extension at 50-60 ps. Later on after 120 ps also the field associated to this structure drops below detection threshold.
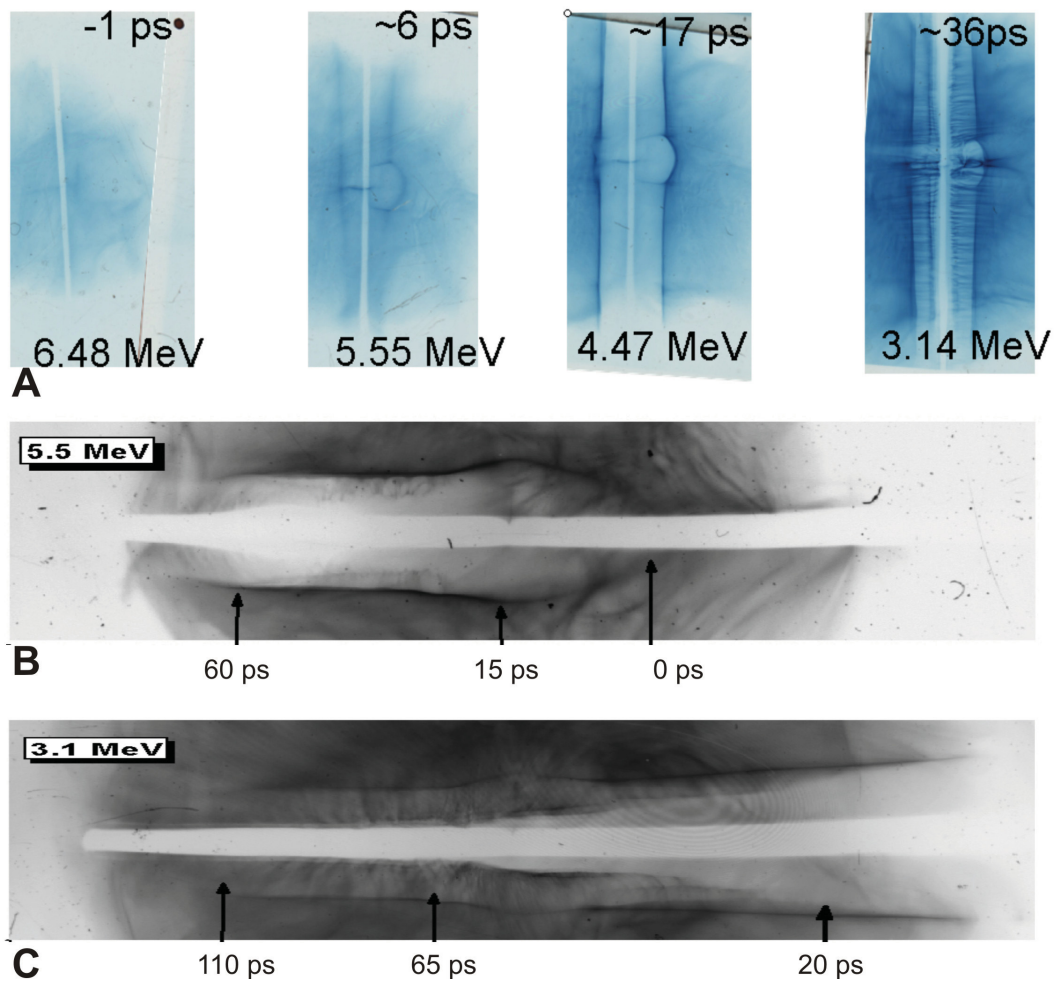
Figure 5.30: Proton probing the laser matter interaction on wire in standard A and continuous time resolved configuration B and C.

5.12.2   Proton Imaging Applied to the Laser-Cylinder Interaction
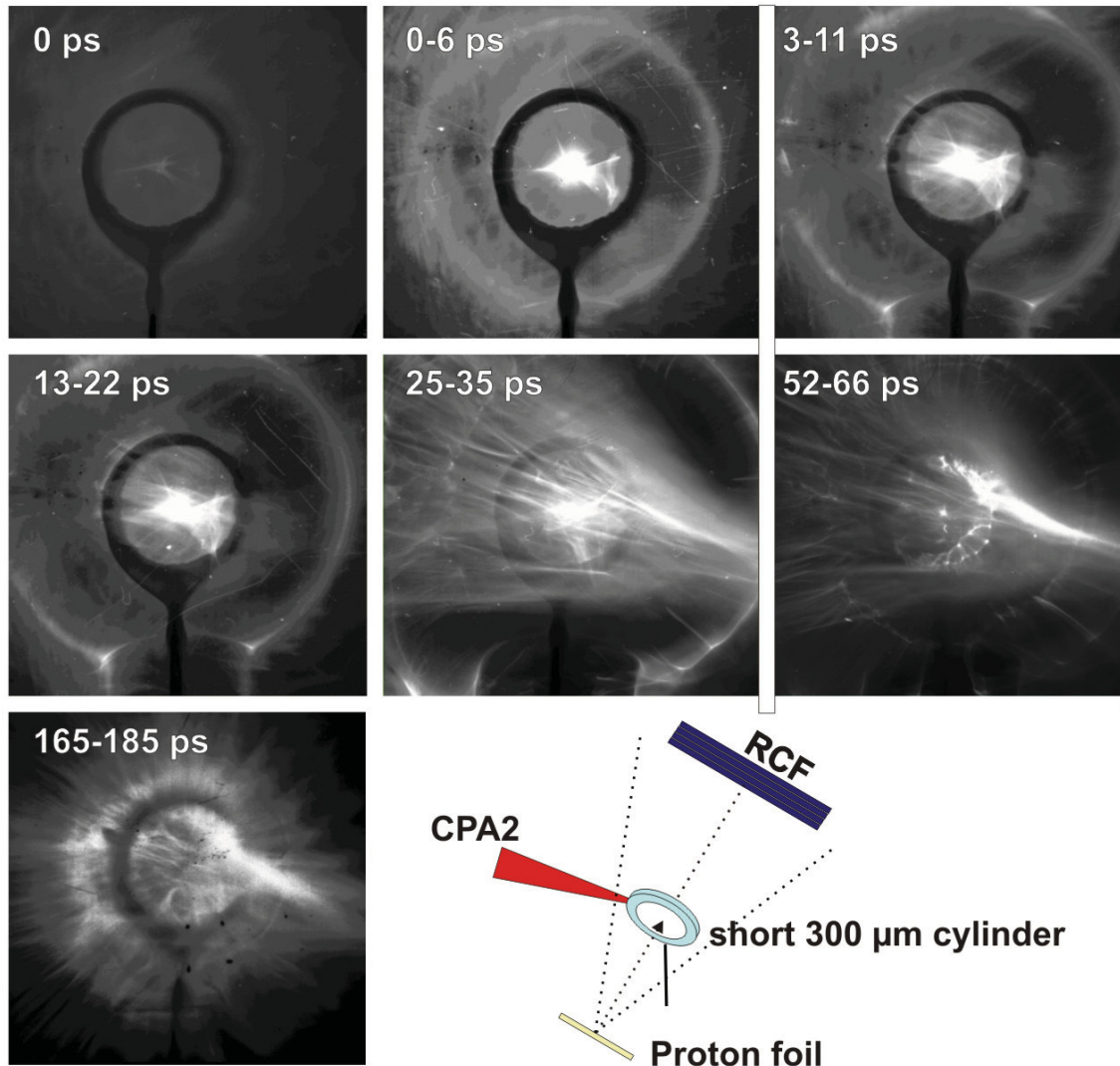
Figure 5.31: Face on proton probing of the field evolution in and outside a 300 μm short cylinder. Proton probe transit times input-exit of the cylinder are given.

Proton imaging and the continuous time resolved proton imaging are applied now to a cylinder. For the proton imaging setup a very short cylinder is used with a length of 300 μm that is probed face on. The experimental result is shown in figure 5.31. The times shown in the figure are transit times from the input to the exit of the cylinder.

The images have been contrast enhanced to see clearly how the deflection pattern evolved. The fields built up on a timescale of 20 ps resulting in a strong focusing effect inside the cylinder and strong defocusing outside the cylinder. After 25 ps the field outside the cylinder begins to collapse resulting in a radial filamentary structure. The collapse is complete after 50 ps, when also strong filamentation inside the cylinder is observed. At very late time 150 ps all regular structure is replaced by radial filaments.

The continuous time resolved proton imaging technique can be applied just to the exterior of the cylinder. The field evolution inside and outside the very short cylinder seems to be qualitatively similar although shifted in time. Hence qualitative information can be gained by studying the exterior fields.
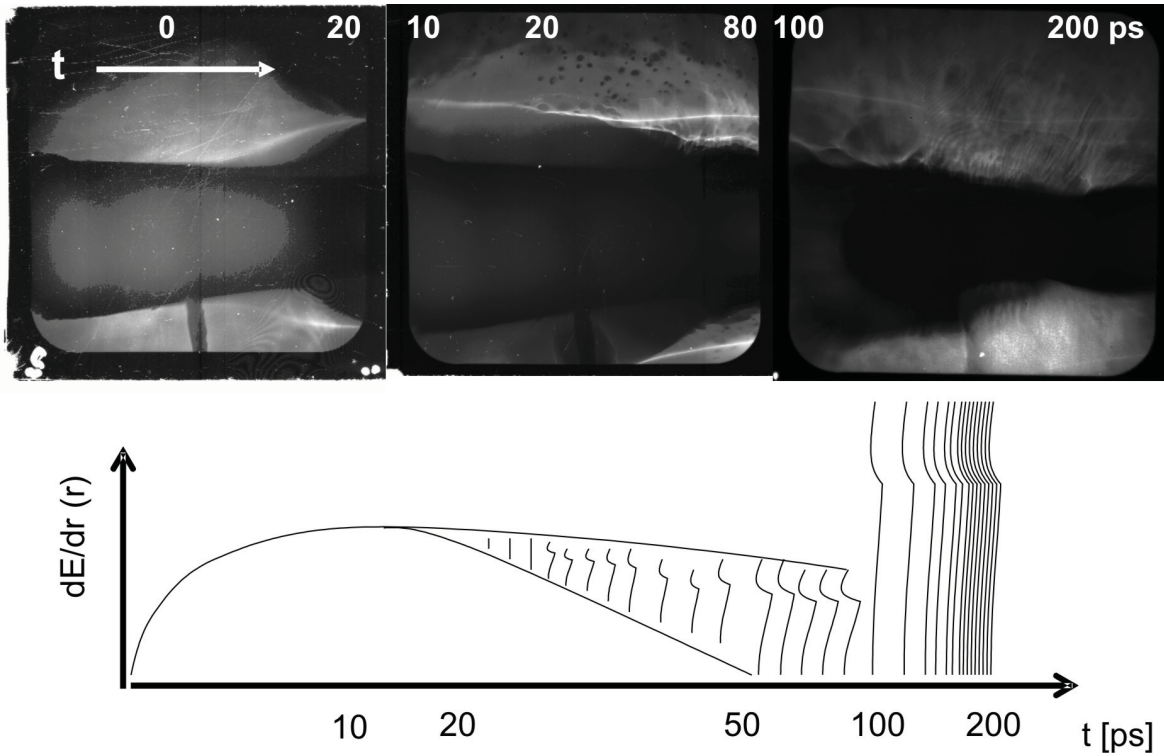
Figure 5.32: Time evolution of the fields developing from the wall of a laser irradiated cylinder probed in the continuous time resolved proton imaging configuration. The time evolution of strong gradients in the fields is sketched at bottom. Both fields rise and decay can be clearly followed.

Figure 5.32 shows the spaial and temporal field evolution on the exterior of the cylinder. The results of the face on proton probing using a short cylinder are confirmed

by the continuous time resolved measurement. The proton beam deflection reaches the peak around 20 ps to break up radially inwards later on in a double layered structure. The same structure can be seen also in face on measurements.
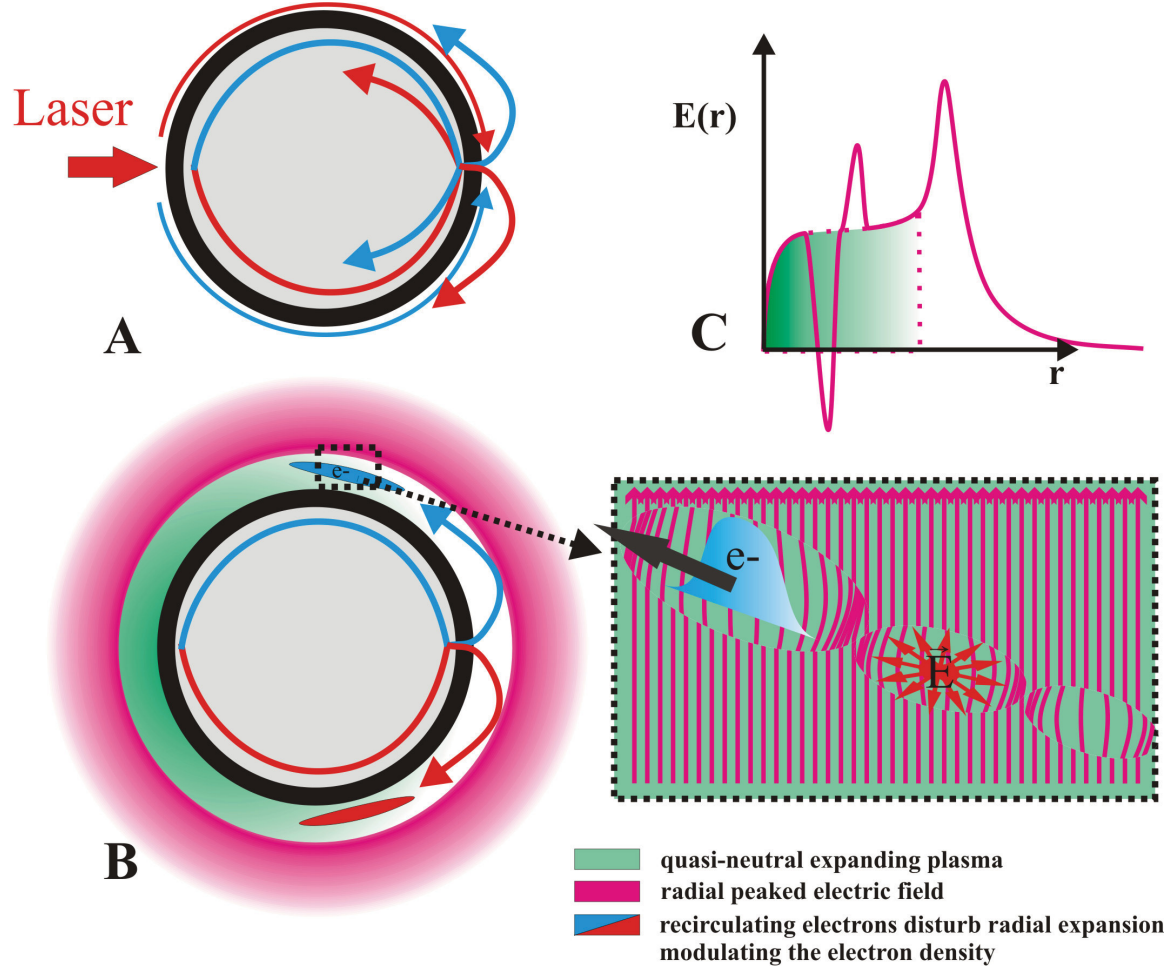
Figure 5.33: A) Path of the hot electrons in and outside the cylinder. B) Electrons circulating around the cylinder pass through a plasma expanding from the wall generating a wake like structure. C) The initial uniform electric field sustained by the quasi-neutral part of the expansion is modulated after the hot electron passage.

To understand the formation of such breakup of the electric field structure the simulation presented in section 5.11.4 was analyzed at laser times. The different paths of the electrons inside and outside the cylinder can be followed and are shown in figure 5.33 A. Electrons originating inside the cylinder pass the cylinder wall and flow back towards the laser irradiation point outside the cylinder. The back circulating

hot electron jet propagates now in an expanding plasma streaming from the wall. The quasi-neutral part of this expansion is disturbed locally by the negative charge excess of the electron beam. The disturbance is measurable if the density of the hot electrons is comparable with the density of the expanding plasma (5.33 B). As a result a wake structure with circular like electron density depressions can be observed in the simulation shown in figure 5.34. The modulated electron density results in electric field structure superimposed to the fields in the expanding plasma from the wall. The electric field due to the electron density modulation points radially from the center of the density depression. A radial line plot of the resulting electric field is shown in
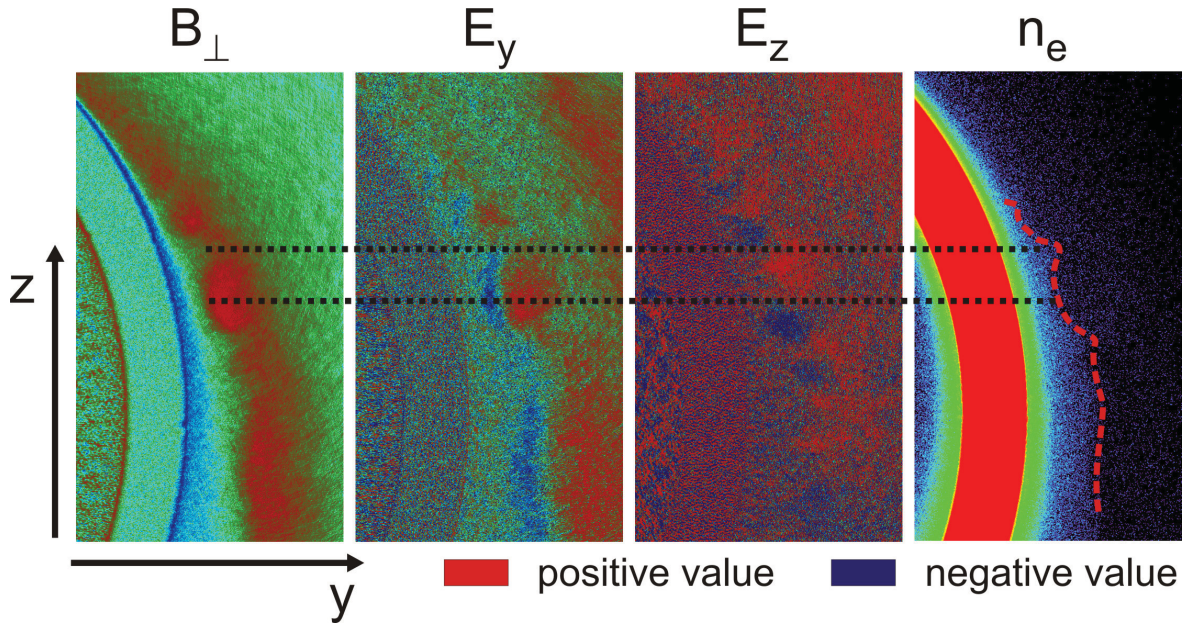
Figure 5.34: When an electron beam traverses a quasi-neutral plasma a wake like disturbance of the electron density is created. The electric fields associated to the density modulation are also shown. An isoline of the electron density is drawn for clarity.

figure 5.33 C. To interpret the effect of this field structure on the probe proton beam ray tracing simulations have been done. The scaled down 2D PSC simulation slice was repeated for a length of 50 μ in a similar way as for the simulations shown in section 5.5. The intensity modulation of the probe proton beam is calculated for two time steps of the PIC simulation. In figure 5.35 at a time (of the PIC simulation) of 884 fs the ray traced simulated radial deflection of protons breaks up in a double layered

structure similar to the measured one. Two type of structures can be distinguished
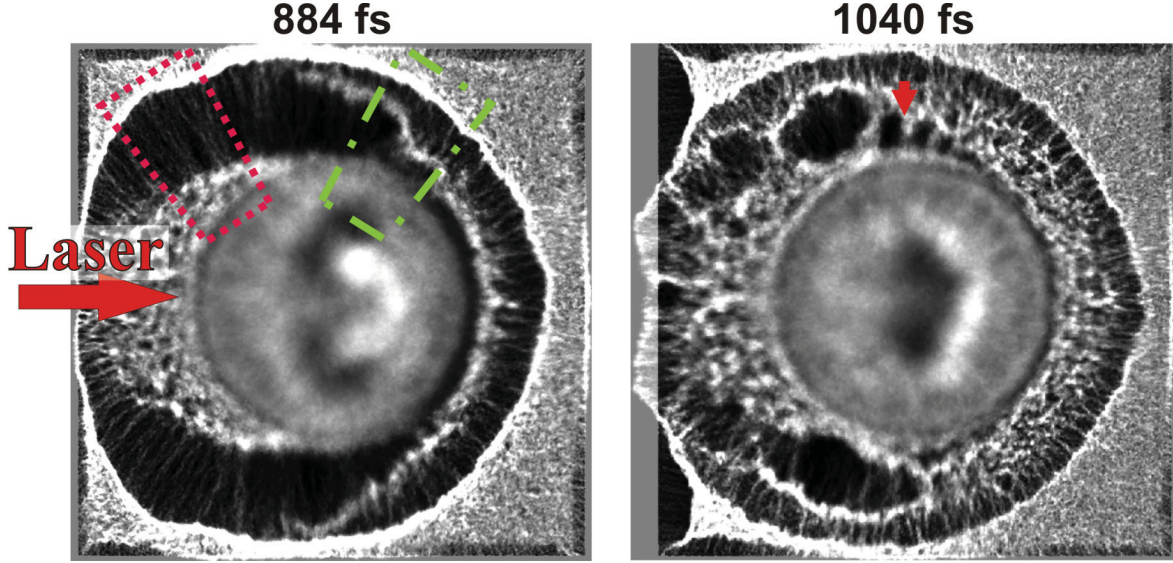
Figure 5.35: The double layer structure observed in the experiment can be reproduced by a ray tracing simulation using the electric field structure calculated by the PSC code. A lighter color stand for a compression of the proton probe, a darker color for a dilution.

in the proton deflection by the exterior of the cylinder. In the area highlighted by a magenta box in figure 5.35 just an annular ring can be observed. This annular structure is created by the deflection of the protons due to the radial pointing field created in the plasma expanding from the wall. Almost no substructure is simulated as the electric field is smooth. In the area highlighted by a green box in figure 5.35 a second annular concentration of the probe protons is simulated. In this part of simulation the expanding plasma from the wall is disturbed by the hot electrons jet. The wake structure of the electric field is more pronounced at a PIC simulation time of 1040 fs. The Bubble like structures are clearly visible. At the same time the inner annular structure moves closer to the cylinder wall.

The experimental measured field evolution after 20 ps is qualitative similar to the one observed in the down-scaled PIC simulation. The PIC simulation timescale of the onset of the electric field break-up of 1 ps becomes similar to the experimental time if scaled up by the geometric down size factor (experimental/simulation cylinder size = 14).

After the inner part of the structure has reached the cylinder surface a new deflection structure emerges. Radial filaments appear that can be see in figure 5.32 after 100 ps and are shown magnified for clarity in figure 5.36.
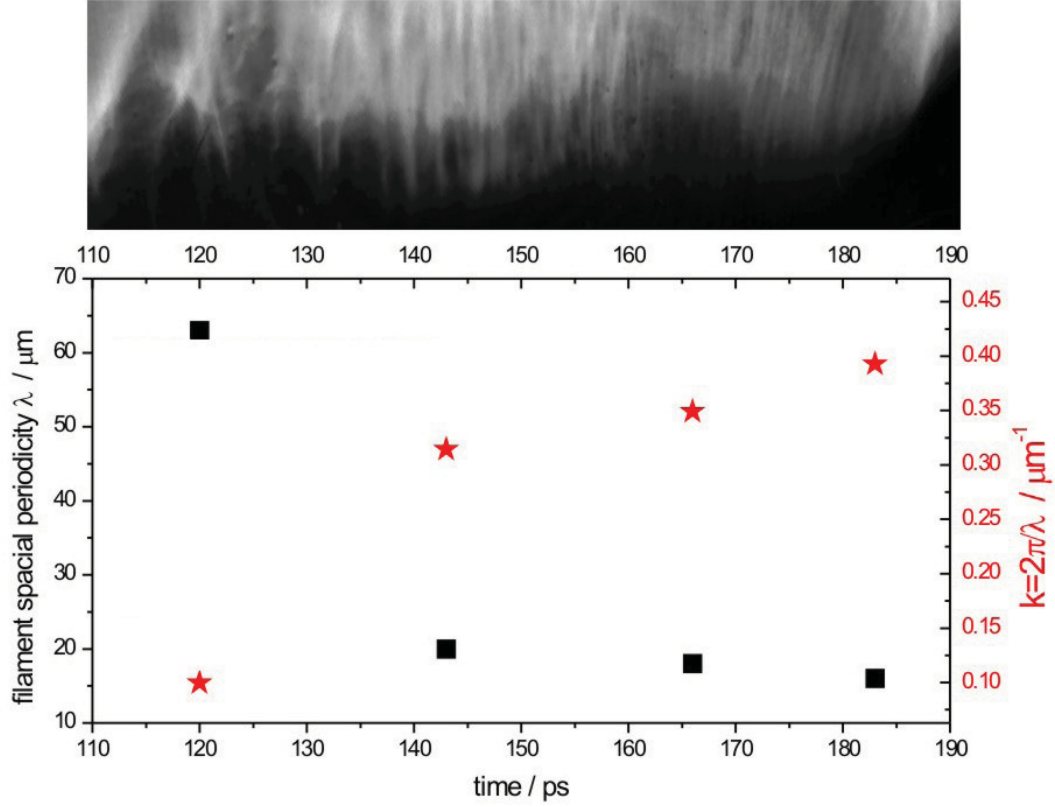
Figure 5.36: Top. The filaments shown in figure 5.32 late time between 110 ps and 190 ps are magnified. Bottom. The time evolution of the filaments periodicity (black squares) and corresponding wave number (red stars) are given. The filaments seen to correspond to the onset and growth of the electro-thermal instability as predicted by Haines.

By analyzing the PIC simulation one learns that a late physical situation could be described as follows. Outside the cylinder the initially hot electrons create a low density population. While expanding and cooling down a part of these electrons will return towards the surface and at the same time a high density cold plasma consisting of the bulk solid material will begin to expand away from the surface. In this context

the electro thermal instability as predicted by Haines in PRL **47,** 917 (1981) will grow: *representing a large heat flow in a plasma as a flow of hot relatively collisionless electrons balanced by an opposing current of cold collisional electrons*. The growth rate α and the wavelength λ of this instability are shown to be $\alpha = 2.8 \times 10^{-8} \cdot n_0 \cdot Z/(A \cdot T_e^{3/2})$ and $\lambda = 2.41 \times 10^{10} \cdot T_e^2 A^{1/2}/n_0/Z$ where A is the atomic number, Z the charge state, n_0 the cold plasma density and T_e the cold electron temperature. Assuming a highly ionized bulk aluminium plasma with $A = 27$ and $Z = 10$ and measuring a build up time of the filaments in the order of 2×10^{-11}s and periodicity of $\simeq 15$ μm one can solve the two upper showed equations for n_0 and T_e yielding $n_0 \simeq 8 \times 10^{23}/\text{cm}^{-3}$ and $T_e \simeq 2.5$ keV the initial conditions of the cold plasma. The calculated numbers are consistent with the plasma parameters of an expanding solid aluminium target.

5.13 Simulation by Collaborators

5.13.1 Simulation of Plasma Expansion with CALDER

1D Particle-in-Cell simulations of field generation at the micro-lens' wall and 3D test-particle simulations of proton propagation through the micro-lens were also performed by Emmanuel d'Hummieres with the PIC Code CALDER [94] giving also an explanation for the divergence reduction and spectral selection capability of the laser triggered micro-lens shown in section 5.2 and 5.10. The simulations use the actual scale of the cylinder used in the experiment and the measured proton beam parameters. In these simulations, he reproduced the plasma flow from a 700 μm diameter cylinder and propagates protons through the space and time dependent resulting fields. As in the experiment, the protons are produced 4 mm in front of the cylinder and they propagate through the cylinder 3 mm in length. The cylinder, which has a thickness of 50 μm, is irradiated by a laser pulse at an intensity 3×10^{18} W/cm^2, and with a pulse duration of 350 fs. The initial electron temperature considered in the PIC simulation is estimated from the pulse's ponderomotive potential, the initial electron density is estimated by considering that a known fraction (i.e. 40 %, inferred from experimental data) of the laser energy is converted into hot electrons. So the hot electron density is $n_e \simeq 6 \times 10^{-5} n_c$, where n_c is the critical density at $\lambda_{Laser} = 1$ μm. It is assumed that when the plasma expansion starts, the field obtained in the PIC simulation is the same for the whole cylinder length.

The plasma begins to expand towards the cylinder axis, driven by a hot electron sheath that extends over a Debye length ahead of the plasma. The radially symmetric ambipolar electrostatic field associated with the plasma front is responsible for the variable focusing of the protons propagating along the cylinder's axis. The proton beam passing through the cylinder is energy chirped due to time-of-flight dispersion, with higher energy protons crossing the cylinder at earlier times. Protons passing through the micro-lens before it is triggered (as in figure 5.3 A for the 9 MeV layer), do not experience any fields and are therefore not deflected. Protons which are crossing the cylinder and are close to its end when it is triggered and therefore experience the fields for only a short time will be almost collimated (as in figure 5.3 A for the 7.5 MeV layer). Lower energy protons will experience a larger cumulated field along their propagation through the cylinder. They are therefore focused at a short distance from the exit plane of the micro-lens and diverge strongly after the focus. This results in

a diluted beam on the RCF stack positioned a few cm away and in the strong dip observed in the spectrum of figure 5.37 right below 6 MeV. Finally, protons having very low energies pass through the micro-lens after the fields have vanished and do not experience any deflection.
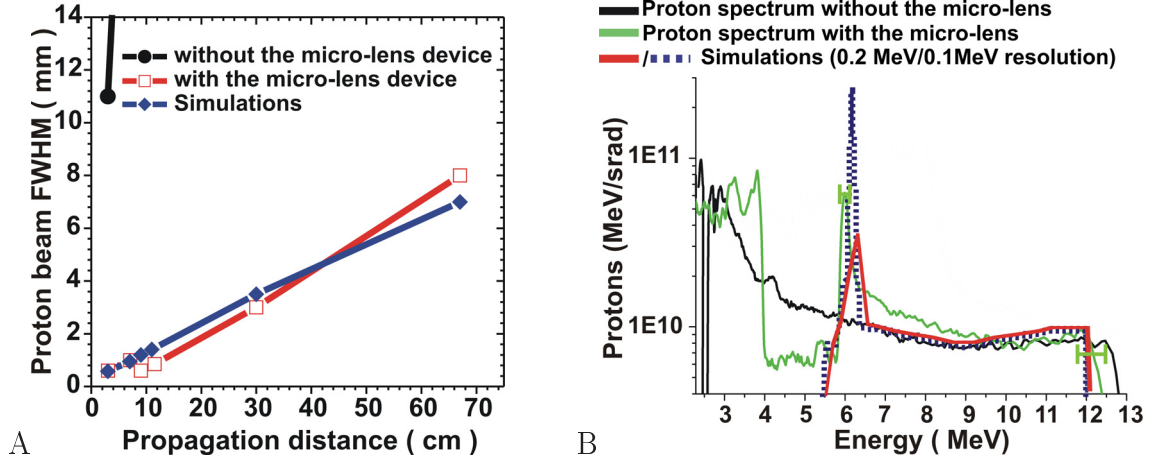
Figure 5.37: A. shows the evolution of the FWHM of the proton beam, for protons with an energy of 7.5 MeV that enter the micro-lens -61 ps relative to the peak of the CPA2 laser pulse versus the propagation distance from the proton source (their transit time through the cylinder is 79 ps). The black circles correspond to the case without micro-lens (free-space divergence), the blue diamonds to the PIC simulation, and the red squares to the experimental results using the micro-lens. The RCFs shown in figure 5.3 correspond to one of the data points in the figure 5.37. B. Proton spectra measured in the experiments using a magnetic spectrometer without micro-lens (black line) and with the micro-lens (green line), and proton spectrum simulated with a PIC simulation code (red line and dotted line) performed using actual proton beam parameters (i.e. the spectrum without micro-lens) and magnetic spectrometer parameters (i.e. distance from the source and slit characteristics). In both cases, the micro-lens is triggered 83 ps after the 6.25 MeV protons have entered the cylinder (their transit time through the cylinder is 86 ps). The distance between the micro-lens and the proton source is 4 mm. The synthetic spectrum was obtained by tracing 5000 protons for each energy considered through the fields predicted by the PIC simulations.

5.13.2 Simulation of Plasma Expansion with VLPL

After the experimental demonstration of the micro-lens Alexander Pukhov gave a first explanation of the laser triggered micro-lens operation. He assumed that the laser pulse produces a population of hot electrons which penetrates through the metal and spread very fast over the inner surface of the cylinder. They exit into vacuum and generate a space charge in the surface vicinity. The electric field of this space charge is large enough to ionize the material and to create a plasma. As a result at an initial time one has a cylindrical plasma layer with a high electron temperature T_e and a low ion temperature $T_i = 0$. The plasma begins to expand toward the cylinder axis due to the TNSA (target normal sheath acceleration) mechanism. The resulting electrostatic fields have a focusing effect on protons. He conducted 3D PIC simulations of the process with the code VLPL [95]. He took a hollow cylinder with a the diameter of 8 μm and assumed that a short laser pulse heated the electrons to $T_e \simeq 500$ keV while the ions remained cold initially. The cylinder is let to freely expand and the field distribution after the simulation time of 150 fs is presented in figure 5.38. One observes the region of focusing electric field in the center of the cylinder (red colored) and the region of defocusing electric field at the outer cylinder surface (blue colored). This model simulation shows that a focusing field can be produced if a cylinder is heated.
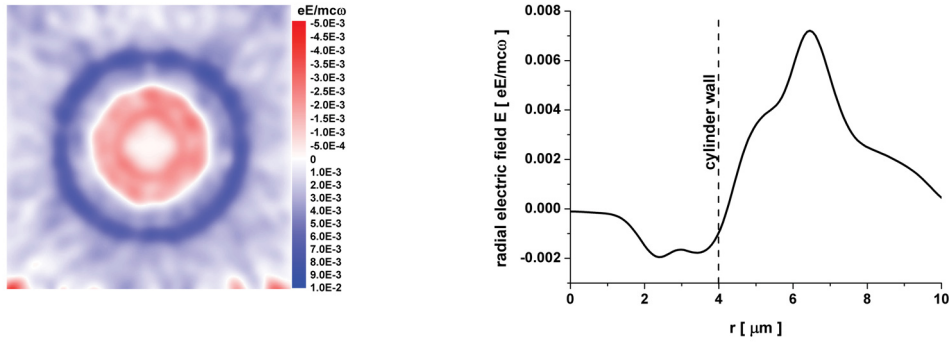

Figure 5.38: Radial electrical field computed with a 3D PIC simulation of the plasma expansion from a cylinder (initial condition $T_e \simeq 500$ keV at cylinder wall). A cross-section through the cylinder is shown. The collimating radial electric field is red coloured. b) radial lineout of electric field. Dashed line shows the position of the cylinder wall.

Later on in [89] this first explanation is further developed by a similarity theory. It is shown that the plasma streaming toward the cylinder axis maintains a focusing electrostatic field due to the positive radial pressure gradient. The cylinder works as a thick lens, whose parameters are obtained from a similarity theory for a freely expanding plasma in cylindrical geometry. Because the lens parameters are energy dependent, the lens focuses a selected energy range of ions and works as a monochromator. Although very elegant the result of this theory concerning the predicted energy to be focused by the lens cannot be directly compared with the experimental data, since some of the quantities defined are not independent. The focusing is caused by the quasi-neutral part of the expanding plasma, the lens parameters depend on the geometrical properties and on the hot electron temperature T_e only, and not on the initial electron density. This result is a key issue predicting that the lens operation can be tuned by changing the intensity of the laser triggering the plasma expansion. This prediction was demonstrated experimentally in section 5.8. A second very intuitive result is that the relative energy width $\delta\mathcal{E}/\mathcal{E}$ of the beam collimated by the lens is narrower for cylinders with $L \ll D$ where L is the length and D the cylinder diameter. A problem of this very short(more ringlike) cylinders is that a direct laser irradiation would destroy the symmetry of the expansion. As observed in the simulations the plasma expanding directly at the rear side of the irradiation point is hotter than the plasma expanding from the remaining wall. The heating of the wall of such rings could be done just indirectly as proposed in the outlook of this work.

5.14 Scaling the lens operation towards higher proton energies

The hadron cancer therapy has gained a lot of interest in the last years. Several therapy centers have been opened for patients or are in construction and commissioning just in Germany at this time. Basically hadron cancer irradiation therapy is attractive due to the special energy deposition curve of the ions in matter. The ions deposit most of their energy at the end of the passage in matter in contrast with electrons and X-rays where the deposition curve drops monotonically. Localized treatment with low collateral damage of healthy tissue is possible even at positions operatively not accessible with very high treatment success rates. Irradiation of different tumor depths in a patient body is done by moderating the energy of a monochromatic beam. The proton beam is brought to the patient by a system of magnetic lenses called a gantry, a device of big dimensions (several m).

Laser acceleration of protons is a fast developing field, in future the replacement of the conventional proton sources with laser sources is discussed [14]. The laser triggered micro-lens could deliver a contribution as beam relaying and focusing and energy selection device for laser accelerated ion sources. The maximum energies used in proton cancer therapy are given by the maximum penetration depth in a human body to be around 240 MeV. A scaling of the operation of the laser triggered micro-lens toward focusing of 240 MeV is given now.

As determined before the fields responsible for the lens effect are created by the wall plasma expansion in vacuum. The field strength of the electric field build up in the initial Debye sheath at the plasma vacuum interface is a function of the electron temperature and scales like:

$$E_{max} = \frac{k_B T_e}{e \lambda_D}$$

where λ_D is the Debye length. At the same time the deflection strength of protons by the lens is proportional to the electric field. From today lens capabilities of focusing a 6 MeV beam 3 cm away from the cylinder with an irradiation intensity of 3×10^{18} W/cm^2 and using the scaling of the imploding plasma electron temperature shown in figure 5.39 calculated with the PSC the lens effect on a 240 MeV beam can be scaled. An irradiation intensity of 1×10^{21} W/cm^2 which would lead to a plasma wall expansion with an electron temperature of $\simeq 380$ keV would be necessary to effectively focus this
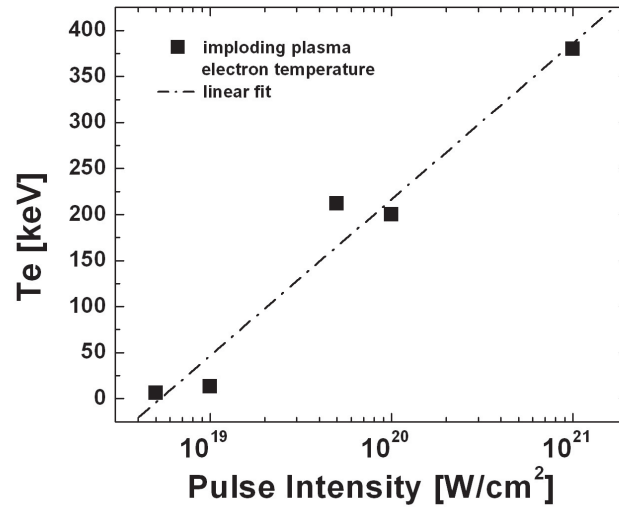
Figure 5.39: Scaling of the imploding plasma electron temperature with the intensity of the laser pulse. The maximum electric field strength is directly proportional to the electron temperature.

high energy protons. The irradiation with today laser capability of longer cylinders would be favorable as the deflection strength is proportional to the square of the transit time in the fields. With a 6 mm long cylinder the focusing of 240 MeV protons could be feasible while the laser aided acceleration of protons to such high energies is still to be demonstrated.

Chapter 6

Summary and Outlook

This work demonstrates experimentally that focusing and energy selection of a MeV poly-energetic diverging laser accelerated proton beam is possible by a laser irradiated hollow cylinder. Electric fields lasting several tens of ps and having strengths of GV/m have been measured and have been determined as generating a positive lens effect on MeV protons transiting axially the cylinder. Experimentally the field existence and a strong localized plasma heating at a point opposite to the laser wall interaction is found to be connected with a transport mechanism close to the cylinder wall by means of proton and optical probing. The lens focal length scales with the laser pulse intensity. Employing a novel proposed proton imaging setup continuous time resolved measurements of the field evolution outside the cylinder were performed. The field evolution can be followed continuously for 150 ps. 20 ps after the interaction of the laser pulse with the cylinder the free plasma expansion from the wall is disturbed resulting in the collapse of radial smooth field structure. In a second stage after 100 ps the electro thermal instability was determined to be responsible for late time plasma filamentation.

2D PIC simulations done with the PSC code for the interpretation of the experimental gathered data show that indeed a radial electric field develops inside a hollow one side laser irradiated cylinder. A hot electron population created at the interaction point mainly by $j \times B$ heating is energetic enough to traverse the cylinder wall. Part of these hot electrons will redistribute inside the cylinder. The simulations show that the hot electron transport is confined to proximity of the surface in a fountain like motion. During the circulation of the hot electrons these ionize the cylinder surface and generate a secondary plasma that expands in vacuum sustaining radial electric fields.

These fields act as a collecting lens on positive charged ions. At the side opposite to the interaction point and inside the cylinder conditions are fulfilled for a magnetic reconnection event leading to strong localized heating. Here the hot electron motion along the surface is redirected toward the cylinder wall and these electrons will be stopped while traversing the wall depositing a substantial amount of energy in the wall. Even after the whole cylinder surface has been ionized the motion of the hot electrons will continue. These electrons will propagate now in the freely expanding plasma from the wall disturbing this expansion. A wake like electric field structure is generated that superimposes to the field of the expanding plasma. This field disturbance grows in time leading to the breakup of the radial smooth electric field. This physical mechanism has been identified to cause the initial collapse of the lens field later than 20 ps after irradiation of the cylinder.

With the help of the PIC simulations the lens operation was scaled for a laser pulse intensity of 1×10^{21} W/cm^2 to focus efficiently 240 MeV protons, an energy required for the cancer therapy of deep seated tumours.

As an outlook further investigations of the laser driven micro-lens by using the newly installed 100 TW laser at the Institute for Laser and Plasma Physics is proposed. The laser is a short pulse (25 fs) 10 Hz Ti:Sa system delivering 2.5 J energy on target. In combination with a 15 mJ synchronized beam optical probing studies of the hot electron redistribution via Faraday rotation for magnetic field detection could be conducted with unprecedented time resolution. Also integrated targets for ion beam production and focusing at a high repetition rate can be imagined.

For increasing the micro-lens capability in terms of the collimation and the selection of a narrower energy bandwidth the irradiation of very short cylinders is desired. If the cylinder wall is directly irradiated by a laser pulse a strong Debye sheet field will be produced at the rear side of the irradiation point. This asymmetry can be neglected for long cylinders (length $\gg$ focal spot size of the laser) but becomes critical for very short cylinders. Part of the electrons creating this field will be electrostatically trapped close to the wall and will redistribute around the cylinder as shown in chapter 5. To increase the symmetry of the plasma expansion inside the cylinder an indirect heating of the cylinder is proposed. A model simulation was run with an modified geometry. A T-shaped structure was added. The T is connected to the cylinder wall and is irradiated by the laser pulse. It should act as an energetic filter for the electrons. Just the electrons having the appropriate energy to move close to the wall should be able

to propagate to the cylinder. Indeed both the electron density and the absolute value of the electric field shown in figure 6.1 show a very symmetric structure, in contrast to the case of direct laser irradiation of the wall. An other method that could result in the same effect to be tested is the irradiation of the stalk holding the cylinder.
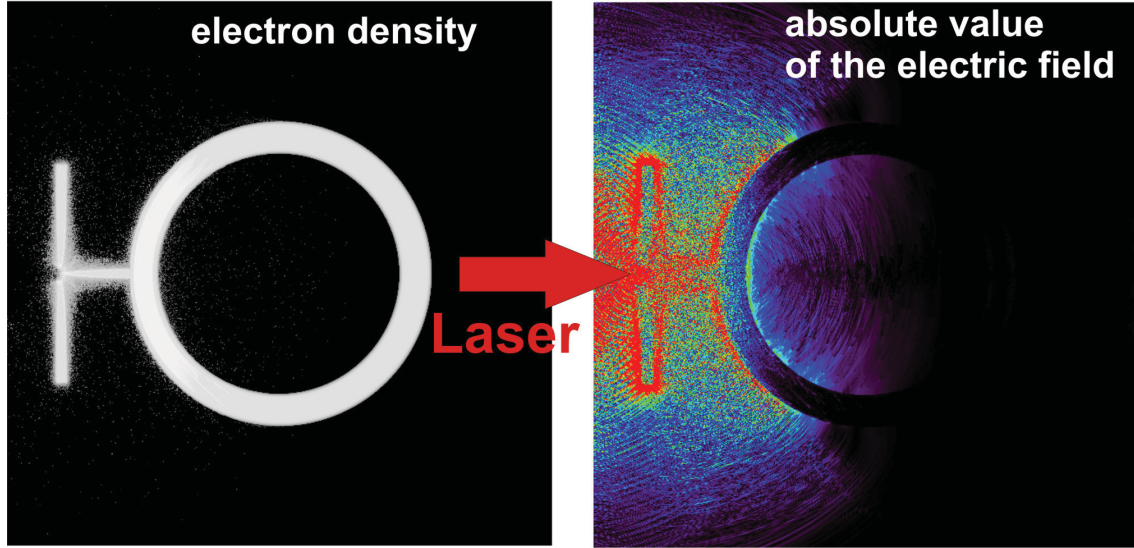
Figure 6.1: By an indirect heating of the cylinder wall a more symmetrical plasma expansion is expected. Both the electron density and the absolute value of the electric field shown are more symmetric compared to the direct irradiation case shown in chapter 5.

Summarizing in a nutshell: This work has studied the time and spatial field evolution from a laser-irradiated hollow cylinder finding very good agreement between experimental and computational data. The laser driven micro-lens can be used as a focusing and energy selection device for MeV proton beams. This work is of relevance to the development of applications of the laser-accelerated protons.

Articles and Patents

During this thesis the author has been involved in several studies that led to refereed publications. The experiments were investigating different modalities of enhancing laser accelerated proton sources in anticipation of different applications. The articles directly reporting about the laser triggered micro-lens are marked with an *.

Cerchez, M., Jung, R., Osterholz, J., Toncian, T., Willi, O., Mulser, P. and Ruhl, H., *Absorption of ultra-short laser pulses in strongly over-dense targets*, submitted to **Phys. Rev. Lett.**

Nickles, P.V., Schnürer, M., Sokollik, T., Ter-Avetisyan, S.,Sandner, W., Amin, M., Toncian, T., Willi, O., Andreev, A., *Ultrafast laser driven proton sources and dynamical proton imaging*, submitted to **JOSAB**

Romagnani, L., Borghesi, M., Cecchetti, C. A., Kar, S., Antici, P., Audebert, P., Bandhoupadjay, S., Ceccherini, F., Cowan, T. , Fuchs, J., Galimberti, M., Gizzi, L. A., Grismayer, T., Heathcote, R., Jung, R., Liseykina, T. V., Macchi, A., Mora, P., Neely, D., Notley, M., Osterholtz, J., Pipahl, C. A., Pretzler, G., Schiavi, A., Schurtz, G., Toncian T., Wilson, P. A. and Willi, O., *Proton Probing Measurement of Electric and Magnetic Fields Generated by ns and ps Laser-Matter Interactions*, in print in **Laser and Particle Beams** (2008)

Sokollik, T. , Schnürer, M., Ter-Avetisyan,S., Nickles, P.V., Risse, E., Kalashnikov, M., Sandner, W., Priebe, G., Amin, M., Toncian, T., Willi, O., and Andreev, A.A. *Transient electric fields in laser plasmas observed by proton streak deflectometry*, **Appl. Phys. Lett. 92**, 091503 (2008)

Borghesi, M., Cecchetti, C. A., Romagnani, L., Antici, P., Audebert, P., Fuchs, J., d'Humieres, E., Brambrink, E., Toncian, T., Pipahl, A., Willi, O., and Lefevbre,

E. *Laser-accelerated protons: Perspectives for control/optimization of beam properties.* **International Journal of Modern Physics B 21**, 3-4 (Feb. 2007), 590–599.

Fuchs, J., Cecchetti, C. A., Borghesi, M., Grismayer, T., d'Humieres, E., Antici, P., Atzeni, S., Mora, P., Pipahl, A., Romagnani, L., Schiavi, A., Sentoku, Y., Toncian, T., Audebert, P., and Willi, O. *Laser-foil acceleration of high-energy protons in small-scale plasma gradients.* **Physical Review Letters 99**, 1 (July 2007), 015002.

Antici, P., Fuchs, J., d'Humieres, E., Lefebvre, E., Borghesi, M., Brambrink, E., Cecchetti, C. A., Gaillard, S., Romagnani, L., Sentoku, Y., Toncian, T., Willi, O., Audebert, P., and Pepin, H. *Energetic protons generated by ultrahigh contrast laser pulses interacting with ultrathin targets.* **Physics of Plasmas 14**, 3 (Mar. 2007), 030701.

∗Willi, O., Toncian, T., Borghesi, M., Fuchs, J., d'Humieres, E., Antici, P., Audebert, P., Brambrink, E., Cecchetti, C., Pipahl, A., and Romagnani, L. *Laser triggered micro-lens for focusing and energy selection of mev protons.* **Laser and Particle Beams 25**, 1 (Mar. 2007), 71–77.

∗Borghesi, M., Kar, S., Romagnani, L., Toncian, T., Antici, P., Audebert, P., Brambrink, E., Ceccherini, F., Cecchetti, C. A., Fuchs, J., Galimberti, M., Gizzi, L. A., Grismayer, T., Lyseikina, T., Jung, R., Macchi, A., Mora, P., Osterholtz, J., Schiavi, A., and Willi, O. *Impulsive electric fields driven by high-intensity laser matter interactions.* **Laser and Particle Beams 25**, 1 (Mar. 2007), 161–167.

Fuchs, J., Antici, P., d'Humieres, E., Lefebvre, E., Borghesi, M., Brambrink, E., Cecchetti, C., Toncian, T., Pepin, H., and Audebert, P. *Ion acceleration using high-contrast ultra-intense lasers.* **Journal de Physique IV 133** (June 2006), 1151–1153.

∗Toncian, T., Borghesi, M., Fuchs, J., d'Humieres, E., Antici, P., Audebert, P., Brambrink, E., Cecchetti, C. A., Pipahl, A., Romagnani, L., and Willi, O. *Ultrafast laser-driven microlens to focus and energy-select mega-electron volt protons.* **Science 312**, 5772 (Apr. 2006), 410–413.

Fuchs, J., Antici, P., D'Humieres, E., Lefebvre, E., Borghesi, M., Brambrink, E., Cecchetti, C. A., Kaluza, M., Malka, V., Manclossi, M., Meyroneinc, S., Mora, P., Schreiber, J., Toncian, T., Pepin, H., and Audebert, R. *Laser-driven proton scaling laws and new paths towards energy increase.* **Nature Physics 2**, 1 (Jan. 2006), 48–54.

Romagnani, L., Fuchs, J., Borghesi, M., Antici, P., Audebert, P., Ceccherini, F., Cowan, T., Grismayer, T., Kar, S., Macchi, A., Mora, P., Pretzler, G., Schiavi, A., Toncian, T., and Willi, O. *Dynamics of electric fields driving the laser acceleration of multi-mev protons.* **Physical Review Letters 95**, 19 (Nov. 2005), 195001.

Borghesi, M., Audebert, P., Bulanov, S. V., Cowan, T., Fuchs, J., Gauthier, J. C., MacKinnon, A. J., Patel, P. K., Pretzler, G., Romagnani, L., Schiavi, A., Toncian, T., and Willi, O. *High-intensity laser-plasma interaction studies employing laser-driven proton probes.* **Laser and Particle Beams 23**, 3 (Sept. 2005), 291–295.

Willi, O., Toncian, T., Borghesi, M. and Fuchs, J., *Deutsche Patentanmeldung 10 2005 012 059.8 PILZ* (**2005**); also filed in the EU, US and Japan.

Bibliography

[1] PERRY, M. D., AND MOUROU, G. Terawatt to petawatt subpicosecond lasers. **Science 264**, 5161 (May 1994), 917–924.

[2] CLARK, E. L., KRUSHELNICK, K., DAVIES, J. R., ZEPF, M., TATARAKIS, M., BEG, F. N., MACHACEK, A., NORREYS, P. A., SANTALA, M. I. K., WATTS, I., AND DANGOR, A. E. Measurements of energetic proton transport through magnetized plasma from intense laser interactions with solids. **Physical Review Letters 84**, 4 (Jan. 2000), 670–673.

[3] SNAVELY, R. A., KEY, M. H., HATCHETT, S. P., COWAN, T. E., ROTH, M., PHILLIPS, T. W., STOYER, M. A., HENRY, E. A., SANGSTER, T. C., SINGH, M. S., WILKS, S. C., MACKINNON, A., OFFENBERGER, A., PENNINGTON, D. M., YASUIKE, K., LANGDON, A. B., LASINSKI, B. F., JOHNSON, J., PERRY, M. D., AND CAMPBELL, E. M. Intense high-energy proton beams from petawatt-laser irradiation of solids. **Physical Review Letters 85**, 14 (Oct. 2000), 2945–2948.

[4] MAKSIMCHUK, A., GU, S., FLIPPO, K., UMSTADTER, D., AND BYCHENKOV, V. Y. Forward ion acceleration in thin films driven by a high-intensity laser. **Physical Review Letters 84**, 18 (May 2000), 4108–4111.

[5] MALKA, V., FAURE, J., GLINEC, Y., AND LIFSCHITZ, A. F. Laser-plasma accelerators: a new tool for science and for society. **Plasma Physics and Controlled Fusion 47** (Dec. 2005), B481–B490.

[6] TABAK, M., HAMMER, J., GLINSKI, M. E., KRUER, W. L., WILKS, S. C., WOODWORTH, J., CAMPBELL, E. M., PERRY, M. D., AND MASON, R. J. Ignition and high gain with ultrapowerful lasers. **Physics of Plasmas 1**, 5 (1994), 1626.

117

[7] ROUSSE, A., PHUOC, K. T., SHAH, R., PUKHOV, A., LEFEBVRE, E., MALKA, V., KISELEV, S., BURGY, F., ROUSSEAU, J. P., UMSTADTER, D., AND HULIN, D. Production of a kev x-ray beam from synchrotron radiation in relativistic laser-plasma interaction. **Physical Review Letters 93**, 13 (Sept. 2004), 135005.

[8] LEDINGHAM, K. W. D., MCKENNA, P., AND SINGHAL, R. P. Applications for nuclear phenomena generated by ultra-intense lasers. **Science 300**, 5622 (May 2003), 1107–1111.

[9] REMINGTON, B. A., ARNETT, D., DRAKE, R. P., AND TAKABE, H. Experimental astrophysics - modeling astrophysical phenomena in the laboratory with intense lasers. **Science 284**, 5419 (May 1999), 1488–1493.

[10] BORGHESI, M., MACKINNON, A. J., CAMPBELL, D. H., HICKS, D. G., KAR, S., PATEL, P. K., PRICE, D., ROMAGNANI, L., SCHIAVI, A., AND WILLI, O. Multi-mev proton source investigations in ultraintense laser-foil interactions. **Physical Review Letters 92**, 5 (Feb. 2004), 055003.

[11] COWAN, T. E., FUCHS, J., RUHL, H., KEMP, A., AUDEBERT, P., ROTH, M., STEPHENS, R., BARTON, I., BLAZEVIC, A., BRAMBRINK, E., COBBLE, J., FERNANDEZ, J., GAUTHIER, J. C., GEISSEL, M., HEGELICH, M., KAAE, J., KARSCH, S., LE SAGE, G. P., LETZRING, S., MANCLOSSI, M., MEYRONEINC, S., NEWKIRK, A., PEPIN, H., AND RENARD-LEGALLOUDEC, N. Ultralow emittance, multi-mev proton beams from a laser virtual-cathode plasma accelerator. **Physical Review Letters 92**, 20 (May 2004), 204801.

[12] PATEL, P. K., MACKINNON, A. J., KEY, M. H., COWAN, T. E., FOORD, M. E., ALLEN, M., PRICE, D. F., RUHL, H., SPRINGER, P. T., AND STEPHENS, R. Isochoric heating of solid-density matter with an ultrafast proton beam. **Physical Review Letters 91**, 12 (Sept. 2003), 125004.

[13] BORGHESI, M., CAMPBELL, D. H., SCHIAVI, A., HAINES, M. G., WILLI, O., MACKINNON, A. J., PATEL, P., GIZZI, L. A., GALIMBERTI, M., CLARKE, R. J., PEGORARO, F., RUHL, H., AND BULANOV, S. Electric field detection in laser-plasma interaction experiments via the proton imaging technique. **Physics of Plasmas 9**, 5 (May 2002), 2214–2220.

[14] BULANOV, S. V., ESIRKEPOV, T. Z., KHOROSHKOV, V. S., KUNETSOV, A. V., AND PEGORARO, F. Oncological hadrontherapy with laser ion accelerators. **Physics Letters A 299**, 2-3 (July 2002), 240–247.

[15] SPENCER, I., LEDINGHAM, K. W. D., SINGHAL, R. P., McCANNY, T., McKENNA, P., CLARK, E. L., KRUSHELNICK, K., ZEPF, M., BEG, F. N., TATARAKIS, M., DANGOR, A. E., NORREYS, P. A., CLARKE, R. J., ALLOTT, R. M., AND ROSS, I. N. Laser generation of proton beams for the production of short-lived positron emitting radioisotopes. **Nuclear Instruments & Methods In Physics Research Section B-Beam Interactions With Materials and Atoms 183**, 3-4 (Oct. 2001), 449–458.

[16] ROTH, M., COWAN, T. E., KEY, M. H., HATCHETT, S. P., BROWN, C., FOUNTAIN, W., JOHNSON, J., PENNINGTON, D. M., SNAVELY, R. A., WILKS, S. C., YASUIKE, K., RUHL, H., PEGORARO, F., BULANOV, S. V., CAMPBELL, E. M., PERRY, M. D., AND POWELL, H. Fast ignition by intense laser-accelerated proton beams. **Physical Review Letters 86**, 3 (Jan. 2001), 436–439.

[17] SZILAGYI, M. Electron and ion optics. Plenum Press, 1988.

[18] LUO, W., FOURKAL, E., LI, J. S., AND MA, C. M. Particle selection and beam collimation system for laser-accelerated proton beam therapy. **Medical Physics 32**, 3 (Mar. 2005), 794–806.

[19] HEGELICH, B. M., ALBRIGHT, B. J., COBBLE, J., FLIPPO, K., LETZRING, S., PAFFETT, M., RUHL, H., SCHREIBER, J., SCHULZE, R. K., AND FERNANDEZ, J. C. Laser acceleration of quasi-monoenergetic mev ion beams. **Nature 439**, 7075 (Jan. 2006), 441–444.

[20] SCHWOERER, H., PFOTENHAUER, S., JACKEL, O., AMTHOR, K. U., LIESFELD, B., ZIEGLER, W., SAUERBREY, R., LEDINGHAM, K. W. D., AND ESIRKEPOV, T. Laser-plasma acceleration of quasi-monoenergetic protons from microstructured targets. **Nature 439**, 7075 (Jan. 2006), 445–448.

[21] BULANOV, S. V. New epoch in the charged particle acceleration by relativistically intense laser radiation. **Plasma Physics and Controlled Fusion 48**, 12B (2006), B29–B37.

[22] DUNNE, M. A high-power laser fusion facility for europe. **Nat Phys 2**, 1 (Jan. 2006), 2–5.

[23] GERSTNER, E. Laser physics: Extreme light. **Nature 446**, 7131 (Mar. 2007), 16–18.

[24] PROTOPAPAS, M., KEITEL, C. H., AND KNIGHT, P. L. Atomic physics with super-high intensity lasers. **Reports on Progress in Physics 60**, 4 (1997), 389–486.

[25] AMMONOSOV, M. V., DELONE, N. B., AND KRAINOV, V. P. Tunnel ionization of complex atoms and atomic ions in a varying electromagnetic-field. **Zhurnal Eksperimentalnoi I Teoreticheskoi Fiziki 91**, 6 (Dec. 1986), 2008–2013.

[26] LOTZ, W. Electron-impact ionization cross-sections and ionization rate coefficients for atoms and ions. **Astrophysical Journal S 14** (1967), 207–&.

[27] BELL, K. L., GILBODY, H. B., HUGHES, J. G., KINGSTON, A. E., AND SMITH, F. J. Recommended data on the electron-impact ionization of light-atoms and ions. **Journal of Physical and Chemical Reference Data 12**, 4 (1983), 891–916.

[28] PRETZLER, G. Generating high-energy particle and photons with femtosecond laser, 2001.

[29] QUESNEL, B., MORA, P., ADAM, J. C., GUERIN, S., HERON, A., AND LAVAL, G. Electron parametric instabilities of ultraintense short laser pulses propagating in plasmas. **Physical Review Letters 78**, 11 (Mar. 1997), 2132–2135.

[30] TAJIMA, T., AND DAWSON, J. M. Laser electron accelerator. **Phys. Rev. Lett. 43**, 4 (Jul 1979), 267–270.

[31] LEEMANS, W. P., NAGLER, B., GONSALVES, A. J., TOTH, C., NAKAMURA, K., GEDDES, C. G. R., ESAREY, E., SCHROEDER, C. B., AND HOOKER, S. M. Gev electron beams from a centimetre-scale accelerator. **Nature Physics 2**, 10 (Oct. 2006), 696–699.

[32] PUKHOV, A., AND MEYER-TER VEHN, J. Laser wake field acceleration: the highly non-linear broken-wave regime. **Applied Physics B-Lasers and Optics 74**, 4-5 (Apr. 2002), 355–361.

[33] FAURE, J., GLINEC, Y., PUKHOV, A., KISELEV, S., GORDIENKO, S., LEFEB-VRE, E., ROUSSEAU, J. P., BURGY, F., AND MALKA, V. A laser-plasma accelerator producing monoenergetic electron beams. **Nature 431**, 7008 (Sept. 2004), 541–544.

[34] FAURE, J., RECHATIN, C., NORLIN, A., LIFSCHITZ, A., GLINEC, Y., AND MALKA, V. Controlled injection and acceleration of electrons in plasma wakefields by colliding laser pulses. **Nature 444**, 7120 (Dec. 2006), 737–739.

[35] HIDDING, B., AMTHOR, K. U., LIESFELD, B., SCHWOERER, H., KARSCH, S., GEISSLER, M., VEISZ, L., SCHMID, K., GALLACHER, J. G., JAMISON, S. P., JAROSZYNSKI, D., PRETZLER, G., AND SAUERBREY, R. Generation of quasimonoenergetic electron bunches with 80-fs laser pulses. **Physical Review Letters 96**, 10 (Mar. 2006), 105004.

[36] ELIEZER, S. The Interaction of High-Power Lasers with Plasmas. Institute of Physics, 2002.

[37] FREIDBERG, J. P., MITCHELL, R. W., MORSE, R. L., AND RUDSINSKI, L. I. Resonant absorption of laser light by plasma targets. **Phys. Rev. Lett. 28**, 13 (Mar 1972), 795–799.

[38] BEG, F. N., BELL, A. R., DANGOR, A. E., DANSON, C. N., FEWS, A. P., GLINSKY, M. E., HAMMEL, B. A., LEE, P., NORREYS, P. A., AND TATARAKIS, M. A study of picosecond laser–solid interactions up to 10[sup 19] w cm[sup - 2]. **Physics of Plasmas 4**, 2 (1997), 447–457.

[39] BRUNEL, F. Not-so-resonant, resonant absorption. **Phys. Rev. Lett. 59**, 1 (Jul 1987), 52–55.

[40] WILKS, S. C., KRUER, W. L., TABAK, M., AND LANGDON, A. B. Absorption of ultra-intense laser pulses. **Phys. Rev. Lett. 69**, 9 (Aug 1992), 1383–1386.

[41] SENTOKU, Y., COWAN, T. E., KEMP, A., AND RUHL, H. High energy proton acceleration in interaction of short laser pulse with dense plasma target. **Physics of Plasmas 10**, 5 (2003), 2009–2015.

[42] GITOMER, S. J., JONES, R. D., BEGAY, F., EHLER, A. W., KEPHART, J. F., AND KRISTAL, R. Fast ions and hot-electrons in the laser-plasma interaction. **Physics of Fluids 29**, 8 (Aug. 1986), 2679–2688.

[43] KEY, M. H., CABLE, M. D., COWAN, T. E., ESTABROOK, K. G., HAMMEL, B. A., HATCHET, S. P., HENRY, E. A., HINKEL, D. E., KILKENNY, J. D., KOCH, J. A., KRUER, W. L., LANGDON, A. B., LASINSKI, B. F., LEE, R. W., MACGOWAN, B. J., MACKINNON, A. J., MOODY, J. D., MORAN, M. J., OFFENBERGER, A. A., PENNINGTON, D. M., PERRY, M. D., PHILLIPS, T. J., SANGSTER, T. C., SINGH, M. S., STOYER, M. A., TABAK, M., TIETBOHL, G. L., TSUKAMOTO, M., WHARTON, K., AND WILKS, S. C. Hot electron production and heating by hot electrons in fast ignitor research. **Physics of Plasmas 5**, 5 (1998), 1966.

[44] HATCHETT, S. P., BROWN, C. G., COWAN, T. E., HENRY, E. A., JOHNSON, J. S., KEY, M. H., KOCH, J. A., LANGDON, A. B., LASINSKI, B. F., LEE, R. W., MACKINNON, A. J., PENNINGTON, D. M., PERRY, M. D., PHILLIPS, T. W., ROTH, M., SANGSTER, T. C., SINGH, M. S., SNAVELY, R. A., STOYER, M. A., WILKS, S. C., AND YASUIKE, K. Electron, photon, and ion beams from the relativistic interaction of petawatt laser pulses with solid targets. **Physics of Plasmas 7**, 5 (May 2000), 2076–2082.

[45] MCKENNA, P., LEDINGHAM, K. W. D., YANG, J. M., ROBSON, L., MC-CANNY, T., SHIMIZU, S., CLARKE, R. J., NEELY, D., SPOHR, K., CHAPMAN, R., SINGHAL, R. P., KRUSHELNICK, K., WEI, M. S., AND NORREYS, P. A. Characterization of proton and heavier ion acceleration in ultrahigh-intensity laser interactions with heated target foils. **Physical Review E 70**, 3 (Sept. 2004), 036405.

[46] ZEPF, M., CLARK, E. L., KRUSHELNICK, K., BEG, F. N., ESCODA, C., DANGOR, A. E., SANTALA, M. I. K., TATARAKIS, M., WATTS, I. F., NORREYS, P. A., CLARKE, R. J., DAVIES, J. R., SINCLAIR, M. A., EDWARDS, R. D., GOLDSACK, T. J., SPENCER, I., AND LEDINGHAM, K. W. D. Fast particle generation and energy transport in laser-solid interactions. **Physics of Plasmas 8**, 5 (May 2001), 2323–2330.

122

[47] ALLEN, M., SENTOKU, Y., AUDEBERT, P., BLAZEVIC, A., COWAN, T., FUCHS, J., GAUTHIER, J. C., GEISSEL, M., HEGELICH, M., KARSCH, S., MORSE, E., PATEL, P. K., AND ROTH, M. Proton spectra from ultraintense laser-plasma interaction with thin foils: Experiments, theory, and simulation. **Physics of Plasmas 10**, 8 (Aug. 2003), 3283–3289.

[48] FRITZLER, S., MALKA, V., GRILLON, G., ROUSSEAU, J. P., BURGY, F., LEFEBVRE, E., D'HUMIERES, E., MCKENNA, P., AND LEDINGHAM, K. W. D. Proton beams generated with high-intensity lasers: Applications to medical isotope production. **Applied Physics Letters 83**, 15 (Oct. 2003), 3039–3041.

[49] FUCHS, J., SENTOKU, Y., KARSCH, S., COBBLE, J., AUDEBERT, P., KEMP, A., NIKROO, A., ANTICI, P., BRAMBRINK, E., BLAZEVIC, A., CAMPBELL, E. M., FERNANDEZ, J. C., GAUTHIER, J. C., GEISSEL, M., HEGELICH, M., PEPIN, H., POPESCU, H., RENARD-LEGALLOUDEC, N., ROTH, M., SCHREIBER, J., STEPHENS, R., AND COWAN, T. E. Comparison of laser ion acceleration from the front and rear surfaces of thin foils. **Physical Review Letters 94**, 4 (Feb. 2005), 045004.

[50] HEGELICH, M., KARSCH, S., PRETZLER, G., HABS, D., WITTE, K., GUENTHER, W., ALLEN, M., BLAZEVIC, A., FUCHS, J., GAUTHIER, J. C., GEISSEL, M., AUDEBERT, P., COWAN, T., AND ROTH, M. Mev ion jets from short-pulse-laser interaction with thin foils. **Physical Review Letters 89**, 8 (Aug. 2002), 085002.

[51] GUREVICH, A. V., PARIISKA.LV, AND PITAEVSK.LP. Self-similar motion of rarefied plasma. **Soviet Physics Jetp-Ussr 22**, 2 (1966), 449–&.

[52] MORA, P. Plasma expansion into a vacuum. **Physical Review Letters 90**, 18 (May 2003), 185002.

[53] MORA, P. Thin-foil expansion into a vacuum. **Physical Review E 72**, 5 (Nov. 2005), 056401.

[54] FUCHS, J., ANTICI, P., D'HUMIERES, E., LEFEBVRE, E., BORGHESI, M., BRAMBRINK, E., CECCHETTI, C. A., KALUZA, M., MALKA, V., MANCLOSSI, M., MEYRONEINC, S., MORA, P., SCHREIBER, J., TONCIAN, T., PEPIN, H.,

AND AUDEBERT, R. Laser-driven proton scaling laws and new paths towards energy increase. **Nature Physics 2**, 1 (Jan. 2006), 48–54.

[55] ROMAGNANI, L., FUCHS, J., BORGHESI, M., ANTICI, P., AUDEBERT, P., CECCHERINI, F., COWAN, T., GRISMAYER, T., KAR, S., MACCHI, A., MORA, P., PRETZLER, G., SCHIAVI, A., TONCIAN, T., AND WILLI, O. Dynamics of electric fields driving the laser acceleration of multi-mev protons. **Physical Review Letters 95**, 19 (Nov. 2005), 195001.

[56] TER-AVETISYAN, S., SCHNURER, M., NICKLES, P. V., KALASHNIKOV, M., RISSE, E., SOKOLLIK, T., SANDNER, W., ANDREEV, A., AND TIKHONCHUK, V. Quasimonoenergetic deuteron bursts produced by ultraintense laser pulses. **Physical Review Letters 96**, 14 (Apr. 2006), 145006.

[57] NAKAMURA, S., IKEGAMI, M., IWASHITA, Y., SHIRAI, T., TONGUI, H., SOUDA, H., DAIDO, H., MORI, M., KADO, M., SAGISAKA, A., OGURA, K., NISHIUCHI, M., ORIMO, S., HAYASHI, Y., YOGO, A., PIROZHKOV, A. S., BULANOV, S. V., ESIRKEPOV, T., NAGASHIMA, A., KIMURA, T., TAJIMA, T., TAKEUCHI, T., FUKUMI, A., LI, Z., AND NODA, A. High-quality laser-produced proton beam realized by the application of a synchronous rf electric field. **Japanese Journal of Applied Physics Part 2-Letters & Express Letters 46**, 29-32 (Aug. 2007), L717–L720.

[58] SCHREIBER, J., KALUZA, M., GRUNER, F., SCHRAMM, U., HEGELICH, B. M., COBBLE, J., GEISSLER, M., BRAMBRINK, E., FUCHS, J., AUDEBERT, P., HABS, D., AND WITTE, K. Source-size measurements and charge distributions of ions accelerated from thin foils irradiated by high-intensity laser pulses. **Applied Physics B-Lasers and Optics 79**, 8 (Dec. 2004), 1041–1045.

[59] ANTICI, P., FUCHS, J., D'HUMIERES, E., LEFEBVRE, E., BORGHESI, M., BRAMBRINK, E., CECCHETTI, C. A., GAILLARD, S., ROMAGNANI, L., SENTOKU, Y., TONCIAN, T., WILLI, O., AUDEBERT, P., AND PEPIN, H. Energetic protons generated by ultrahigh contrast laser pulses interacting with ultrathin targets. **Physics of Plasmas 14**, 3 (Mar. 2007), 030701.

[60] WEIBEL, E. S. **Phys. Rev. Lett. 2** (1959), 83.

[61] Jung, R., Osterholz, J., Lowenbruck, K., Kiselev, S., Pretzler, G., Pukhov, A., Willi, O., Kar, S., Borghesi, M., Nazarov, W., Karsch, S., Clarke, R., and Neely, D. Study of electron-beam propagation through preionized dense foam plasmas. **Physical Review Letters 94**, 19 (May 2005), 195001.

[62] Manclossi, M., Santos, J. J., Batani, D., Faure, J., Debayle, A., Tikhonchuk, V. T., and Malka, V. Study of ultraintense laser-produced fast-electron propagation and filamentation in insulator and metal foil targets by optical emission diagnostics. **Physical Review Letters 96**, 12 (Mar. 2006), 125002.

[63] Stein, J., Fill, E., Habs, D., Pretzler, G., and Witte, K. Hot electron diagnostics using x-rays and cerenkov radiation. **Laser and Particle Beams 22**, 3 (Sept. 2004), 315–321.

[64] Batani, D., Manclossi, M., Santos, J. J., Tikhonchuk, V. T., Faure, J., Guemnie-Tafo, A., and Malka, V. Transport of intense laser-produced electron beams in matter. **Plasma Physics and Controlled Fusion 48**, 12B (Dec. 2006), B211–B220.

[65] Wei, M. S., Beg, F. N., Clark, E. L., Dangor, A. E., Evans, R. G., Gopal, A., Ledingham, K. W. D., McKenna, P., Norreys, P. A., Tatarakis, M., Zepf, M., and Krushelnik, K. Observations of the filamentation of high-intensity laser-produced electron beams. **Phys. Rev. E 70** (2004), 056412.

[66] Ruhl, H. 3d kinetic simulation of super-intense laser-induced anomalous transport. **Plasma Sources Sci. Technol. 11** (2002), A154.

[67] Honda, M. Eigenmodes and growth rates of relativistic current filamentation instability in a collisional plasma. **Phys. Rev. E 69** (2004), 16401.

[68] Fonseca, R. A., Silva, L. O., Tonge, J. W., Mori, W. B., and Dawson, J. M. Three-dimensional weibel instability in astrophysical scenarios. **Physics of Plasmas 10**, 5 (2003), 1979.

[69] PUKHOV, A. Three-dimensional simulations of ion acceleration from a foil irradiated by a short-pulse laser. **Physical Review Letters 86**, 16 (Apr. 2001), 3562–3565.

[70] NAKAMURA, T., KATO, S., NAGATOMO, H., AND MIMA, K. Surface-magnetic-field and fast-electron current-layer formation by ultraintense laser irradiation. **Physical Review Letters 93**, 26 (Dec. 2004), 265002.

[71] SENTOKU, Y., KEMP, A. J., PRESURA, R., BAKEMAN, M. S., AND COWAN, T. E. Isochoric heating in heterogeneous solid targets with ultrashort laser pulses. **Physics of Plasmas 14**, 12 (2007), 122701.

[72] ZIEGLER, J., BIERSACK, J., AND LITTMARK, U. The Stopping and Range of Ions in Solids, vol. 1. Pergamon Press, 1985.

[73] ZIEGLER, J. F., BIERSACK, J. P., AND ZIEGLER, M. D. SRIM - The Stopping and Range of Ions in Matter. srim.org, 2008.

[74] KEMP, A. J., PFUND, R. E. W., AND MEYER-TER VEHN, J. Modeling ultrafast laser-driven ionization dynamics with monte carlo collisional particle-in-cell simulations. **Physics of Plasmas 11**, 12 (Dec. 2004), 5648–5657.

[75] BORGHESI, M., SCHIAVI, A., CAMPBELL, D. H., HAINES, M. G., WILLI, O., MACKINNON, A. J., GIZZI, L. A., GALIMBERTI, M., CLARKE, R. J., AND RUHL, H. Proton imaging: a diagnostic for inertial confinement fusion/fast ignitor studies. **Plasma Physics and Controlled Fusion 43** (Dec. 2001), A267–A276.

[76] BORGHESI, M., SCHIAVI, A., CAMPBELL, D. H., HAINES, M. G., WILLI, O., MACKINNON, A. J., PATEL, P., GALIMBERTI, M., AND GIZZI, L. A. Proton imaging detection of transient electromagnetic fields in lasor-plasma interactions (invited). **Review of Scientific Instruments 74**, 3 (Mar. 2003), 1688–1693.

[77] MCLAUGHLIN, W. L., MILLER, A., FIDAN, S., PEJTERSEN, K., AND PEDERSEN, W. B. Radiochromic plastic films for accurate measurement of radiation absorbed dose and dose distributions. **Radiation Physics and Chemistry 10**, 2 (1977), 119–127.

[78] MCLAUGHLIN, W., YUN-DONG, C., AND SOARES, C. Sensitometry of the response of a new radiochromic film dosimeter to gamma radiation and electron

beams. **Nuclear Instruments and Methods in Physics Research A 302** (1991), 165–176.

[79] HIDDING, B., PRETZLER, G., CLEVER, M., BRANDL, F., ZAMPONI, F., LUBCKE, A., KAMPFER, T., USCHMANN, I., FORSTER, E., SCHRAMM, U., SAUERBREY, R., KROUPP, E., VEISZ, L., SCHMID, K., BENAVIDES, S., AND KARSCH, S. Novel method for characterizing relativistic electron beams in a harsh laser-plasma environment. **Review of Scientific Instruments 78**, 8 (Aug. 2007), 083301.

[80] TANAKA, K. A., YABUUCHI, T., SATO, T., KODAMA, R., KITAGAWA, Y., TAKAHASHI, T., IKEDA, T., HONDA, Y., AND OKUDA, S. Calibration of imaging plate for high energy electron spectrometer. **Review of Scientific Instruments 76**, 1 (Jan. 2005), 013507.

[81] VOGEL, H. Gerthsen Physik. Springer, 1999.

[82] BORGHESI, M., ROMAGNANI, L., SCHIAVI, A., CAMPBELL, D. H., HAINES, M. G., WILLI, O., MACKINNON, A. J., GALIMBERTI, M., GIZZI, L., CLARKE, R. J., AND HAWKES, S. Measurement of highly transient electrical charging following high-intensity laser-solid interaction. **Applied Physics Letters 82**, 10 (Mar. 2003), 1529–1531.

[83] MACKINNON, A. J., PATEL, P. K., TOWN, R. P., EDWARDS, M. J., PHILLIPS, T., LERNER, S. C., PRICE, D. W., HICKS, D., KEY, M. H., HATCHETT, S., WILKS, S. C., BORGHESI, M., ROMAGNANI, L., KAR, S., TONCIAN, T., PRETZLER, G., WILLI, O., KOENIG, M., MARTINOLLI, E., LEPAPE, S., BENUZZI-MOUNAIX, A., AUDEBERT, P., GAUTHIER, J. C., KING, J., SNAVELY, R., FREEMAN, R. R., AND BOEHLLY, T. Proton radiography as an electromagnetic field and density perturbation diagnostic (invited). **Review of Scientific Instruments 75**, 10 (Oct. 2004), 3531–3536.

[84] TONCIAN, T. Quantitative messungen von elektrischen feldern in laser generierten plasmen. Diploma thesis, Heinrich-Heine-Universität Düsseldorf Mathematisch-Naturwissenschaftliche Fakultät, 2004.

[85] SETTLES, G. S. Schlieren and Shadowgraph Techniques. Springer, Berlin, 2001.

[86] Danson, C. N., Brummitt, P. A., Clarke, R. J., Collier, J., Bell, B., Frackiewicz, A. J., Hancock, S., Hawkes, S., Hernandez-Gomez, C., Holligan, P., Hutchionson, M. H. R., Kidd, A., Lester, W. J., Musgrave, I. O., Neely, D., Neville, D. R., Norreys, P. A., Pepler, D. A., Reason, C. J., Shaikh, W., Winstone, T. B., Wyatt, R. W. W., and Wyborn, B. E. Vulcan petawatt - and ultra-high-intensity interaction facility. **Nuclear Fusion 44** (2004), 239.

[87] Danson, C. N., Collier, J., Neely, D., Barazanti, L. J., Damerell, A., Edwards, R., Hutchionson, M. H. R., Key, M. H., Norreys, P. A., Pepler, D. A., Ross, I. N., Taday, P. F., Toner, W. T., Trentelman, M., Walsh, F. N., Winstone, T. B., and Wyatt, R. W. W. Well characterized 10^{19} w cm^2 operation of vulcan - an ultra-high power nd:glass laser. **Journal of Modern Optics 45**, 8 (1998), 1653.

[88] Wilks, S. C. Simulatrions of ultraintense laser-plasma interactions. **Phys. Fluids B 5** (1993), 2603.

[89] Gordienko, S., Baeva, T., and Pukhov, A. Focusing of laser-generated ion beams by a plasma cylinder: Similarity theory and the thick lens formula. **Physics of Plasmas 13**, 6 (2006), 063103.

[90] Huba, J. D. Nrl plasma formulary.

[91] Drake, J. F., Shay, M. A., Thongthai, W., and Swisdak, M. Production of energetic electrons during magnetic reconnection. **Physical Review Letters 94**, 9 (Mar. 2005), 095001.

[92] Li, C. K., Seguin, F. H., Frenje, J. A., Rygg, J. R., Petrasso, R. D., Town, R. P. J., Amendt, P. A., Hatchett, S. P., Landen, O. L., Mackinnon, A. J., Patel, P. K., Smalyuk, V. A., Sangster, T. C., and Knauer, J. P. Measuring e and b fields in laser-produced plasmas with monoenergetic proton radiography. **Physical Review Letters 97**, 13 (Sept. 2006), 135003.

[93] Li, C. K., Seguin, F. H., Frenje, J. A., Rygg, J. R., Petrasso, R. D., Town, R. P. J., Amendt, P. A., Hatchett, S. P., Landen, O. L., Mackinnon, A. J., Patel, P. K., Smalyuk, V. A., Knauer, J. P., Sangster, T. C., and Stoeckl, C. Monoenergetic proton backlighter for measuring e

and b fields and for radiographing implosions and high-energy density plasmas (invited). **Review of Scientific Instruments 77**, 10 (Oct. 2006), 10E725.

[94] LEFEBVRE, E., COCHET, N., FRITZLER, S., MALKA, V., ALEONARD, M. M., CHEMIN, J. F., DARBON, S., DISDIER, L., FAURE, J., FEDOTOFF, A., LANDOAS, O., MALKA, G., MEOT, V., MOREL, P., LE GLOAHEC, M. R., ROUYER, A., RUBBELYNCK, C., TIKHONCHUK, V., WROBEL, R., ANDEBERT, P., AND ROUSSEAUX, C. Electron and photon production from relativistic laser-plasma interactions. **Nuclear Fusion 43**, 7 (July 2003), 629–633.

[95] PUKHOV, A. Three-dimensional electromagnetic relativistic particle-in-cell code vlpl (virtual laser plasma lab). **J. Plasma Physics 61**, 3 (1999), 425.

Danksagung

Abschließend möchte ich mich bei Herrn Professor O. Willi bedanken, der immer ein offenes Ohr hatte und stets bereit war mir mit einem guten Ratschlag weiter zu helfen. Einen besonderen Dank Herrn Professor K.-H. Spatschek, der bereit war das Koreferat dieser Arbeit zu übernehmen.

Mein besonderer Dank gilt all denjenigen, die mit zum Gelingen dieser Arbeit beigetragen haben. Einen besonderen Dank allen Kollegen und Kolleginnen am Institut für Laser und Plasmaphysik der Universität Düsseldorf die mir jahrelang während meiner Dissertation zur Seite standen und mich begleitet haben. Vielen Dank den Mitstreitern vieler und langer Experimentiernächte: Carlo, Ariane, Munib, Timur, Wilson, Pati, Erik, Lorenzo. Vielen Dank dem Marco Borghesi und dem Julien Fuchs für Rat und Tat. Mein besonderer Dank gilt Ralph Jung für die anregenden Diskussionen und dem geteilten Leid.

Dem Herrn Professor H. Ruhl möchte ich für die Bereitstellung des PIC Codes PSC danken. Prof S. Bulanov danke ich für die fruchtbaren Diskussionen in Bezug zur PIC Simulation. Götz danke ich für die Hilfe bei der Einrichtung des Clusters.

Schließlich muss ich Monika meiner geliebten Frau danken, erst durch Sie habe ich noch Kraft gefunden, auch wenn keine mehr da war. Vielen Dank für deine unschätzbare Hilfe und Geduld (besonders während der letzten Tage dieser Schrift)!

Beneath knowing, understanding
Beneath understanding, seeing
Beneath seeing, recognizing
Beneath recognizing, knowing
Keeper of the Way, Vision of Faith, CY 10003 (Andromeda Ascendant Opening Quote Episode 219)